The University Of Sheffield.

Department Of Mechanical Engineering

PhD Mechanical Engineering

Development of a High Pressure Torsion Test for Recreating Deformed Layers in Rail

James **Ayabina**

February 2026

Supervisors: Prof Roger Lewis, Dr Christophe Pinna

Thesis submitted to the Department of Mechanical Engineering, University of Sheffield in partial fulfilment of the requirements for the degree of PhD

SUMMARY

This thesis outlines work carried to develop a method for recreating plastically deformed layers to allow fatigue crack growth testing material with properties and microstructure equivalent to those found in the actual rail. The top layer of the rail experiences high contact pressure (above material yield) and shear from wheel passage. This leads to the creation of a highly deformed layer. Rail damage such as wear and rolling contact fatigue are initiated in this layer.

Design work has been carried out to develop the set-up and testing approach for high pressure torsion (HPT) testing to create a deformed layer representative of that on wheels and rails and for a fatigue crack growth (FCG) test to assess properties of specimens taken from the deformed layer created from the HPT process.

Tests have been completed under different conditions and using varying rail grades, R260, R350HT and R400HT. Consistent deformed layers were created which compare well with those found in field rail in terms of microstructure and hardness.

A new method was established for extracting fatigue crack growth (FCG) specimens from the specimens so that the deformed layer could be tested in a cyclic fatigue test.

A pilot test set-up was iterated through several machines that would allow the very small FCG specimens to be tested. Unfortunately, this could not be run successfully as the string of components within the set-up were not stiff enough and the connections were taking up the load rather than it being transferred to the specimen. A new approach has been defined that will allow larger deformed layer specimens to be created and a different FCG test to be carried out.

NOMENCLATURE

a	Crack length in fatigue crack growth (FCG) specimen (mm)
a_0	Initial crack length (mm)
B	Thickness of FCG specimen (mm)
b	Fatigue strength exponent in strain life relation equation
C	Constant in Paris equation
c	Fatigue ductility exponent in strain life equation
da	Difference in crack length (mm)
dN	Difference in number of cycles
ECAP	Equal channel angular processing
E	Young's modulus (GPa)
F	Geometry function of specimen in stress intensity calculations
FCG	Fatigue Crack Growth
HPT	High Pressure Torsion
K	Stress intensity (MPa√m)
k	Wear coefficient
K_{max}	Maximum stress intensity per cycle (MPa√m)
K_{min}	Minimum stress intensity per cycle (MPa√m)
K_{IC}	Fracture toughness (MPa√m)
ΔK	Difference in stress intensity per cycle (MPa√m)
m	Second constant in Paris equation
N_f	Number of cycles to failure
p_m	Material hardness in Archard equation
p_0	Maximum Hertz pressure (MPa)
P_{max}	Maximum load per Cycle (N)
P_{min}	Minimum load per Cycle (N)
ΔP	Difference between maximum and minimum load in a cycle (N)

R	Ratio of load or stress intensity per cycle
Ry	Cyclic plastic zone (mm)
T	Torque (Nm)
V	Worn volume in Archard equation (mm^3)
W	Specimen dimension in crack direction (mm)
w	Normal load in Archard equation (N)
σ_{ys}	Yield strength (MPa)
σ_f	Fatigue strength coefficient
ε_f	Fatigue ductility
$\Delta\varepsilon$	Difference in strain
ε_{vm}	von Mises strain

CONTENTS

ACKNOWLEDGEMENTS

I would like to thank Virtual Vehicle Research for providing this research opportunity with special mention to Dr Gerald Trummer and Dr Klaus Six. I would also like to thank my supervisors Professor Roger Lewis and Dr Christophe Pinna for their advice and guidance during this research in particular Professor Roger Lewis for the support offered during those extremely difficult periods.

This project was very challenging from start to finish from the manufacturing of the anvils used to the machining of the testing specimens made. It would not have been possible without the expertise of LAW Grinding who were willing to take on the challenge and attempt machining that looked almost impossible. The COVID pandemic made a challenging PhD even more demanding and tricky. As a result, special mention also to goes to Tesoro Monaghan and Sylwester Mikula of the Materials Science and Engineering department at The University of Sheffield for their help and Dr Le Ma for electron microscopy analysis.

I would also like to say thank you to my father Mr K. P. Ayabina for the tremendous support as well as advice offered during the research as well as thank you to my brother and his wife Mr and Mrs T. C. Ayabina for the immeasurable support given during the research. Especial during the trying times where it looked like all hope was lost. Special mention also to my son Rio Damolehi Ayabina for being my number one fan and cheering me on all the way to the finish line. Thank you very much son.

1 INTRODUCTION

1.1 Background to the problem

The key to this work centres around establishing an understanding of the material deformation that occurs at the wheel-rail interface due to the loads the materials experiences and the resulting effect on the fatigue crack propagation behaviour. This has led to the development of a testing apparatus which can be used for testing small compact tension specimens. The conditions at the wheel-rail interface lead to strain levels as high as 6 (Meyer, Nikas and Ahlström, 2018) near the surface of the rail and wheel materials although it could be higher as it is hard to measure. This results in significant changes in the mechanical properties with levels as high as 2500MPa for the UTS and hardness levels as high as 570Hv being achieved (Lee and Polycarpou, 2005). This comes from a starting point of 950MPa and 320Hv hardness in the virgin material in the case of R260 in the unstrained condition (Peixoto and Ferreira, 2013).

The depth of material that undergoes plasticity as a result of the wheel-rail contact has been reported to be around 1mm under very severe conditions (Larijani *et al.*, 2014). This is clearly not enough material for traditional fatigue crack growth test specimens to be manufactured from. The recommended minimum thickness of the specimen according to ASTM E647 is 1.3 mm. As a result, new approaches are needed for assessing the impact of the severe plastic deformation (SPD) process.

New techniques have been emerging to help create a severe plastically deformed layer similar to that at the wheel-rail interface. They include equal channel angular process (ECAP) and the high pressure torsion process (HPT), to mention a few. Both ECAP and HPT are reviewed in detail to establish their potential for use in this work. There is a significant drop in fracture toughness of the material after it undergoes a large amount of strain going from 55MPa√m in the as received material to a little as 4MPa√m depending on the notch orientation for the fracture toughness testing and the amount of strain the material has experienced (Hohenwarter *et al.*, 2011). This has an impact on the testing that can be carried out as well as how the test can be conducted to establish properties as the material could be relatively brittle.

Whilst some work has been done on the role of the microstructure on the damage and wear mechanisms of wheel and rail material; further understanding is needed to fully appreciate the role the microstructure plays especially when anisotropy is considered in relation to fatigue crack growth through the deformed layer (Leitner, Hohenwarter and Pippan, 2019). The data gathered will be used in modelling damage propagation in the deformed layer to try and predict the material behaviour in parallel projects. Modelling techniques already developed include the wedge (Trummer, Marte, Scheriau, *et al.*, 2016) and T-gamma models (Six *et al.*, 2020), to mention a few. Some of the modelling approaches are discussed in brief to show how data from the experimental work feeds into them.

1.2 Aims and objectives

The aim of the project is to develop a technique able to recreate the microstructure of the deformed layer on a railway wheel or rail surface (a result of the repeated cyclic loading in the wheel/rail interface) in preparation for creating small specimens from the layer to carry out fatigue crack growth tests to assess the properties of the deformed layer.

Objectives included:

- Carrying out a thorough literature review and assessment of the wheel/rail interface to help define the test approaches and the target microstructure of the deformed layer and strain levels.
- Developing a test set-up to achieve the chosen method for creating the deformed layer
- Carrying out test on different rail grades
- Analysing the microstructure and properties of the created deformed layers and comparing them with actual rail
- Creating and trialling a cyclic loading test set-up for running fatigue crack growth test and defining the test conditions needed

1.3 Novelty and impact

The key novelty from the work is:

- A method for controlled creation of a deformed layer in pearlitic rail steel using a high pressure torsion approach that emulates that found on a rail or wheel surface
- A method for extracting a sub-scale fatigue crack growth specimen from the deformed layer allowing the possibility of crack path studies through the deformed layer that will help understanding of rail rolling contact fatigue issues.

The work can help in developing improved models of crack growth and wear in wheels and rails as well as providing a means to test new wheel and rail steels.

1.4 Thesis overview

Chapter 2 contains wheel-rail characteristics while Chapter 3 contains the literature review which was conducted to try and identify suitable test methods to create a deformed layer representative of those in wheel and rail material and for assessing crack growth in samples made from the layer.

Chapter 4 contains the design work which was carried out to develop the set-up for a high pressure torsion (HPT) test approach for creating a deformed layer representative of that on wheels and rails and for a fatigue crack growth (FCG) test to assess properties of specimens taken from the deformed layer. In this chapter, constant value for "m" and "C" needed for the Paris equation were derived.

Chapter 5 contains the work done on the high pressure torsion experiment designed in the previous chapter. In this chapter metallurgical analysis was conducted which reveals the extent of the presence of the deformed layer within the processed high pressure torsion sample as well as the hardness values as a result of the process. A comparison between the processed high pressure torsion disc and twin disc and in-service material was also conducted in this chapter.

Chapter 6 outlines the attempt to set-up and run a FCG test. Issues encountered are detailed and methods for overcoming this.

Chapter 7 contains the conclusions from the work.

.

2 WHEEL-RAIL INTERFACE

2.1 Introduction

The wheel-rail interface is relatively small (approximately 1cm^2), but at very high load so the material beneath it is locally above its yield stress. This, along with the high shear stress resulting from friction in the interface means that plastic deformation occurs creating a highly deformed layer at the surface of the wheel and rail where damage such as wear and rolling contact fatigue originates. This section covers conditions involved in the creation of this layer which accounts for the change in properties compared to that of the bulk wheel or rail material.

2.2 Contact mechanics

There is cyclic loading of material at the wheel-rail interface as the wheel travels over the rail. This leads to a large amount of pressure on the rail within a very small area resulting in the profile of both wheel and rail changing with time as well as creation of the deformed layer due to the refinement of the material microstructure. This is especially the case when there is a lateral shift in the wheel due to curves on the track or wear leading to creation of a profile different to when the rail was first installed. The wear process tends to occur in the newly created deformed layer which contains heavily refined grains which are now completely different to those within the original bulk material.

There are three regions of contact between the rail and the wheel as shown in Figure 1 and the pressure exerted varies depending on the condition of the rail head and the wheel as well as track as the position will be different between a straight track and a curved track. Due to the tendency for wheel and rail material to wear. The maximum pressure “p_0” can be calculated using the Hertz elliptical contact approach (Equation 1):

$$p_0 = \frac{3P}{2\pi ab} \qquad \text{Equation 1}$$

Where a is the width and b is the length of the contact ellipse and P is the applied force.

This is due to the elliptical shape that arises at the wheel-rail interface as shown in Figure 1a. This was generated using pressure sensitive film applied to the contact patch (Dwyer-Joyce *et al.*, 2009).

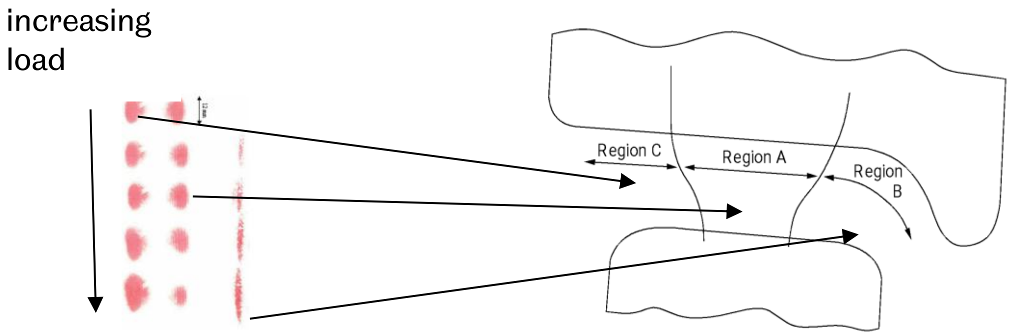

Figure 1: Wheel-rail contact: (a) associated8 contact patch area (Dwyer-Joyce *et al.*, 2009); (b) contact regions (Tournay, 2001)

The size of the contact patch varies with pressure. Increasing the pressure increases the size of the contact patch. This is shown in Figure 1a as you move down the image.

The three main contact regions are:

Contact Region A – This is the region which is the most common in straight and curved tracks. The role of poor friction can manifest itself by cracks forming at the surface; other defects that can be accounted for here are squats.

Contact Region B – This section is a lot smaller than contact A and experiences extreme stresses. This is where gauge corner cracks can occur as a result of the stress conditions.

Contact Region C – Contact in this region is less likely, but not impossible. In the event of a contact occurring in this region; it is likely to experience high levels of stress as well.

The contact between wheel and rail typically has a 10mm diameter with contact pressure as high as 2700MPa (Lewis and Olofsson, 2009); This is high and exceeds the yield stress of the wheel and rail material. This leads to processes like ratcheting and shakedown taking place within the material which will be discussed later. Due to the loads being exerted, there can be a tremendous amount of shear stress generated, with the point of peak stress being just below the surface.

The stress leads to plastic deformation taking place due to the accompanying strain. The continuous passage of wheels leads to plastic strain accumulation and eventual formation of a crack after all the plasticity within the material has been exhausted. This is shown in Figure 2. If the stress is below the elastic shakedown limit of the steel when this process is taking place, this is called elastic shakedown. In this region, the material undergoes plastic deformation and can take a high cyclic fatigue before failure occurs. The plastic shakedown limit is higher than the material's yield strength as it is due to the material being cold worked by the stress being applied. When the stress is above the elastic shakedown limit, but below the plastic shakedown limit; the material undergoes plastic flow. The number of cycles needed before damage can occur is much less when compared to elastic shakedown.

There is a third scenario where the stress is substantially higher than the plastic shakedown limit; here there is an accumulation of plastic deformation with every cycle. This process is called ratcheting. In this instance, the cycles needed before damage is substantially less than what is needed in elastic and plastic shakedown.

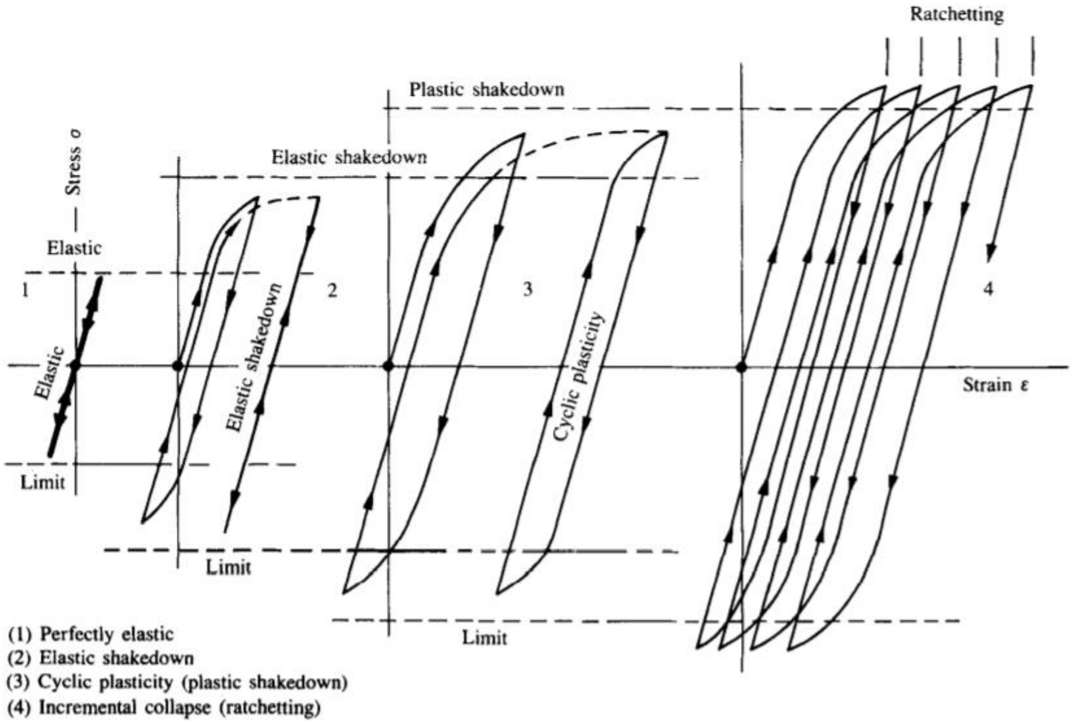

Figure 2: Cyclic material response (Johnson, 1989)

The strain accumulation can be related to the exponential law of fatigue which can be used to assess the strain life relation of the material (Mitchell, 2018).

$$\frac{\Delta\varepsilon}{2} = \frac{\sigma_f}{E}(N_f)^b + \varepsilon_f(2N_f)^c = Strain\ life\ relation \qquad \text{Equation 2}$$

Where σ_f is the fatigue strength coefficient, N_f is the reversals to failure, ε_f is fatigue ductility, c is the fatigue ductility exponent, E is the Young's modulus of the material and b is the fatigue strength exponent. This approach is utilised in modelling rolling contact fatigue (RCF) within the material (Trummer, Marte, Dietmaier, *et al.*, 2016).

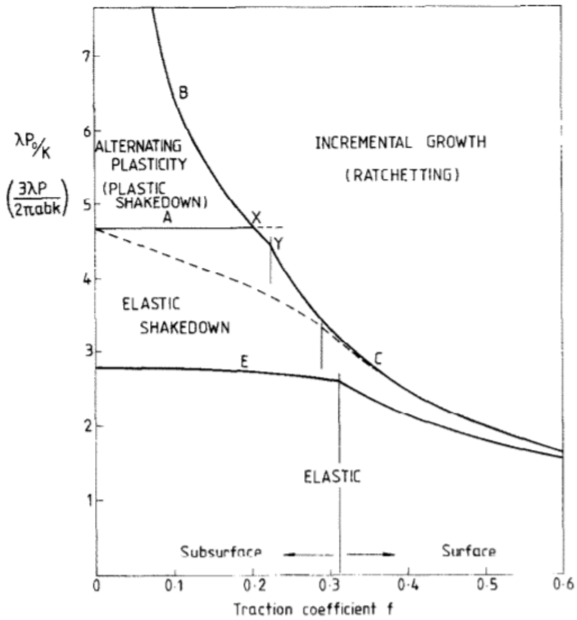

Figure 3: Shakedown map (Ponter, Hearle and Johnson, 1985)

The processes of elastic shakedown, plastic shakedown and ratcheting all lead to damage occurring within the material as well as the formation of cracks and wear in addition to the creation of wear debris as a result of the interaction between the wheel and the rail. This is shown in Figure 3. Ratcheting tends to be most severe in region B in Figure 1 due the high lateral forces as a train passes through a curve, but it will also occur on the rail head in Region A.

2.3 Creep force relationship

Creep in this context is how much faster or slower the wheel is turning relative to pure rolling. As stated in Figure 1, there are 3 contact points between the wheel and the rail. In each contact position different coefficients of friction would be expected. To reduce energy consumption and damage in Region A, an intermediate friction level (0.2-0.3 is desired. This can be achieved through application of a top-of-rail friction modifier. In region B low friction is desired and achieved through application of grease in curves. In pure rolling, there is no friction in the wheel/rail interface.

Creep is usually expressed as a percentage. Experiments done with varying creep are typically conducted in a twin disc apparatus, which will be discussed later in this review. Creep is calculated using the following equation for this situation (Petersen *et al.*, 2000):

$$Creep = 200\frac{R_{top}S_{top}-R_{bottom}S_{bottom}}{R_{top}S_{top}+R_{bottom}S_{bottom}} \quad \text{Equation 3}$$

Where R_{top} is the radius of the disc made from rail or wheel material and S is the speed of the rail or wheel material.

In pure rolling, the stress distribution takes the shape as shown in Figure 4 in the elliptical contact patch.

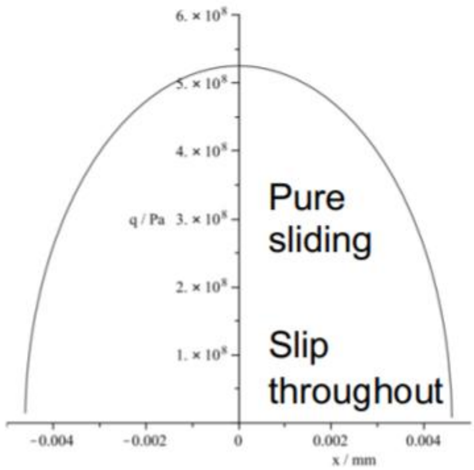

Figure 4: Contact stress distribution in an elliptical contact (Fletcher, 2019a)

The reality is that Figure 4 is not the case as some part of the wheel/interface will stick while the other part slips depending on the amount of tractive force, as shown in Figure 5. So, in summary some part of it will be rolling-slip while the other part will be rolling-stick.

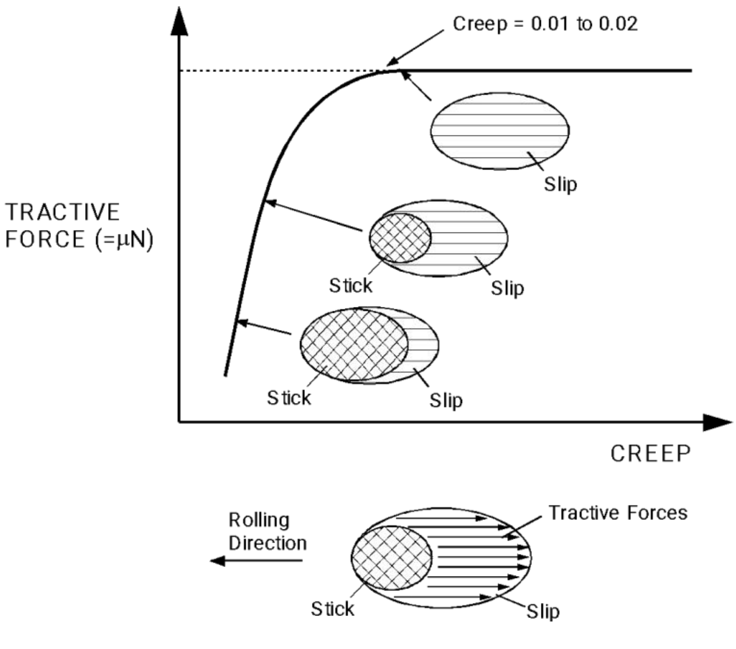

Figure 5: Traction and creep diagram (Lewis and Olofsson, 2009)

The increase in the tractive force eventually leads to full slip in the contact area. In this case, traction coefficient and friction coefficient are the same. Creep curves, such as shown in Figure 5, illustrate the creep/traction relationship. These can be created for different interface conditions, which gives an insight into what is going on in the contact patch. Low friction conditions like wet surfaces lead to a reduction in the traction force present between the wheel and the rail as shown in Figure 6 (Fletcher and Lewis, 2013). This also leads to slip saturation occurring at a lower slip value.

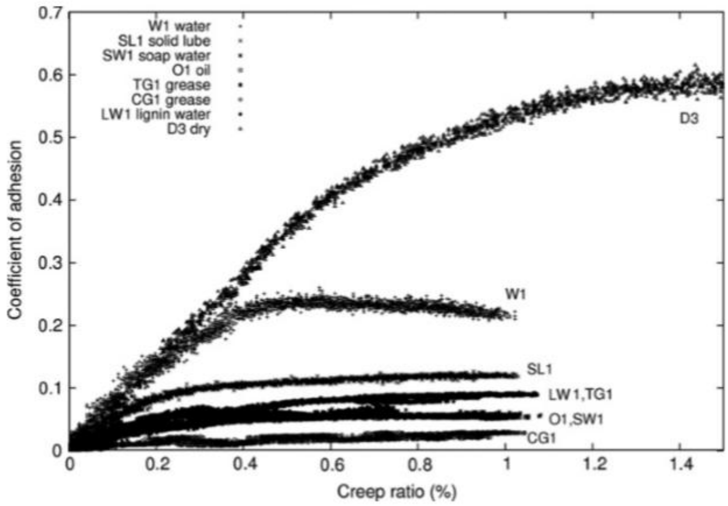

Figure 6: Effect of lubricants/surface conditions on creep force relationships (Fletcher and Lewis, 2013)

High creep can be because of wheel slipping due to low friction contamination. High creep contributes to the formation of white etching layer and will lead to higher wear and possible rolling contact fatigue. This will be discussed later in this literature review in the deformed layer and white etching layer section.

2.4 Controlling friction

From Figure 3, it is evident that the friction level between the wheel and rail influences the damage occurring as well as where it occurs. When the friction coefficient is greater than 0.3 the damage begins to move towards the surface (as the point of peak shear stress rises). The coefficient of friction between two unlubricated steel surfaces is around 0.5, as shown in Figure 7. This immediately places the material in the ratcheting region when viewed in Figure 3. The use of top-of-rail friction modifiers or curve lubricants has the ability to reduce the friction coefficient to between 0.1 – 0.3 (Carrell, 2019).

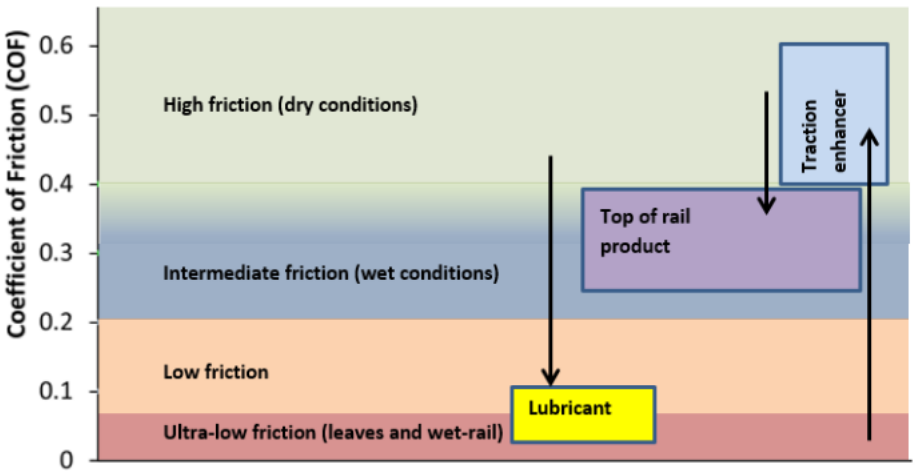

Figure 7: Wheel-rail friction regimes and actions required of friction management products

This brings the material back into the safe operating zone in the shakedown map. This effect of friction modifiers is shown in Figure 7. Top-of-rail friction modifiers, lubricants and sand are used to control the level of friction on the track. Figure 8 shows the effect of using top of rail friction modifiers on R260 rail material. It is evident that the use of friction modifiers reduces wear and rolling contacting fatigue cracks due to the change in the position in the shakedown map of the material when friction modifiers are introduced into the wheel-rail system. The friction modifiers help to reduce the amount of shear stress being experienced by the material as well as the amount of deformed layer formed at the interface. This would explain the reduction in the ratcheting effect of the material as well as reduction in rolling contact fatigue and wear as shown in Figure 8a for wear rate reduction and 8b shows the location on the rail from which the reading was taken.

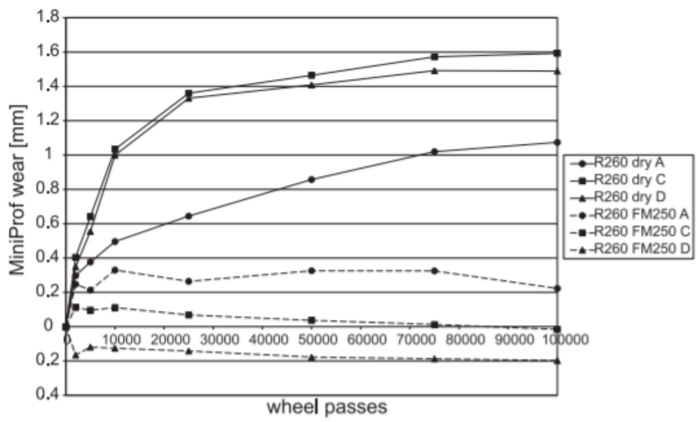

(a)

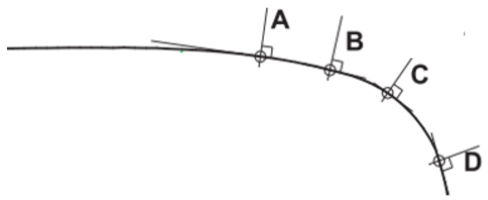

(b)

Figure 8: (a) Effect of friction modifiers on wear rate; (b) Location of measurements (Stock *et al.*, 2011)

Another way top of rail friction modifiers can help is in producing positive creep curves as shown in Figure 9.

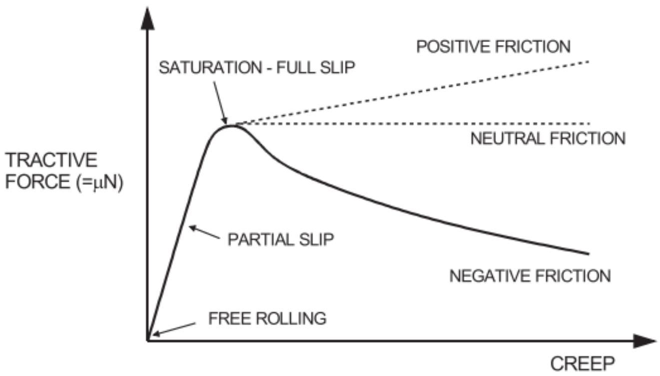

Figure 9: Various friction situations (Harmon and Lewis, 2016)

Figure 6 shows the creep curve for possible surface contaminants. One of the most abundant surface contaminants is water. This can come on to the surface through rain or through precipitation on a cold day. The presence of water reduces the friction as shown in Figure 6. The presence of grease on the track gives a much severe friction drop than water, but as stated earlier, its application is carried out to reduce wear at the gauge corner of the rail, so this is the desired effect.

To combat the detrimental effect of these surface contaminants the use of friction modifiers or traction enhancers becomes necessary. This is to provide a continuous increase in friction as creep rises, avoiding the drop seen in dry situations at higher slips due to temperature effects. This can lead to the same friction level being associated with two creep values. The ensuing instability can cause corrugations to form on the rail.

Whilst the creep curve shows a saturation with the presence of different surface contaminants; the presence of certain substances can lead to negative (reducing) friction occurring between the wheel and rail interface as shown in Figures 9a. In this situation, the wheel is going faster than the rail. The application of a high friction modifier can be used to alleviate the situation, as shown in Figure 10b.

(a)
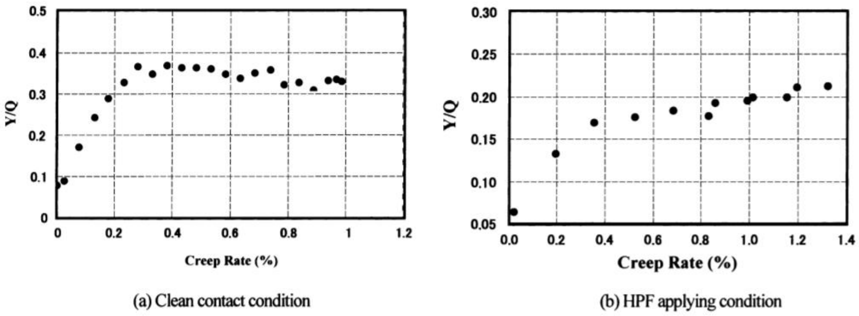

(b)
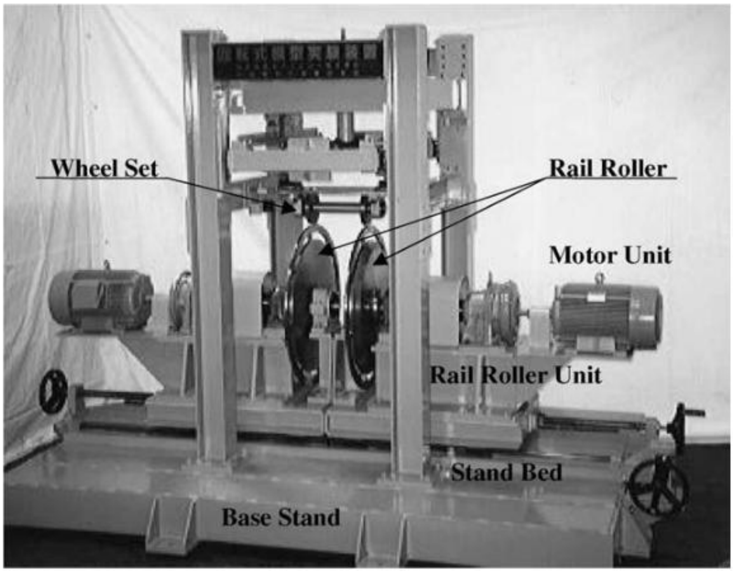

Figure 10: (a) Effect of applying friction modifier for traction (Matsumoto *et al.*, 2002) Y is the lateral force and Q is vertical force; (b) test set-up

Figure 10b shows the effects of high positive friction modifiers. This application delays the onset of creep saturation which is when the entire contact point becomes one of rolling-slip.

As well as reducing the effect of wear and cracks, it can also be used to control friction on the top of rails in instances where there are other bodies on the track that alter the state of friction to levels which are undesirable. An example of this is leaves on the track which can impede traction thereby leading to more rolling-sliding due to the alteration of the friction co-efficient. The leaves on the track leads to the formation of a third body layer on the top of rail surface. It is this third body layer which leads to the reduction friction between the wheel and the rail thereby acting as a lubricant on the rail surface in this scenario as shown in Figure 11 (Gallardo-Hernandez and Lewis, 2008). This affects both braking and traction and becomes a safety issue.

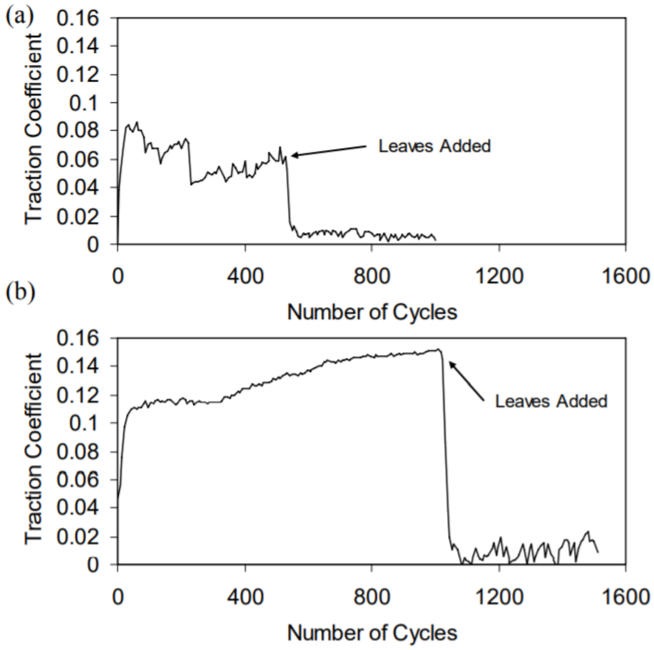

Figure 11: Effect of leaves on traction coefficient (Gallardo-Hernandez and Lewis, 2008)

The effects of the leaves can be overcome by using a positive or very high positive friction modifier or a cheap alternative like sand can be applied to restore the traction coefficient lost because of the leaves on the track as shown in Figure 12.

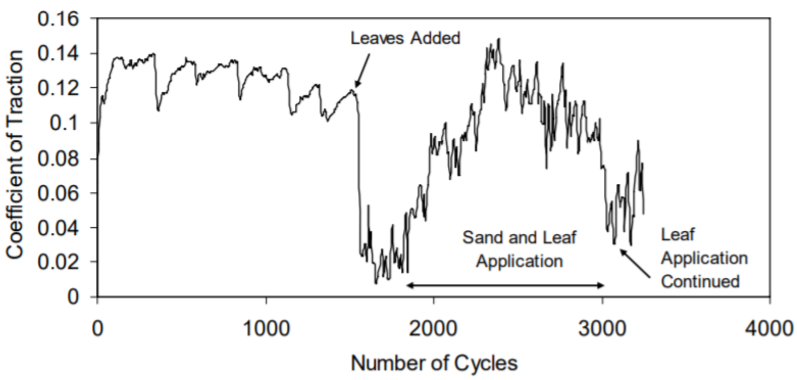

Figure 12: Effects of sand on leafy tracks (Gallardo-Hernandez and Lewis, 2008)

Top-of-rail friction modifiers (FMs) tend to be fluids that contain suspension of other solids that alter the friction condition between the wheel and the rail. In the case of the fluid friction modifiers, the fluids can be oil based, water based or a mixture of both. For the water-based FM, the water evaporates when it is applied leaving behind the solid particles. This then leads to the formation of a third body layer which interacts with wear debris and oxides the wheel and the rail leading to the creation of a new friction condition compared to before it was introduced. In the oil-based FM, there is no evaporation taking place as instead the oil containing the particles behaves as the FM.

The presence of friction modifiers help to alter the creep conditions (Wang *et al.*, 2017) which in turn influences the fatigue crack propagation and wear rate of the wheel-rail system by reducing the shear stress at the surface.

Depending on the type of FM used, their application can accelerate the growth of pre-existing cracks formed as a result of the ratcheting process (Hardwick, Lewis and Stock, 2017). The use of liquid-based FM would lead to more RCF due to the hydrostatic pressure exerted at the crack tip when the wheel rolls over with the liquid still present. This is shown in Figures 13. This issue is not present when solid type friction modifiers are used (Hardwick, Lewis and Stock, 2017).

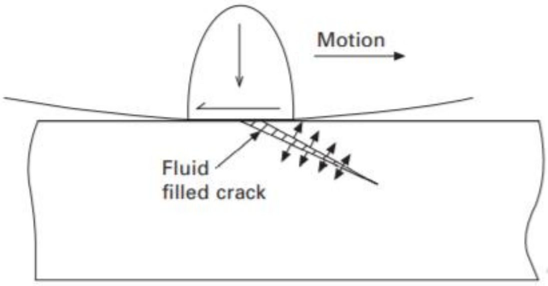

Figures 13: Effects of fluid in pre-existing cracks (Lewis and Olofsson, 2009)

Even with the above potential negative effect with liquid type friction modifiers, their application is still encouraged as they still can reduce the damage at the top of rail or gauge corner cracks if they are applied from the start of the material installation.

2.5 Summary

From the above research it is evident that the wheel-rail interface is a very complex area to fully understand. This is because the contact pressures have on the material to the effect of the friction having on the location in which peak pressure occurs within the contact patch. The role of friction is further compounded by having third bodies present which can either be intentional like, as in the case of lubricants and top-of-rail friction products to unintentional products like leaves and oxide on the track. The presence of these third bodies reduces the shear stress experienced at the interface which reduces the thickness of the deformed layer further increasing the difficulty of being able to extract a viable sample to be studied in the laboratory. The research in this project was focussed solely on the material deformation and how much of the deformed material is present which can be replicated in a controlled environment.

3 LITERATURE REVIEW

The aim of the literature review was to develop an understanding of topics related to the research being carried out including rail metallurgy and the nature of the deformed layer formed on the surface of wheels and rails due to shear stresses resulting from traction in the interface; rail rolling contact fatigue and wear mechanisms; testing approaches for creating deformed layers and sub-scale approaches for assessing crack growth.

3.1 Metallurgy and microstructure of wheel and rail material

Table 1 below shows some of the typical chemical contents of the various rail steels used in the UK and Europe, while Table 2 shows some wheel materials used. This is not an exhaustive list; other rail chemistries are also available, as described in BS-EN13674-2. This work was focused on pearlitic rail grades R260, R350HT and R400HT. R350HT is a heat-treated version of R260. It tends to be used in regions where high wear rates can occur. These can be around curves or on heavy haul freight lines. It has a higher hardness level due to the resulting heat treatment. R400HT on the other hand as shown in the table below is a rail grade with a higher carbon level. This is more expensive and as a result reserved for use in heavy freight lines due to the high wear resistance and resistance to crack formation needed.

Table 1: Chemical composition of different wheel and rail materials (Bevan *et al.*, 2020)

Elements	**R220**	**R260**	**R350HT**	**R370CrHT**	**R400HT**	**Bainitic rail B320**	**Bainitic rail B360**
C	0.50-0.60	0.60-0.82	0.70-0.82	0.68-0.84	0.88-1.07	0.15 - 0.25	0.25 - 0.35
Si	0.20-0.60	0.13-0.60	0.13-0.60	0.38-1.02	0.18-0.62	1-1.50	1-1.50
Mn	1.00-1.25	0.65-1.25	0.65-1.25	0.65-1.15	0.95-1.35	1.4-1.70	1.4 - 1.7
S	0.008 - 0.030	0.008-0.030	<0.030	<0.025	0.025		
P	0.03	0.03	<0.025	<0.025	0.025		

Cr	0.15	0.15	<0.15	0.36-0.65	0.3	0.30 - 0.70	0.3 – 0.7
Mo	0.02	0.02					
Ni	0.1	0.1					
Cu	0.15	0.15					
Al	0.004	0.004	<0.004	<0.004	0.004		
V	0.03	0.03	<0.030	<0.030	0.03		
Ti	0.025	0.025					
N	0.008	0.01	<0.010	<0.010			
O	0.002	0.002					
B							
Hardness (HB)	220-260	260 – 300	350 – 390	370-410	400-440	320 minimum	360 minimum
UTS (MPa)	770	880	1175	1280	1280	1100	1200

Table 2: Chemistry of wheel materials in accordance with BS EN 13674-2

	ER6	ER7	ER8	ER9
C	0.48	0.52	0.56	0.60
Si	0.40	0.40	0.40	0.40
Mn	0.75	0.80	0.80	0.80
P	0.020	0.020	0.020	0.020
S	0.015	0.015	0.015	0.015
Cr	0.30	0.30	0.30	0.30
Cu	0.30	0.30	0.30	0.30
Mo	0.08	0.08	0.08	0.08
Ni	0.30	0.30	0.30	0.30

V	0.06	0.06	0.06	0.06
Hardness (HB)	225 minimum	235 minimum	244 minimum	255 minimum
UTS (MPa)	780 – 900	820-940	860-980	900-1050

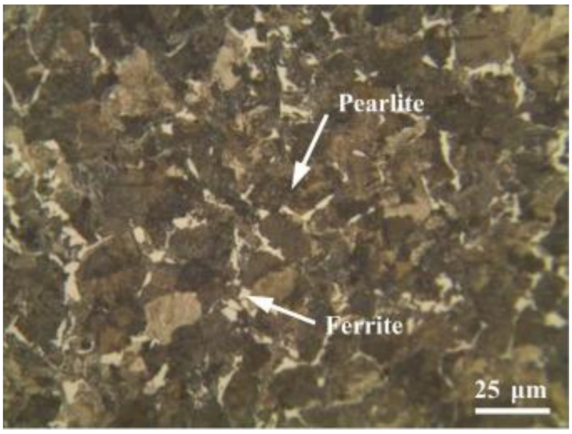

Figure 14: E8 wheel microstructure (He *et al.*, 2016)

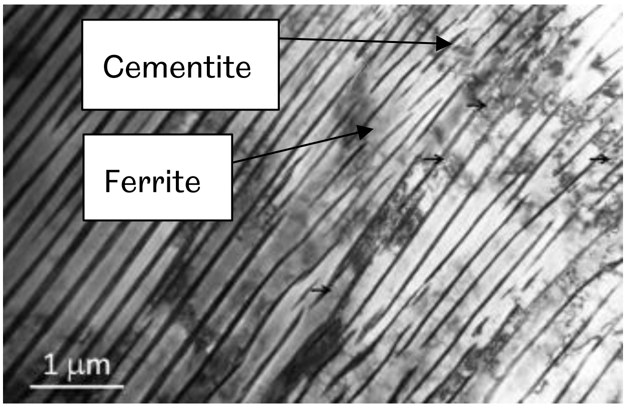

Figure 15: R260 microstructure (the black arrows indicate dislocations present) (Nikas *et al.*, 2018)

The microstructures in Figures 14 and 15 are from E8 wheel and R260 rail materials. Both R260 and E8 are regarded as hypoeutectoid steels due to the carbon levels which are less than 0.83% which is the eutectoid level for steel. Above this point the phase composition typically becomes one of pearlite and cementite and are regarded as hypereutectoid steels since the carbon levels are above the eutectoid content. Ferrite is a phase of iron which contains 0.02% carbon and cementite is iron carbide (Fe_3C) while pearlite is a phase which contains alternative rows of ferrite and cementite as shown in figure 8 when zoomed in. These are formed because of the cooling cycle which leads to the formation of the ferrite and pearlite microstructure. The dislocations are the primary means through which the strain is accumulated when stress is applied. This is from a virgin microstructure and will look different after being plastically deformed.

The microstructure produced is dependent on the steel chemistry as well as the heat treatment performed. However, the grades for this research are predominantly pearlitic in nature and so look similar. The difference is only apparent when their mechanical properties are considered.

Figure 16 is an image of a R350HT which is a heat-treated version of R260.

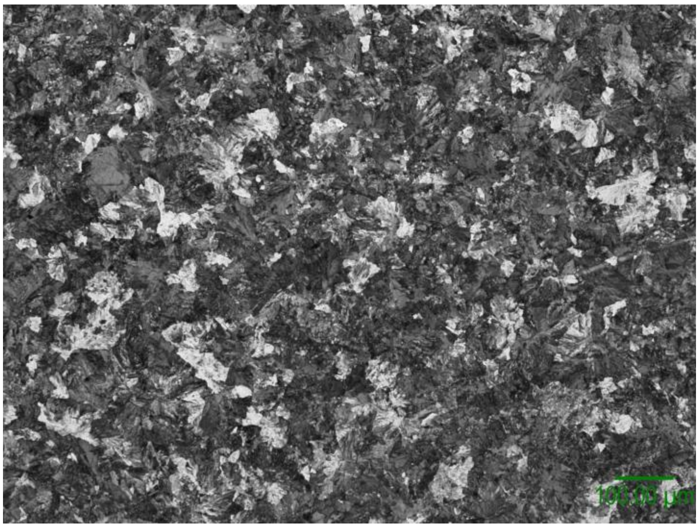

Figure 16: R350HT rail microstructure

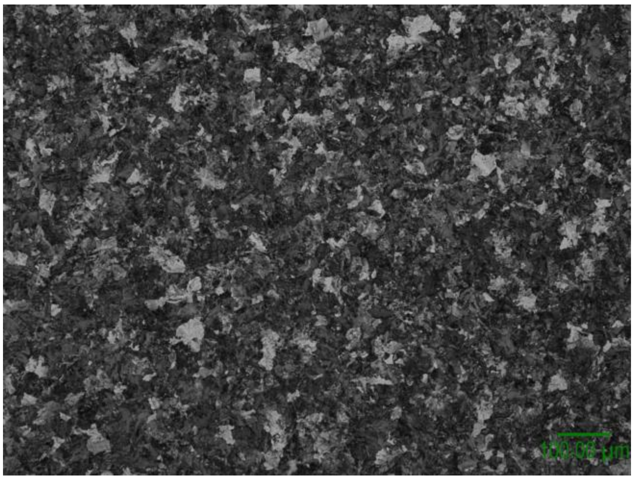

Figure 17: R400HT Rail microstructure

The production of pearlitic rail steels involves the standard normalised heat treatment after the steel making process to achieve the ferrite and pearlite microstructure. However, from Table 1; the grades with "HT" assigned to them indicate heat treated. This is why R350HT has the same chemistry as R260, but with a higher hardness level. The microstructure for R350HT is one that has undergone a forced cooling rate. Figure 17 is a hyper eutectoid steel due to its higher carbon content. From the image when compared to Figure 16, the grain size appears slightly smaller. The small grain size in Figure 17 coupled with its higher carbon level contributes to its higher hardness and strength.

The steel making process is accompanied by secondary steel refining involving degassing to reducing oxygen and hydrogen as well as sulphur as these can be detrimental to the steel quality in terms of steel cleanness and thus affect fracture mechanics due to the presence of inclusions. The presence of inclusions within the steel act as initiation sites for cracks and stress raisers (Hashimoto *et al.*, 2012) (Garnham and Davis, 2011) thus the presence of inclusions affects the fracture mechanics of the material which can make an otherwise ductile material act in a brittle manner.

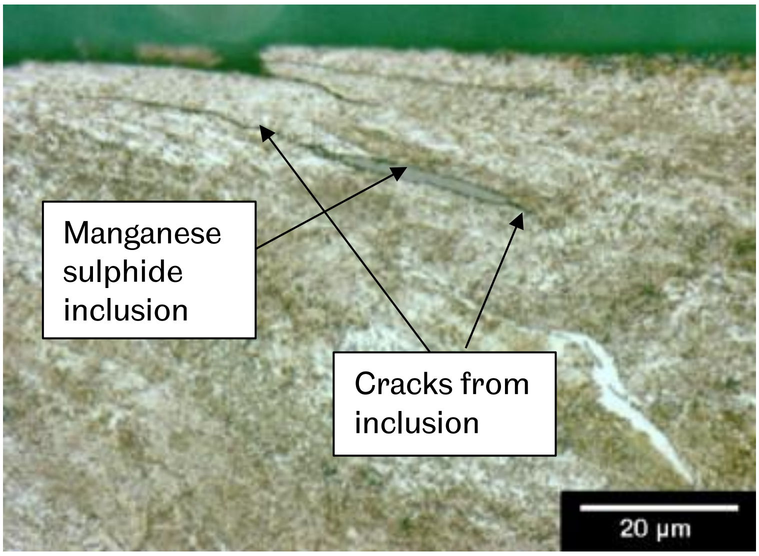

Figure 18: Cracks emanating from a manganese sulphide inclusion (Garnham and Davis, 2011)

This is especially the case for sulphur which is already known to cause anisotropy behaviour within materials (Barbangelo, 1985) (Cyril and Fatemi, 2009) (ASM committee, 1996). Anisotropy is when you have different behaviour in different directions and can be inherent in the material. Severely plastically deformed material can introduce another element to this due to the directionality of the grains due to the process.

The presence of sulphur reacts with manganese to form manganese sulphide which tends to accumulate at the grain boundaries of the material. Figure 18 shows the formation of a crack at a manganese sulphide inclusion site from a twin disc experiment.

A large percentage of sulphur leads to an increase in the volume fraction of sulphides present (Cyril and Fatemi, 2009) and therefore crack initiation sites (Barbangelo,

1985) (Maya-Johnson, Felipe Santa and Toro, 2017). The sulphides also accelerate crack growth rate as well as increase wear rate as shown in Figure 19 using a twin disc approach (Fegredo *et al.*, 1988).

Inclusions of any kind are not welcome in the steel microstructure and can be because of issues arising during the steel making process. Typical inclusions are referenced in ASTM E45 as well as BSEN 13674-1 are predominantly oxides and sulphides.

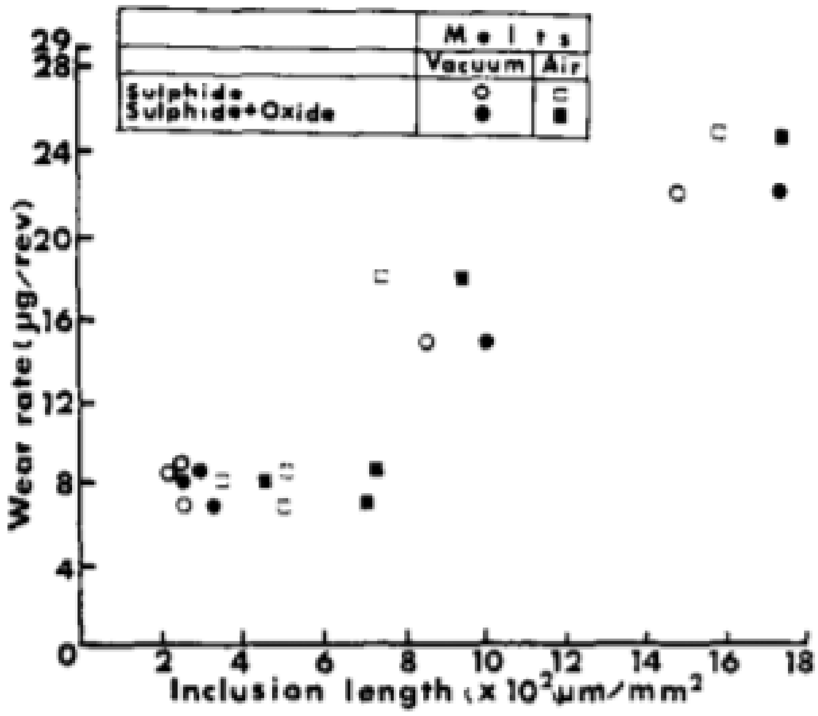

(a)

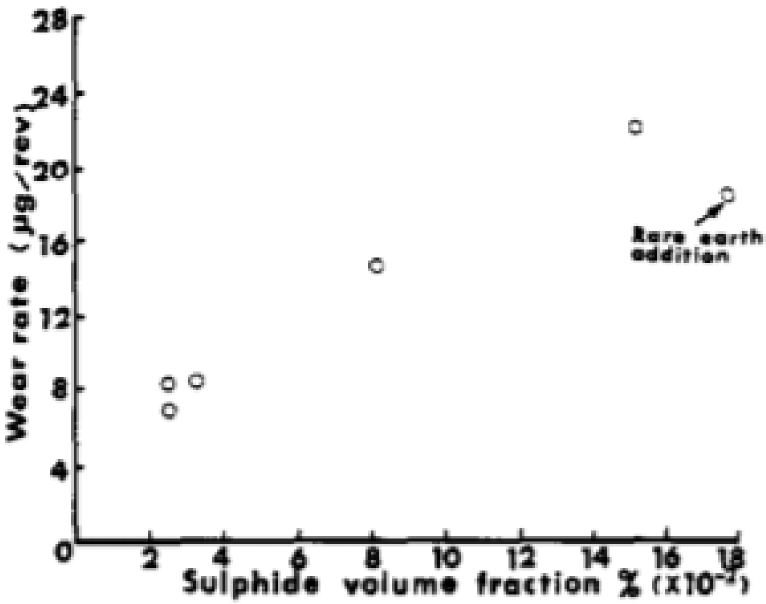

(b)

Figure 19: Wear rate against: (a) sulphide length and (b) volume fraction (Fegredo *et al.*, 1988)

The mechanism by which the wear takes place is linked to dislocation interaction with the inclusions or cracks emanating from the inclusions due to the large stress.

Given the alignment of the sulphide inclusion in line with the shear pattern observed by the rest of the microstructure in Figure 18, it appears it is deformed just like the rest of the microstructure. Given the sulphur level present within the steel grades used for wheel and rail production can be as high as 0.025% for rail and 0.015% for wheel as indicated in BS EN 13647 and BS EN 13674-2 respectively, this can influence the anisotropy behaviour as it already shows this in the production material. Anisotropy is the process by which the material exhibits different behaviour in different directions. High sulphur content leads to an increase in volume fraction (Cyril and Fatemi, 2009) as well as length and size of sulphide inclusions present within the steel (Hashimoto *et al.*, 2012).

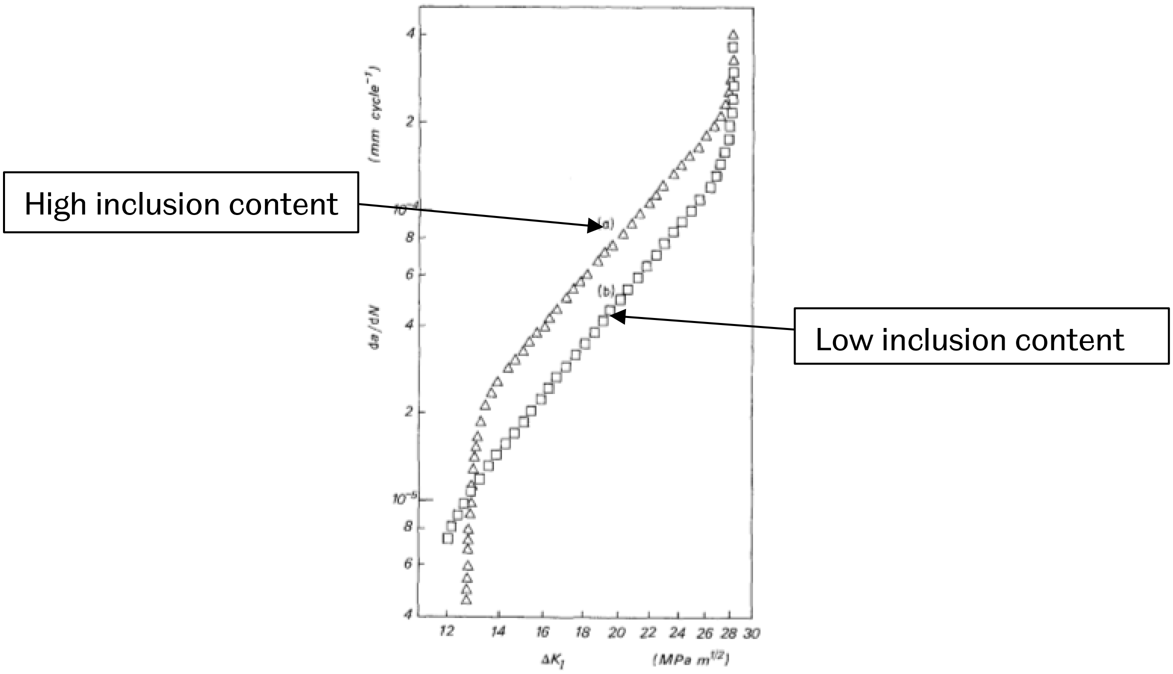

Figure 20: Effects on inclusion content on FGC rate (Barbangelo, 1985)

Figure 20 shows the effect high inclusion content has on the fatigue crack propagation behaviour in a material. The fatigue crack growth (FCG) process will be discussed later in this review.

The anisotropy in the starting material can be reduced by decreasing the levels of sulphur present thereby reducing the volume fraction of sulphide inclusion within the material and in turn affecting the fracture mechanics of the material. However, the reduction of sulphur can raise an issue with hydrogen cracking in the case of wheel production so hydrogen treatment could be introduced to address this concern.

The use of inclusion modifiers to reduce the deformation behaviour of the inclusions also reduces the degree of anisotropy in the fatigue propagation behaviour of this steel (Wilson, 1976). This inclusion modification is done by adding calcium during the refining process.

Whilst this is the case for sulphur; the presence of other inclusions like oxides will likely give a different appearance in the microstructure. An example is alumina which is hard and therefore will not align with the rest of the microstructure like its sulphide counterpart.

The production of the wheel involves closed die forging, rolling and then an isothermal heat treatment should a bainitic microstructure be sought, provided one of the various bainitic chemistries is met. If the pearlitic grade (E8) is used, then the material is air cooled and then machined. It is also possible to harden and temper the steel to increase the hardness. Similar steel making practise used on the rail is also applied here as inclusions can be detrimental.

In the case of bainitic rail steels, the microstructure can be formed by simply air cooling like the normal production route for R260 for some chemistries. However, in some cases an isothermal treatment is sometimes required to allow the formation of bainite. This involves cooling the material down to just above the martensite start temperature and held for an appropriate amount of time that conforms to the TTT diagram to allow for the transformation of austenite to bainite and then air cooled. The diagram in Figure 21 shows an example of an isothermal heat treatment used (Messaadi, Oomen and Kumar, 2019). It is worth noting that in some cases the transformation from austenite to bainite is not complete and as a result there is retained austenite within the microstructure which can play a significant role in the material performance.

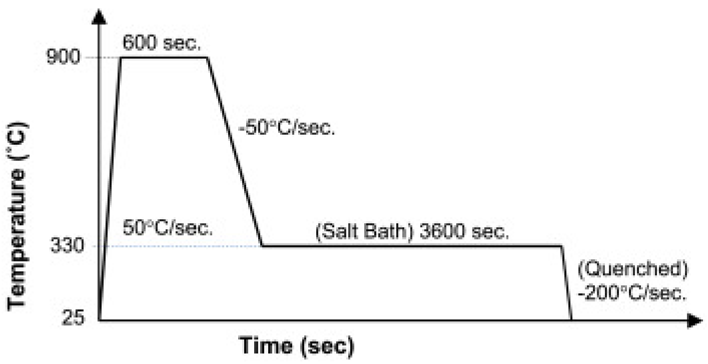

Figure 21: Bainitic heat treatment cycle (Messaadi, Oomen and Kumar, 2019)

Due to the range of chemistry that can be achieved; the hardenability of the material is affected as it shows the ease with which the material forms Martensite. This has to be considered in cases where heat treatment is carried out. To minimise the wear rate, it is worth making the hardness of the wheel similar to the hardness of the rail (Liu *et al.*, 2016). This can be achieved by hardening and tempering as stated earlier.

3.1.1 White etching layer

Due to the frictional energy at the surface between the wheel and rail, heat is generated. In some scenarios, the heat generated can be sufficiently high enough to transform the microstructure into austenite and white etching layers can appear (see Figure 22(a)). For this transformation to occur, the transformation temperature of 723°C must be exceeded. Temperatures as high as 1050°C can be achieved at the wheel-rail interface thereby causing the transformation to occur (Bernsteiner *et al.*, 2016). This leads to the transformation of the steel from body centred cubic ferrite to face centred cubic structure austenite phase as shown in Figure 22(b).

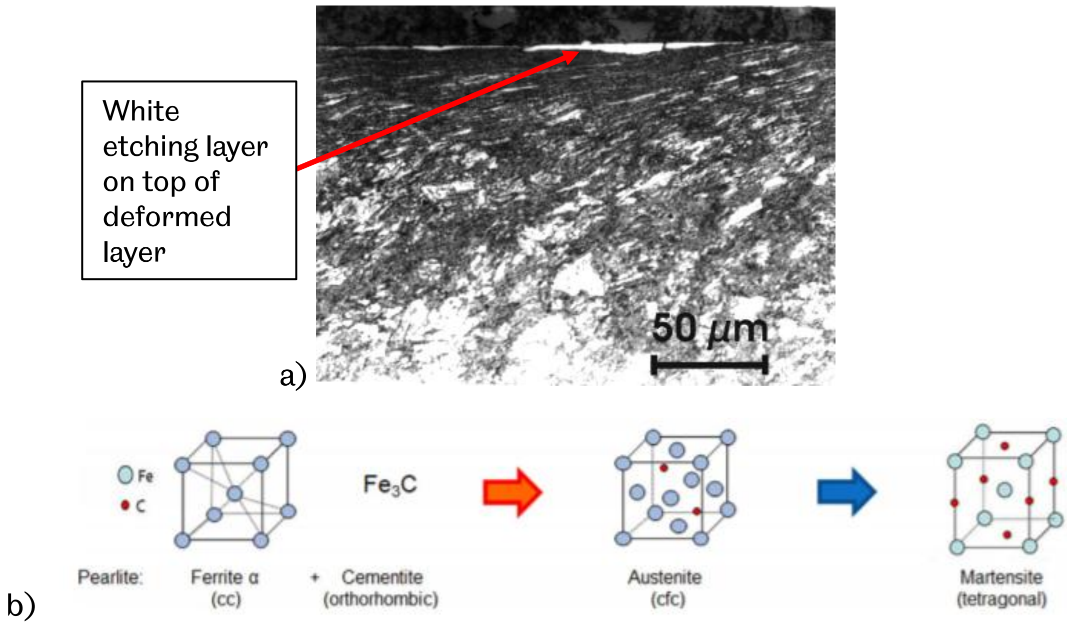

Figures 22: (a) WEL (Pointner, 2008); (b) formation of BCT martensite (Vargolici *et al.*, 2016)

There is an increase in cooling rate which then leads to the transformation of body centred tetragonal martensite as shown in Figure 22(b).

This is hard and generally brittle in nature if un-tempered, which is the case here. This can be the source of cracks on the rail due to the change in the crystal volume fraction associated with the metallurgical transformation (see for example, Figure 23).

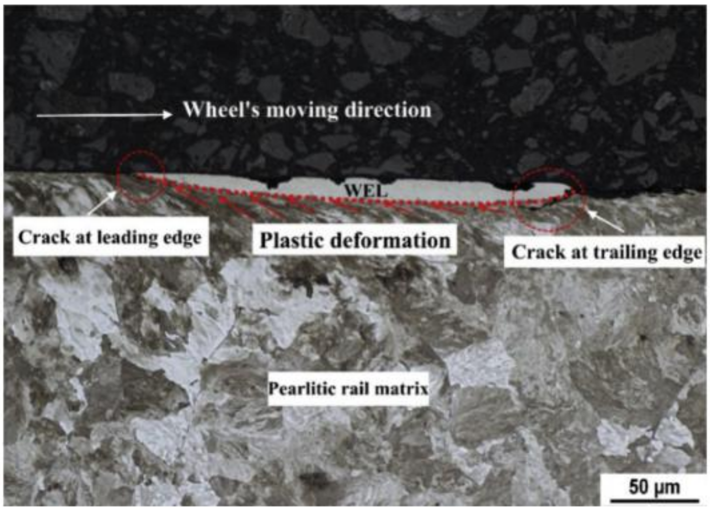

Figure 23: White etching layer with cracks originating from it (Lian *et al.*, 2019)

The conditions at the wheel-rail interface can encourage the formation of white etching layer if certain requirements are met. These are high creep and high loads which in turn translate to high pressure given the small contact area involved at the wheel-rail interface.

High creep can occur in accelerating or braking or in very sharp curves in the wheel flange/rail gauge corner contact. High creep and the corresponding high friction led to an increase in the temperature being achieved at the wheel-rail interface as well as the depth to which the WEL layer forms. High creep can occur in situations where there is negative traction or creep saturation occurs at a low traction level, as shown in Figure 9.

Figure 10 shows the effect of positive friction modifiers on creep saturation position of the creep curve. Unlike the wheel, the rail is static which means a continuous exposure of heat because of the frictional energy on a particular spot on the rail. This feature of forming a white etching layer is not restricted to just the rail as it is also capable of forming in a wheel. The wheels sliding due to the locking of the wheels when brakes are applied leads to the wheels been heated, leading to the creation of the thermal conditions needed for the transformation to occur.

As stated earlier, the applied load can also affect the formation of a white etching layer. This is expected as it influences the tractive force apparent at the contact patch. A large load leads to an increase in the contact area as well as the pressure as well as early creep saturation. Once again, the wheel flange and gauge corner of the rail are the location for the high pressure due to the small contact area.

3.2 Deformed layer

Due to the loads experienced as well as the small contact area at the wheel-rail interface, the microstructures of both components undergo grain refinement due to the strain the surface of the material experiences, as shown in Figure 24.

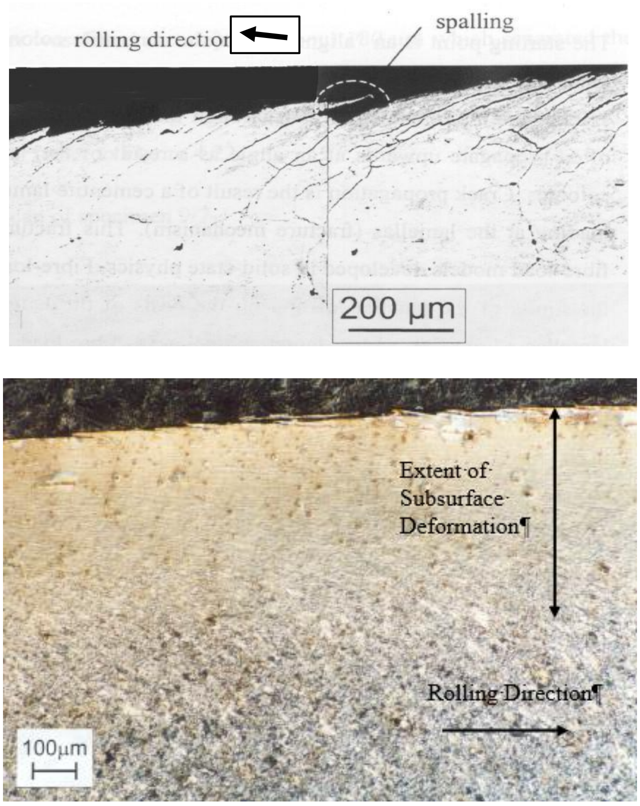

Figure 24: Deformed layers on rail: (a) actual rail (Kapoor, Fletcher & Franklin, 2003) b) wheel material from twin disc test (Beaty *et al.*, 2016)

The refinement leads to an increase in the surface hardness of the material due to the work hardening process. Whilst it is evident that a high carbon level increases the performance in the form of reduced wear and better fatigue resistance (Ueda *et al.*, 2003), this results from the increase in the work hardening rate due to the strain.

Figure 1 shows just how small the contact area is at the flange section compared to regions A and C. This extremely small contact patch on the gauge corner accounts for the catastrophic wear that occurs in this section which will be discussed later.

Approaches have been made to try and quantify the strain the surface of the rail experiences. Modelling done indicates strain levels as high as 10 (Widiyarta *et al.*, 2008) are expected at the surface as shown in Figure 25. This was achieved using the "brick model" (discussed in more detail in section 3.5.4).

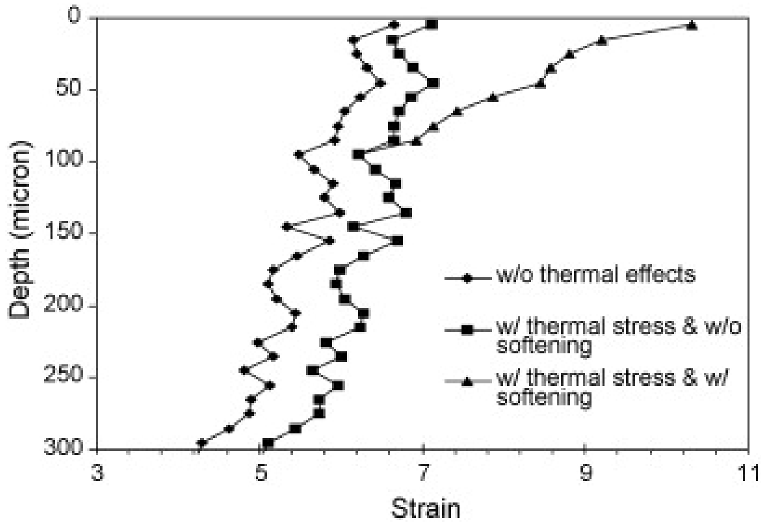

Figure 25: Brick modelling strain levels at surface (Widiyarta, Franklin and Kapoor, 2008)

Other approaches to try and quantify the level of stain indicated strain levels as high as 6 at 10 microns below the surface as indicated in Figure 26a.The approach to identify the strain level involved axially loading a test bar with markings on it is shown in Figure 26b and then rotating it 90 degrees in 60 seconds while maintaining the axial load before relaxing both the axial and torsional loads. This microstructure formed was then compared to samples extracted from track material. The strain of samples matching track material microstructurally as well as hardness levels was then calculated based on the degree of deflection of the lines, as shown in Figure 26b by calculating its tangent of the angle.

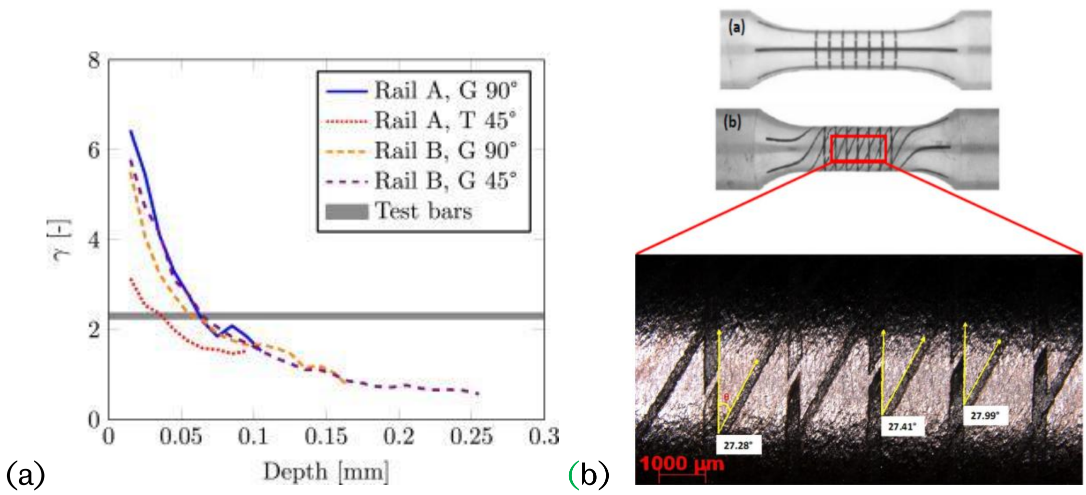

Figure 26: (a) Experimental estimation of strain levels and depth (Meyer *et al.*, 2018); (b) Strain calculation method (Nikas, Zhang and Ahlström, 2018)

The combination of sliding with cyclic loading accounts for the grain refinement at the surface which leads to a hardness gradient set up within the material, as shown in Figure 27 (Larijani *et al.*, 2014).

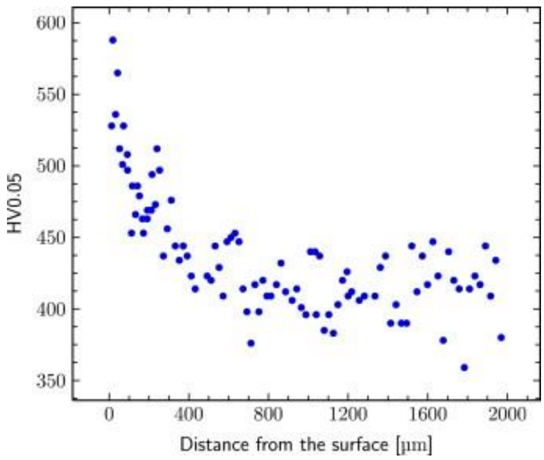

Figure 27: Hardness variation and depth from rail surface on R350HT rail (Larijani *et al.*, 2014)

This leads to a deformed layer that can be up to 1mm in thickness depending on the severity of the contact conditions (Larijani *et al.*, 2014), but varies from the top of rail to the gauge corner due to the extreme contact conditions at the gauge corner, as shown in Figure 1.

The deformed layer is where the various degradation mechanisms initiate and propagate. This is from delamination when the layer has exhausted its ductility due to the extreme strain the material accumulates because of the repetitive loading, to the other wear mechanisms like adhesive, abrasive and oxidation wear. All these lead to a loss of profile which is addressed by grinding of the rail and turning of wheels. As well as change of profile, wheels can suffer out of roundness and rails corrugations which also need to be resolved.

3.3 Test approaches for creating deformed layers

This section covers the techniques that could be used in the experimental work to create the deformed layer as well as investigatory techniques and other testing approaches to be considered during this research.

To assess the properties of the deformed layer described in section 3.2, a review of techniques needed to create material in similar strain conditions as well as testing the associated properties was carried out. Before this can be done, representative material needs to be processed to form a deformed layer identical to that at the wheel-rail interface. To create this, one of the severe plastic deformation (SPD) processes can be used and then fatigue crack growth test samples taken from the processed specimen. The severe plastic deformation techniques currently used are the high pressure torsion process (HPT), the equal channel angular process (ECAP) and accumulative roll bonding (ARB). Of these three SPD techniques, only two have been used so far for creating an SPD sample for investigating the deformed layer in wheel or rail material. They are ECAP (Wetscher *et al.*, 2007) and HPT (Leitner *et al.*, 2019). Both are reviewed here.

Methods for assessing wear and other aspects of material performance are also covered.

3.3.1 High pressure torsion

The layer that experiences plasticity in the rail is usually tens of microns thick and as a result not big enough to take test samples from, thus, a high pressure torsion machine can be used to generate a highly strained layer of material of sufficient quantity to take test samples.

The HPT process creates a microstructure which replicates the surface of the microstructure of the rail or the wheel. The process involves applying pressure to the sample between two anvils and then twisting it. This is shown in Figure 28. This leads to refinement of the grains of the material with the grains aligned in the shear direction which is similar to what occurs at the wheel-rail interface.

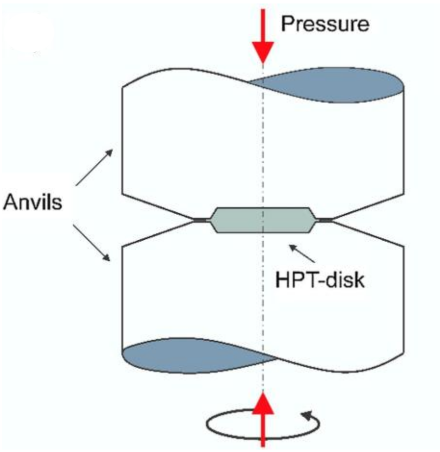

Figure 28: HPT process (Leitner *et al.*, 2019)

The refined grains lead to an increased hardness as well as strength due to the smaller grain size. This is mainly due to the increased number of grains obstructing the movement of dislocations. The grain size is influenced by the distance from the centre of the HPT samples as shown in Figure 29. The prior grain size can also affect the final grain size after processing (Kim *et al.*, 2017). This means care must be taken in selecting the right part of the wheel or rail to extract material from to process in the HPT specimen and in selecting the right part to extract an FCG specimen from in the SPD layer.

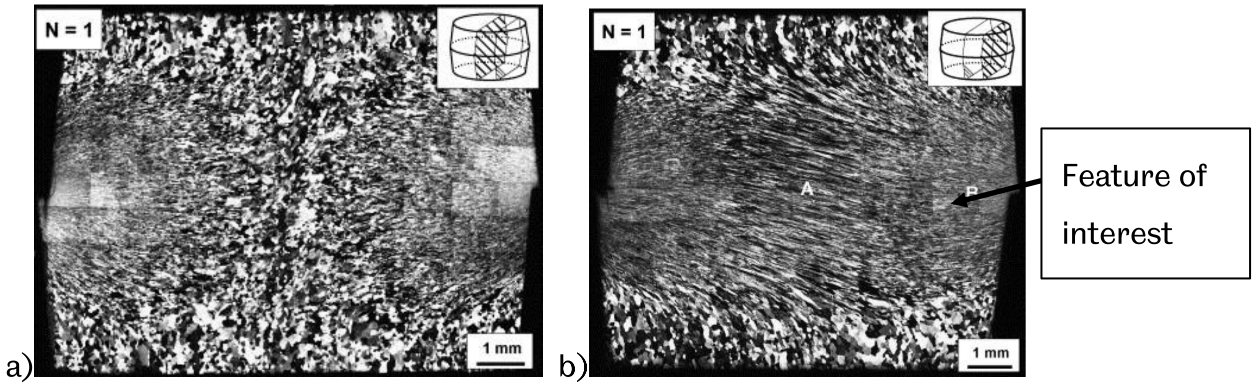

Figure 29: Microstructural and grain orientation at: (a) the centre of an HPT specimen and b) off centre in an HPT specimen (Sakai *et al.*, 2005)

The applied pressure used for R260 has varied when previous research has been reviewed; ranging from 4GPa to 5.6GPa. This may seem inconsequential, but the pressure applied on the material is needed to prevent the material slipping between the anvils during the twisting or rotation. This applied pressure needs to be a minimum of 4.5GPa for steels when a rotation speed of 0.5rpm is used and 5GPa for 1rpm. This is shown in Figure 30. The sample holder or anvil can be further shot blasted to also help prevent slip (Larijani *et al.*, 2015).

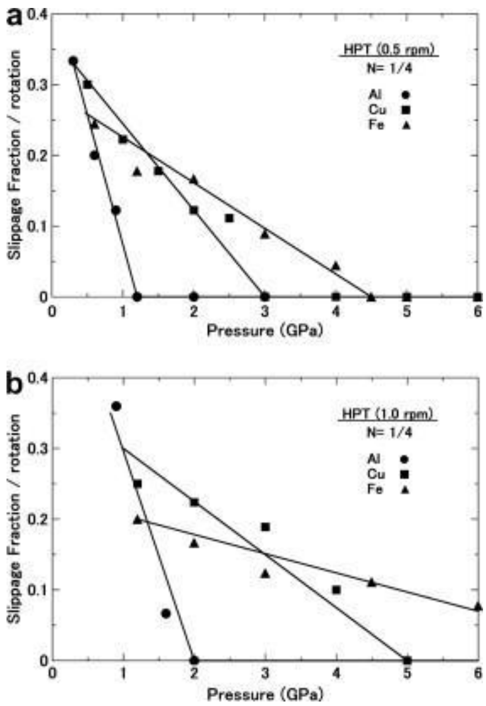

Figure 30: Applied HPT pressure and amount of slippage at (a) 0.5rpm rotational speed and (b) 1rpm (Edalati *et al.*, 2009)

Increases in applied pressure also led to an increase in torque requirement as shown in Figure 31. This was performed on Copper and Armco iron. The torque requirement is significantly higher in Armco iron compared to copper due to its higher tensile strength.

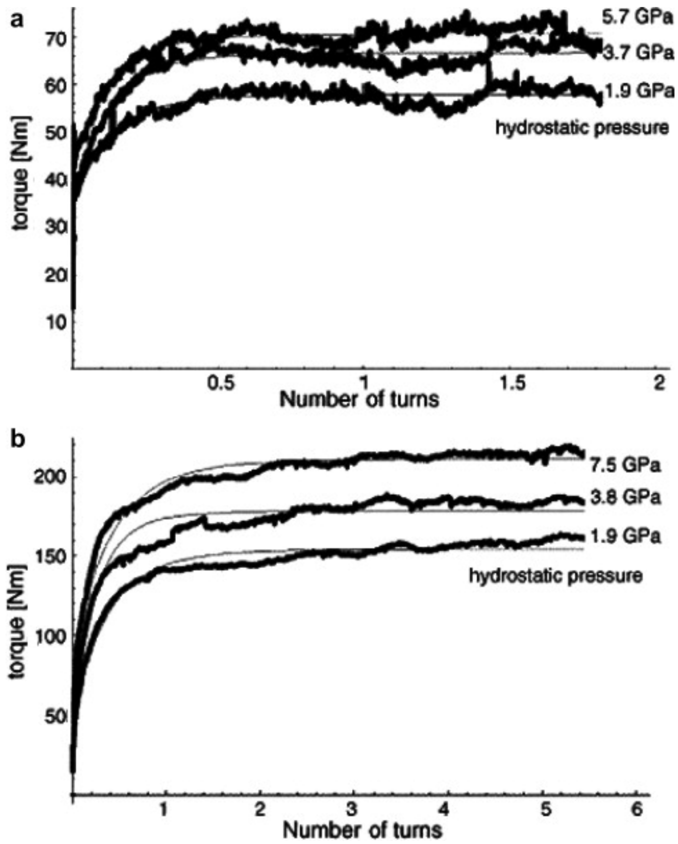

Figure 31: Effects of pressure on torque: (a) is Copper; (b) is Armco Iron (Zhilyaev and Langdon, 2008)

This would be an issue in a situation where there is a limit in the readily available torque.

The torque profile or data can also be used as a processing parameter to confirm the effectiveness of the high pressure torsion process. An increase in torque as the number of turns increases gives an indication into the work hardening of the material as it is being processed.

Another important parameter that has been reported to affect the property profile of the deformed HPT disc is the angle of the anvil wall as well as the depth of the anvil (Lee and Kim, 2014). Previously, the recommendation of the radius to diameter thickness ratio was supposed to be kept to 1/10 (Pippan *et al.*, 2010). Work has been carried out to see if a larger sample could be produced. However, it did show variability of the strain within the sample because of increasing the sample dimensions in the form of different hardness levels as shown in Figure 32. A large

HPT sample leads to an increase in radius to depth ratio which shows an increase in strain variability between the top and the middle part of the sample, as shown in Figure 32.

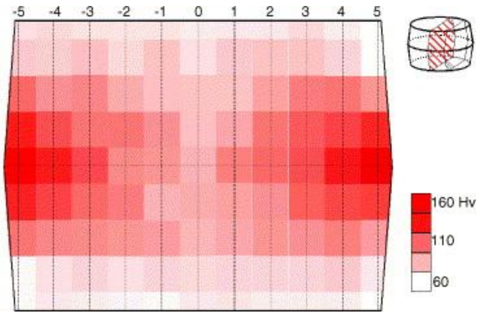

Figure 32: Hardness variation due to strain inhomogeneity (Sakai *et al.*, 2005)

This can be addressed by having a ratio that meets the 1/10 target or is as close as possible. However, this will become unrealistic when larger HPT samples are sought. The variation in grain size is evident in Figure 29. This variation in grain size can also affect the fracture mechanics. Since the grain size varies, it can change the fracture type from one of trans-granular fracture to inter-granular fracture during a test like the FCG test due to the cyclic plastic zone becoming larger or smaller than the grain size depending on the direction of the crack propagation. This feature can also account for crack path deflection as observed in previous research (Leitner *et al.*, 2019). Due to the grain refinement the specimen undergoes after the HPT process, there is a reduction in fracture toughness while there is a corresponding increase in strength and hardness. This is reflected in Figure 33 showing R260 fracture toughness data.

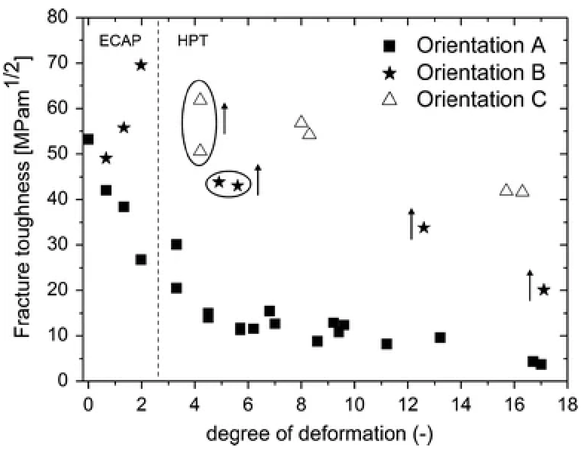

Figure 33: Effects of strain on fracture toughness (Hohenwarter *et al.*, 2011)

From Figure 33, it is evident the fracture toughness reduces as the amount of strain the material undergoes increases. This is also affected by the notch orientation as well as direction in which the crack is travelling as orientation A, from Figure 33, appears to display an exponential drop in fracture toughness compared to the other directions which appear linear.

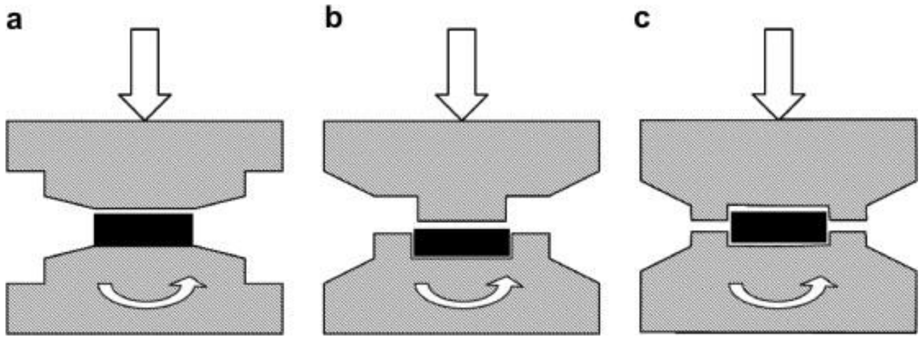

Figure 34: Various types of HPT in use (Zhilyaev and Langdon, 2008)

The diagram in Figure 34 shows the type of HPT designs considered in previous work (Zhilyaev and Langdon, 2008). Figure 34a is an unconstrained HPT device, Figure 34b is a constrained HPT device and Figure 34c is a quasi-constrained HPT device. Over time, different types of HPT design have emerged. Figure 34c is a schematic of the latest design of HPT device being used for this research. The design has a tapered wall which has varied from 5°C (Sakai *et al.*, 2005) to 22°C (Figueiredo *et al.*, 2012) from the literature. However, this parameter is important as it can affect the strain variability within the material, required torque as well as the amount of dead zone material present after processing. Finite element simulations done so far indicate a larger inclination angle gave better response in terms of reduced strain inhomogeneity with 60° showing the best results (Lee and Kim, 2014).

The strain (ɣ) generated within the sample increases with distance from its centre. It can be calculated using the following equation:

$$\gamma = \frac{2\pi r N}{t} \qquad \text{Equation 4}$$

Where "t" is the thickness of the sample, "r" is the radius from which the test specimen or test is taken from, and "N" is the number of revolutions.

The von-Mises strain (ε_{vm}) on the sample can then be calculated using the equation:

$$\varepsilon_{vm} = \frac{\gamma}{\sqrt{3}} \qquad \text{Equation 5}$$

The increased number of turns increases the strain. As the strain increases with every turn, the grain size also reduces with an increase in hardness of the HPT sample since smaller grain size gives higher hardness.

3.3.2 Equal angular channel processing

Equal channel angular processing (ECAP) is another severe plastic deformation technique that has been used for creating a deformed layer for investigating railway material behaviour (Wetscher, Stock and Pippan, 2007). It involves pushing the sample through a die which is at an angle. Figure 36 shows a schematic of an equal angular processing set-up.

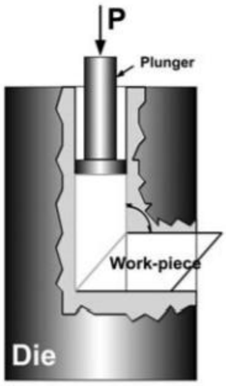

Figure 35: Schematic of equal channel angular process (Lowe and Valiev, 2004)

The angle between the channels dictates the amount of strain the material experiences after one pass. Increasing the number of passes leads to an increase in the amount of strain the material experiences.

$\mathcal{E} = \frac{2}{\sqrt{3}} \cot\left(\frac{\Phi}{2}\right)$ – This gives the strain per path Equation 6

Where Φ is the intersection angle and was 120° when the processing was done. Whilst Equation 6 is for a device which only has one prominent angle, there is another Equation used for the calculation of the strain per pass if there is a curvature present within the tool, as shown in Figure 36.

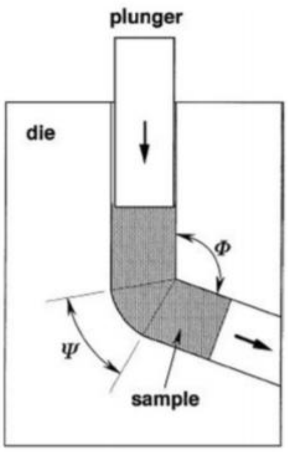

Figure 36: Curved ECAP tool design (Arun Kumar *et al.*, 2019)

The total strain, $\mathcal{E}_n$ for Figure 37 can be calculated using (Roodposhti *et al.*, 2015):

$$\varepsilon_n = \frac{N}{\sqrt{3}}\left[2cot\left(\frac{\phi}{2} + \frac{\Psi}{2}\right) + \Psi cosec\left(\frac{\phi}{2} + \frac{\Psi}{2}\right)\right] \quad \text{Equation 7}$$

Where *N* is the number of passes.

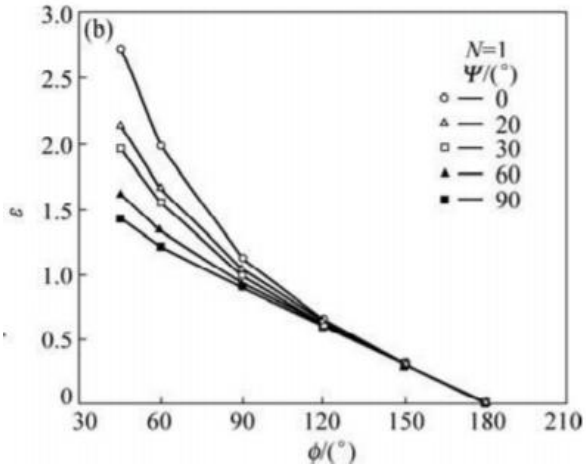

Figure 37: Strain and angle relationship (Roodposhti *et al.*, 2015).

Figure 37 shows the amount of strain imposed on the material in one pass. It is evident that the smaller the angle the larger the strain the material experiences.

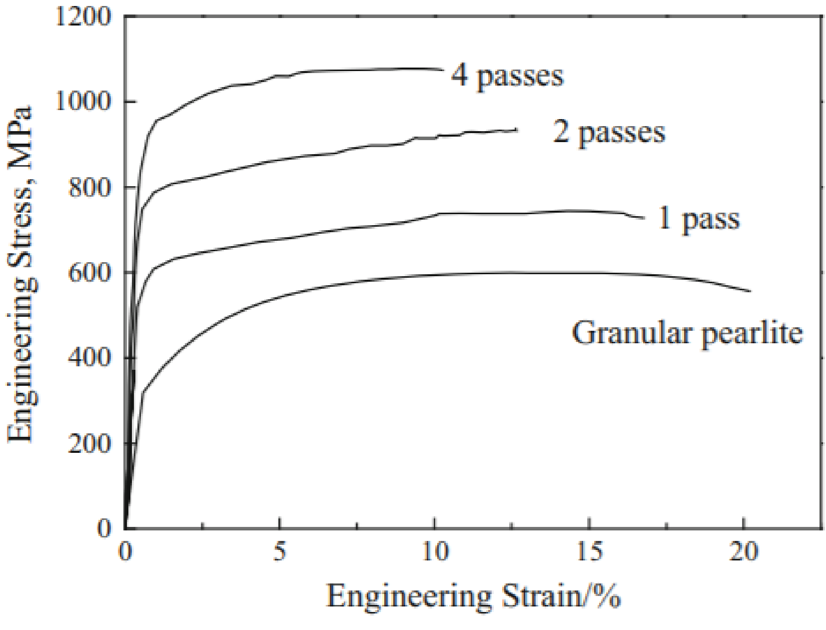

Figure 38: Number of passes and strength (Xiong *et al.*, 2015)

Like every other SPD technique, the process leads to refinement of the grains within the material because of the strain it experiences, this leads to a change in properties, an example of which is the mechanical strength (Xiong *et al.*, 2015), as shown in Figure 38.The increase in strength in the processed material is due to the smaller grain size formed.

There are various routes involved in processing using the ECAP approach. These are shown in Figure 39.

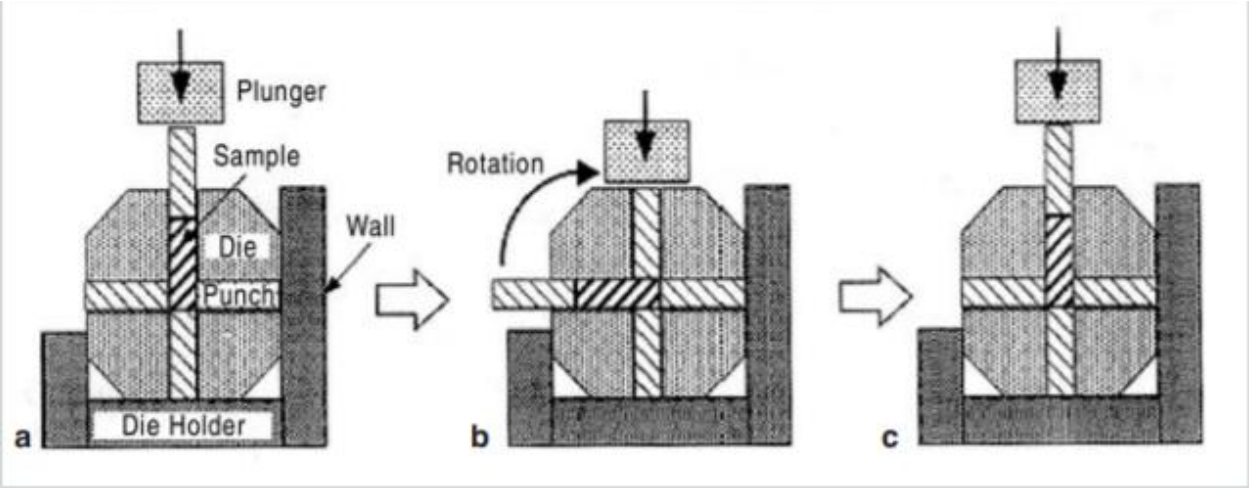

Figure 39: ECAP processing routes (Lowe and Valiev, 2004)

This is due to the way the material is processed having an effect on the properties afterwards as well as the microstructure. It was concluded that rotating the material 90° in the same direction as it was processed gave the best properties (Furukawa *et al.*, 1998). This is known as the B_c route. It produces a more equiaxed microstructure in all directions compared to the other routes. It is not known if this was applied in previous work done on R260 material where tensile and fracture toughness were studied. This could explain the strange behaviour displayed in terms of fracture toughness where there appear to be an increase in the fracture toughness of material compared to before it was processed. The increase could be as a result of the crack going against the principal deformation plan where all the grains are aligned (Wetscher *et al.*, 2007).

Whilst it is an impressive processing technique, indications are that ECAP is not capable of administering the high strains levels that can be achieved in the high pressure torsion (Arun Kumar *et al.*, 2019).

There is no significant cross-sectional change within the material after going through this process in addition to the fact that the strain calculated is for the entire ECAP specimen. The deformed layer has a variation in the amount of strain experienced at each level as you move away from the head of the rail. Therefore, an ECAP specimen could reflect a deformed layer at a particular strain level, but it will not be representative of the variation in properties or grain size from the deformed layer into the component. This is generally represented by the variation in hardness that arises from the wheel-rail interaction. The maximum strain achieved was 2 (Wetscher, Stock and Pippan, 2007). This is significantly less than the strain of 6 or higher reported at the rail head. This means the technique is not suitable for this research.

3.3.3 Twin disc approach

Wear assessment can be carried out using a twin disc rig in a laboratory environment, as shown in Figure 40. This comprises of two discs made of wheel and rail material and rotated at different speeds to achieve the required level of partial slip. Realistic contact pressures are achieved through the hydraulic loading jack incorporated.

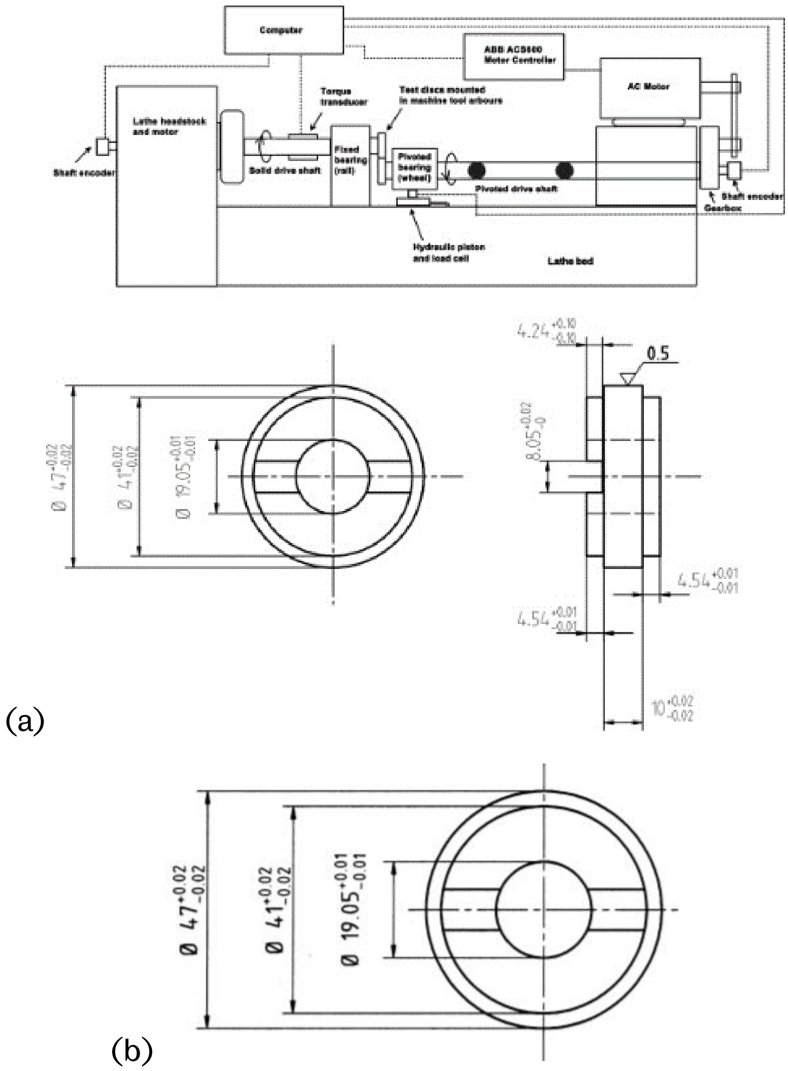

Figure 40: (a) Twin disc machine layout and (b) Twin disc dimensions (Fletcher and Lewis, 2013)

The mass of the discs is checked before and after testing to assess the amount of wear that has taken place. The wear debris is also reviewed under the microscope to ascertain the type of wear that is occurring between the two samples due to the different creep. This is a small-scale approach thus not a completely true reflection of what could occur on the track when different contact profiles are factored in. As a result, a full-scale rig is needed to verify the findings of the twin disc assessment. There are various types of full-scale rigs that are in use. The linear rig shown in Figure 41(a) (Stock and Pippan, 2014) has been used in previous investigations. Figure 41(b) shows a similar type of full-scale rail rig used at the University of Sheffield.

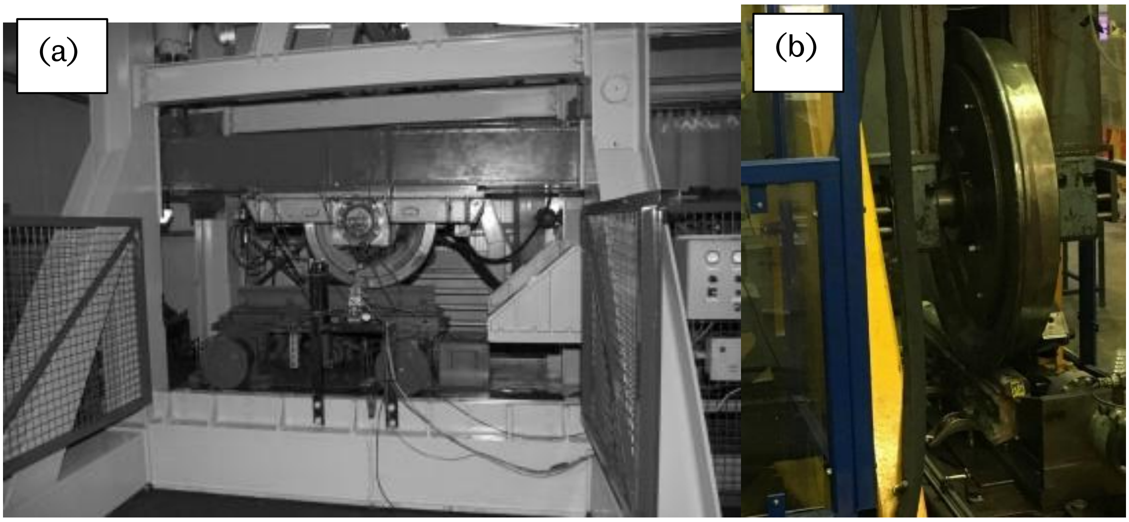

Figure 41: (a) Linear full scale rig at voestalpine (Stock *et al.*, 2011); (b) full scale rig at University of Sheffield

These full-scale rigs consist of a wheel identical to that found on a train as well as an actual length of rail. A load is applied on the wheel and it the rail is pulled underneath it. In the University of Sheffield rig the wheel is also pulled slightly to achieve the desired slip. The rail moves at a speed which lower than that seen on track.

Whilst the full-scale rig and twin disc approaches can create severe plastically deformed layers similar to in-service conditions, these processes are not well controlled and repeatable in addition to the fact that the geometry is not good for extraction of the fatigue crack growth test samples to be used for this research.

Pin-on-disc testing is another approach that can be used to assess the wear rate of the wheel or rail steel component. This was the basis on which the Archard wear formula was generated (Archard, 1986).

$$\frac{V}{L} = \frac{KW}{P_m} \qquad \text{Equation 8}$$

Where V is the worn volume in a sliding distance L, K is the wear coefficient, p_m is the hardness of the of the softer of the two materials in contact and W is the normal load.

As the name implies, it involves a pin (typically made of wheel material) under a load sliding against a disc (typically made of rail material.

Rolling contact fatigue testing is done in a similar fashion to the twin disc wear testing but also utilises a non-destructive examination approach to detect the onset of the formation of cracks which is often accelerated by the application of water. Eddy currents are typically utilised to detect the formation of cracks (Wang *et al.*, 2017).

3.4 Sub-size testing

Given the size of the deformed layer, research into historic sub size specimen is needed. Whilst previous research appears to be the first attempt to conduct the fatigue crack growth test in the deformed layer (Leitner, 2017), this work is actually the first time that shows that the notch is present within the deformed layer.

Several small-scale techniques have been developed, but most are suitable for assessing material properties rather than for conducting fatigue crack growth tests. Also available are micro-cantilever tests. FIB can be used to machine these specimens from the material of interest. Figure 42 shows an example of one machined from a railway wheel to study white etching layers formed (Freisinger *et al.*, 2023).

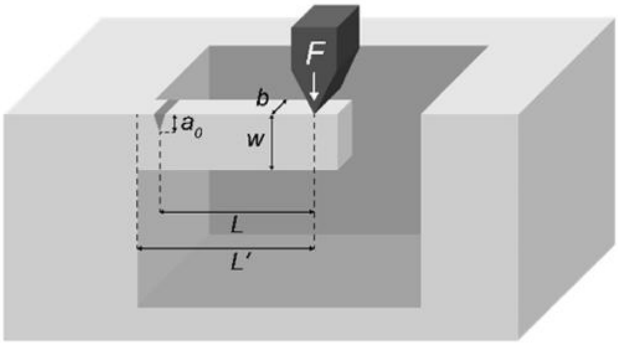

Figure 42: Micro pillar (Freisinger *et al.*, 2023).

Small size dog-bone specimens have also been considered, as shown in Figure 43. The dog-bone had a dimension of 18mm in total length with a square cross section of 1.2mm^2 and the gauge length of 6mm. In light of the new evidence in this research, it is apparent this type of specimen can be considered if a bigger HPT sample as shown above can be processed. However, this would present challenges on how to monitor crack growth given their small size. The C-T sample was picked for this research as it requires less material to manufacture.

Figure 43: Dog bone specimen from processed HPT intended for tensile testing (Larijani, Kammerhofer and Ekh, 2015)

There does not appear to be any restriction to the geometry function quoted in ASTM E647 therefore it can be applied even to the small size specimens. It is not certain if the size of the specimen would present variability in result. However there is speculation about a different crack tip plasticity on full scale C-T samples when compared to other specimen types (Varfolomeev, Luke and Burdack, 2011).

3.4.1 Summary of testing approaches

A full-scale test rig is suitable for creating the deformed layer as well as testing rail products, unfortunately though, the layer created is not big enough for a fatigue crack growth sample to be taken from. In the case of the ECAP, the maximum strain achieved has been reported as 2 (Wetscher, Stock and Pippan, 2007). This is quite small compared to the target of 6 or higher. The high pressure torsion process has the ability to achieve high strains comparable to what is achieved at the interface as the strain is linked to the radius from which the sample is extracted as well as the degree of rotation. This makes it more suitable for this research.

3.5 Damage mechanisms in wheel and rail material

The damage mechanisms the wheel and rail experience are a combination of various mechanisms which include abrasion and adhesion. These are all wear mechanisms that do not account for the microstructural changes the material undergoes due to the excessive pressure. The other mechanisms the material undergoes which can result in possible wear or rolling contact fatigue cracking are the shakedown and ratcheting mechanisms as stated earlier.

Due to the cyclic stress the material undergoes; there is an accumulation of plastic strain for every cycle. This continuous accumulation reaches a threshold and leads to the formation of a crack. This can be below the surface or at the surface depending on the level of friction present between the wheel and the rail as well as whether there are inclusions present. The process also leads to wear of the material.

If material fails at the surface it is lost as wear and a crack may initiate. If material fails sub-surface a crack can initiate.

To further understand how the microstructure evolves as the stress is applied, the various processes will be revisited again and explained in relation to the evolution of the microstructure. From a microstructural point of view, the strain experienced by the material occurs due to dislocations within the material. From the shakedown map, when friction coefficient is below 0.3, the maximum shear stress occurs below the surface. Therefore, during the ratcheting process for a friction of 0.3 and below, the dislocation is moving underneath the surface of the material depending on the load. In the presence of second phase particles these dislocations pile up at the carbide/matrix grain boundary forming a crack or void.

However, prior to ratcheting, elastic shakedown is the first process to occur. This is effectively a cold work operation as it leads to a grain refinement of the material and therefore increases the strength of the material. However, as stated earlier, the strain associated with the applied stress occurs via dislocations. In this event, the elastic shakedown will lead to fracture of carbides or sulphides because of the stress. Figure 42 already shows the presence of manganese sulphide in the steel which can be inevitable given the sulphur levels typically encountered in common rail grades like R260 and wheel steel like E8. The presence of manganese sulphide is especially detrimental at this stage as it also acts as a source of crack initiation within the material. This has been shown in Figure 18 during twin disc experiments. The process can also lead to de-cohesion between manganese sulphide and the matrix as shown in Figure 44. This mechanism is associated with the increased wear rate shown in Figure 19.

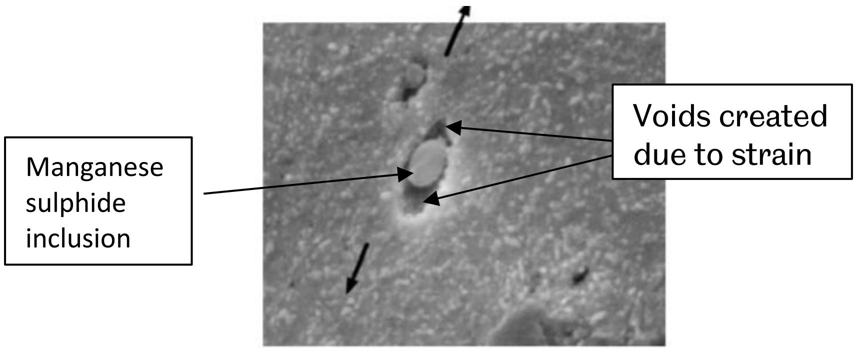

Figure 44: Void formation at an MnS site (Becker *et al.*, 2018)

This leads to the formation of voids present within the material and hence damage occurring at the elastic shakedown stage around the vicinity of a manganese sulphide inclusion. In some instances, where harder inclusions are present, such as alumina, it will lead to crack initiation and growth for every cycle thereafter.

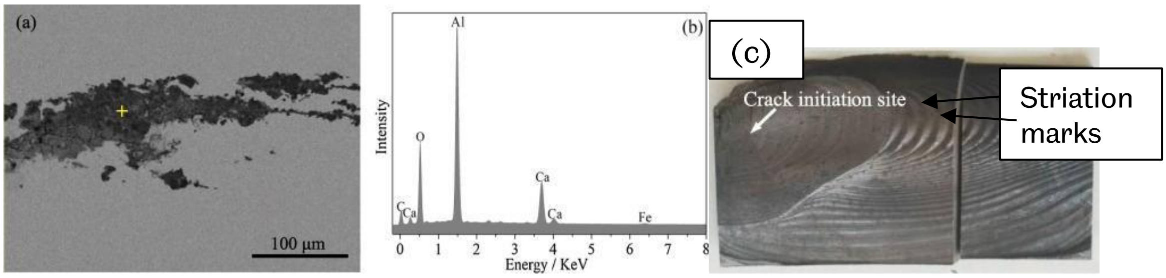

Figure 45: (a) Calcium aluminate inclusion and crack initiation from a scrapped railway wheel; (b) EDAX analysis of inclusion; (c) Fracture surface (Zeng *et al.*, 2020)

Figure 45 shows what appears to be a Calcium aluminate inclusion being the initiation site for a subsurface rolling contact fatigue failure. The striation marks are representative of the number of cyclic load cycles experienced by the wheel and are carried out by dislocations. The inclusion in Figure 45a is a result of the steel making process.

Further strain experienced during the plastic shakedown or ratcheting of the material will lead to the voids continuing to grow until they get to a level where they coalesce leading to propagation of the crack. However, this can be altered by the presence of inclusions as they can influence the direction in which the crack grows fastest as well as the ease with which the crack grows.

One of the criteria for void coalescence is when the distance between the carbide particles is half the length of the void formed; this is assuming the particles are of the same size. The presence of large inclusions like manganese sulphide or oxides inclusions, as shown in Figure 46, alters those criteria leading to an acceleration of this process as well as the direction in which the crack grows.

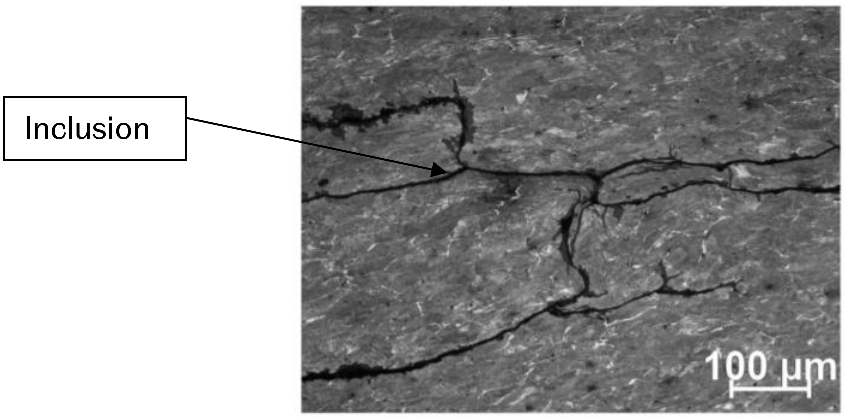

Figure 46: Non-metallic inclusion (Schilke *et al.*, 2014)

The presence of inclusions, as shown in Figure 46, can lead to material peeling off when the component is experiencing high strains, thereby forming wear particles.

From the shakedown map in Figure 3, there is a shift in the shear stress from below the surface towards the surface at a friction level of 0.3. As stated earlier, the coefficient of friction for steel on steel is around 0.55. This puts the peak shear stress at the surface of the material. The strain associated with the stress is still carried out by dislocation; however, in this case there is no material to stop their movement. The dislocations pile-up eventually leading to the formation of a crack at the surface. This leads to head checks if formed at the gauge corner. This makes it necessary to use lubricants to minimise damage as their application can reduce the coefficient of friction to levels or around 0.1 and 0.3. This moves the peak shear stress to below the surface thereby the associated dislocation movement will be below the surface. Although there is still damage occurring, it will be below the surface of the material where it is supported. As stated earlier, the application of friction modifiers reduces the shear stress the material experiences thereby reducing the amount of strain and thus the amount of dislocation moving per cycle. This is how the reduction of wear by friction modifiers occurs.

Due to the high strain experienced, the cracking and de-bonding of carbides and the metal matrix will be next (Becker *et al.*, 2018). This is most likely to occur during the plastic shakedown and ratcheting phase. As a result of this, more cracks will be formed and connect with pre-existing cracks formed at manganese sulphide location.

3.5.1 Wear mechanisms

In the case of the pearlitic steels being used which is most common; the interaction between the wheel and the rail in this instance from the point of view of the Archard principle, is likely to lead to some adhesive wear taking place due to the asperities on the wheel bonding to that on the rail and breaking off to form a new wear surfaces. This is likely to occur at the running in stage.

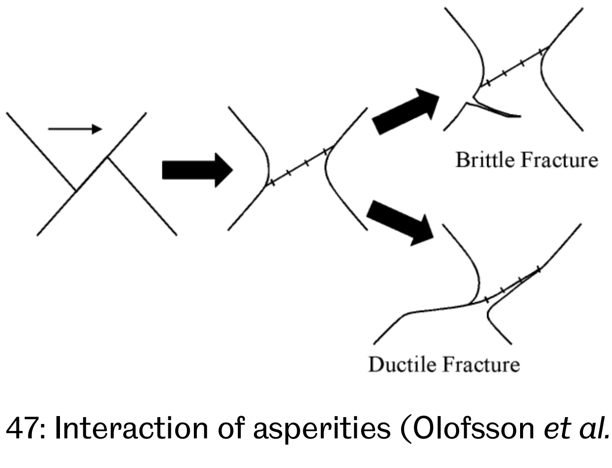

Figure 47: Interaction of asperities (Olofsson *et al.*, 2013)

Figure 47 shows adhesive wear due to the asperities interacting which could be one of the possible mechanisms taking place at the wheel-rail interface.

The presence of friction at the wheel-rail interface leads to an increase in temperature thereby leading to iron oxidising with the atmospheric oxygen available. The mechanism of oxide formation because of exposure of iron to atmospheric oxygen leads is a form of wear as shown in Figure 48. The presence of oxide has already been reported to be present at the early stages of wear (He *et al.*, 2016). This makes it a complex degradation mechanism in play at the wheel-rail interface when it is accounted for along with abrasion.

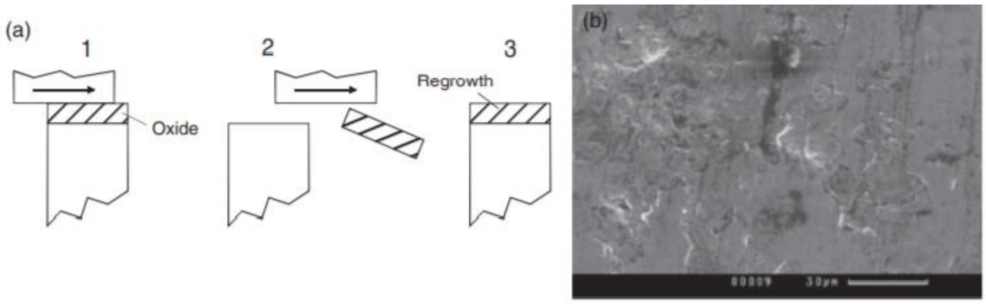

Figure 48: Oxidation wear (Olofsson *et al.*, 2013)

Leaves on the track also have an influence on the degradation mechanism of both fatigue and abrasion (Wang *et al.*, 2017). Leaves on the track alter the friction coefficient as stated earlier, but have also been reported to be able to inflict damage on the material (Gallardo-Hernandez & Lewis, 2008).

In instances where the lower carbon rail steel is used; for example R260, and a higher hardness is required due to high loads or other factors; cladding of the rail with harder material like martensitic stainless steel helps to improve the wear resistance (Lewis *et al.*, 2016), (Lu *et al.*, 2019). However, this is a more expensive approach to improving performance. As a result, heat treating the material can be sufficient to a degree, so consideration could be given to R350HT and R400HT as they have higher hardness levels and as a result will tend to show better wear resistance over R260.

In low friction scenarios which could be the result of leaves on the track or water due to rain, the use of sand to overcome the problem causes damage to the system. This is due to the abrasive wear that ensues as a result of the hard sand particles becoming embedded between the wheel and the rail material (Lewis, 2006). This is due to two mechanisms that become active in the wear process, as shown in Figure 49.

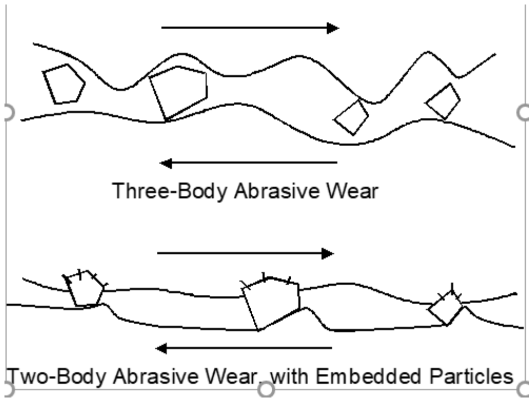

Figure 49: Wear mechanism as a result of third body introduction (Olofsson *et al.*, 2013)

The sand becomes embedded in the wheel or rail material causing 2 body abrasive wear to the opposing surface. This is also while potentially interacting with the wheel and rail in a three-body abrasive wear mechanism scenario.

Delamination and fatigue wear are also mechanisms that take place, as shown in Figure 50. They are both similar in terms of been the result of the exhaustion of the material ductility but differ in appearance. The delamination wear appears as material being peeled off the surface due to the exhaustion of the material ductility due to the repeated load.

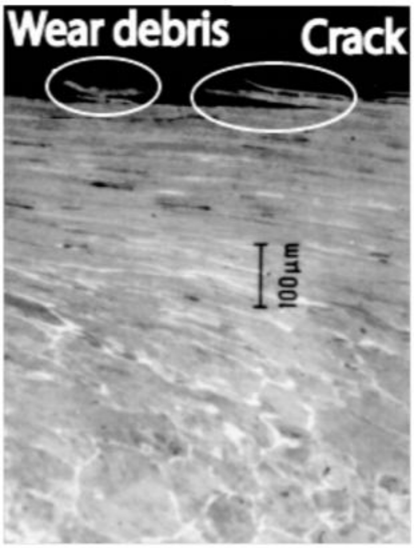

Figure 50: Delamination wear (Fletcher, 2019b)

In the case fatigue wear, the exhaustion in ductility is because of the load being carried out by the asperities. This leads to damage occurring below the surface until cracks link up and a piece of material is removed. This is shown in Figure 51.

Figure 51: Fatigue wear leading to spalling from a wheel (Ekberg and Sotkovszki, 2001)

The principle of both is based on movement of dislocations as explained in the previous section and void coalescence taking place and then the material eventually peeling off when a particular thickness of material is reached.

3.5.2 Interaction between wear and rolling contact fatigue

If the effect of wear on crack propagation is considered (as show in Figure 34a), the crack is truncated as more material is removed. If crack truncation rate is laid over the crack growth rates the net crack growth rate can be determined. In Figure 34b, two different wear rates are considered. If the wear rate (hence crack truncation rate) is high, it is likely that most cracks will be worn away before progressing beyond stage A (cracks driven by ratcheting). If, however, the wear rate is low, cracks will initiate and progress along stage A. They may stabilise at point 1, where growth rate equals truncation rate. These curves will vary considerably with contact conditions and as such the crack may be carried from point 1 to point 2 and then continue propagating. The crack reaches a length at which the growth rate declines, and it stabilises at point 3. If the wear rate drops below the intersection of stages B and C the crack can move to stage C, which may lead to a dangerous conclusion such as a rail break.

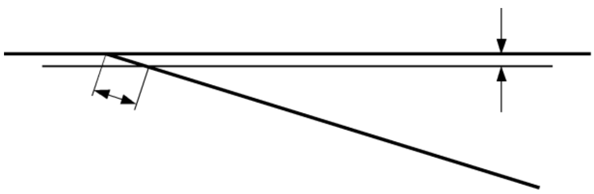

a)

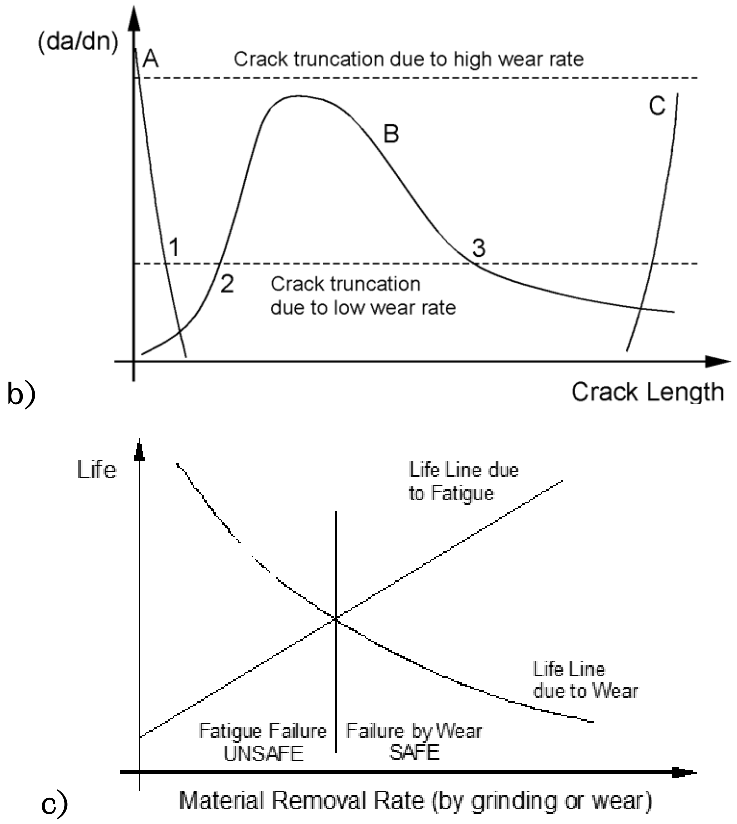

Figure 52: Interaction of wear and fatigue: (a) Crack truncation by wear; (b) Crack growth rate versus crack length; (c) Rail life versus material removal rate (Kapoor *et al.*, 2003)

Figure 52c shows the effect of material removal rate on rail life. This may be reduced by using harder rail or by lubrication. Grinding rail increases the removal rate. Clearly the aim should be to have a removal rate at the optimum point, where the wear and fatigue lines cross. This, however, will be very difficult because of variation in the wheel-rail contact conditions, but with good interface management systems in place a good life can be attained.

As stated earlier, wear of the material can take place through several mechanisms from oxidation due to exposure to the elements to delamination as a result of plasticity exhaustion. Overall, these mechanisms can be in play and can lead to mild, severe or catastrophic wear depending on location at the wheel-rail interface as shown in Figure 53. This was derived from twin disc experiments.

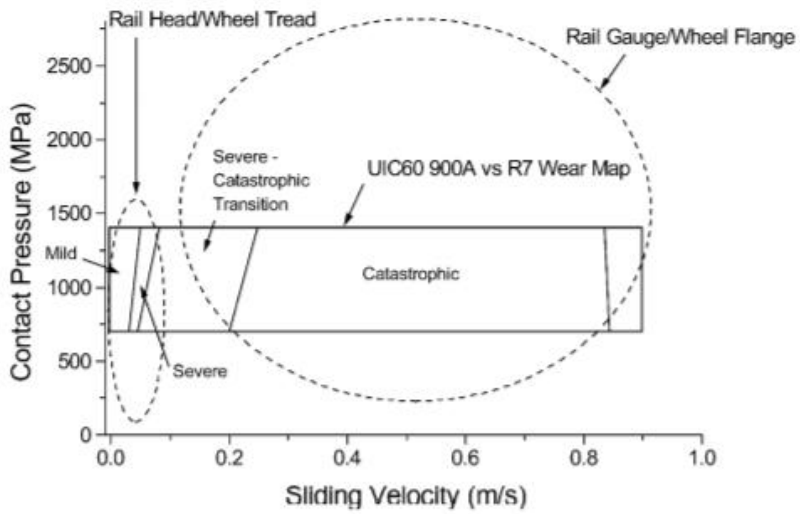

Figure 53: Wear regime vs contact pressure and sliding velocity (Lewis *et al.*, 2010)

The contact pressure along with the speed varies when the contact position moves from the top of the rail to the gauge corner. As stated earlier, head checks arise due to the high friction between the wheel and the rail in the absence of lubrication or friction modifiers along with cyclic loading. However, due to high creep at the gauge corner along with the high contact pressure as a result of the small contact area, as shown in Figure 1, it is evident that catastrophic wear occurs. This takes place at a high rate thereby removing any layer containing head checks that have developed at the gauge corner of the rail. The catastrophic wear accounts for the significant change that occurs over time at the gauge corner as shown in Figure 54.

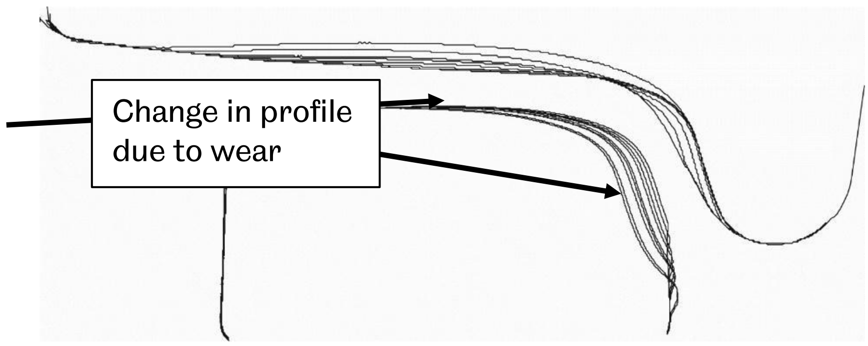

Figure 54: Wear of wheel and rail over time (Olofsson *et al.*, 2013)

3.6 Fatigue crack growth, fracture and testing

Fatigue crack propagation is the next step towards fracture after crack initiation because of fatigue or the formation of wear particles at the interface. The fatigue crack propagation test is similar in fashion to the fracture toughness test in terms of samples and machines used to conduct the test. However, this is where the similarities end. For a fatigue crack growth test (FCG); a pre-crack is introduced into the test specimen by cyclic loading thereby mimicking the exact way the crack forms in an engineering component or in this case at the wheel or rail material. The load is increased at specific crack length interval while the test is being carried out.

The crack grows as a result of the applied load until the amount of material left is no longer enough to sustain the load thereby leading to failure. When the load is applied, there is stress intensity at the crack tip *K*. This can be calculated by the following equation:

$K = FS\sqrt{\pi a}$ Equation 9

Where *S* is the load, *F* is a geometry function of the crack and a is the crack length. At the point of failure, the stress intensity exceeds the material fracture toughness. This results in a material that would typically behave in a ductile manner to fail in a brittle way and that is without any ductility or warning. This typically occurs at loads which are substantially less that the yield or the UTS of the material.

ASTM E647 is the international specification that has been written to be able to perform the fatigue crack propagation test. There are three modes of fatigue crack propagation and the associated stress intensity for the modes are K_i, K_{ii} and K_{iii}. Figure 55 shows the manner in which the various modes occur (Jenkins, 2018).

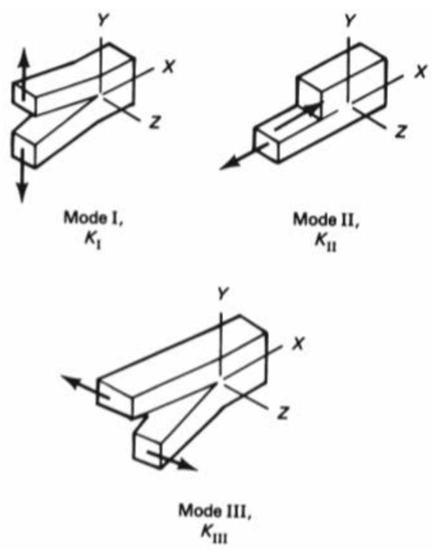

Figure 55: Crack opening modes (Jenkins, 2018)

There are four types of test specimen that can be used for performing this test (ASTM committee E08, 2019); they are:

- Compact tension specimen C(T)
- Eccentrically loaded single edge crack extension specimen ESE(T)

- Arc loading specimen
- Middle tension specimen

The value of *F* from Equation 9 varies for each of these specimens. However, the C(T) specimen is of particular interest due to the small amount of material needed for its production and as such will be the focal point.

F can be calculated using the following equation (ASTM, 1999):

$$\frac{\left(2+\frac{a}{W}\right)\left[0.886+4.64\left(\frac{a}{W}\right)-13.32\left(\frac{a}{W}\right)^{2}+14.72\left(\frac{a}{W}\right)^{3}-5.6\left(\frac{a}{W}\right)^{4}\right]}{\left(1-\frac{a}{W}\right)^{\frac{3}{2}}} \qquad \text{Equation 10}$$

Where *a* is the crack length from the centre of the hole in the FCG specimen and *W* is the distance from the centre of the hole to the end face of the specimen. Figure 56 is a drawing of a FCG specimen indicating dimensions for *a* and *W*.

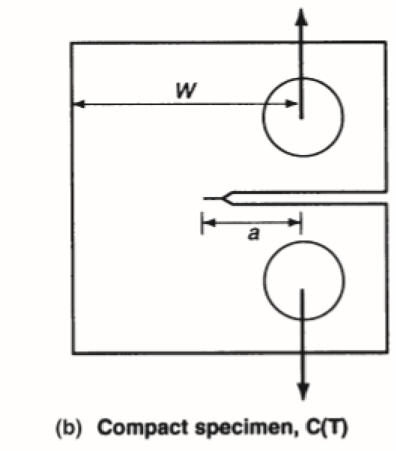

Figure 56: Compact FCG specimen (Kuhn and Medlin, 2018)

Due to the inevitability for cracks to form at the wheel and rail interface as a result of fatigue as stated earlier, Mode 1 is what is assumed to occur at the rail wheel interface and will therefore be the focus of this research.

From Equation 9, it is apparent there is a direct relationship between crack size “a” *a*nd stress intensity factor *K*. Therefore, large inclusions represent large cracks and hence large *K* values. Whilst the load is the driving force in crack initiation, the driving force in fatigue crack propagation is the fluctuation of the stress intensity factor in a cycle.

$$\Delta K = K_{max} - K_{min} \qquad \text{Equation 11}$$

Plotting the difference in stress intensity Δ*K* against the fatigue crack growth rate leads to the graph shown in Figure 57 (Becker, 2018).

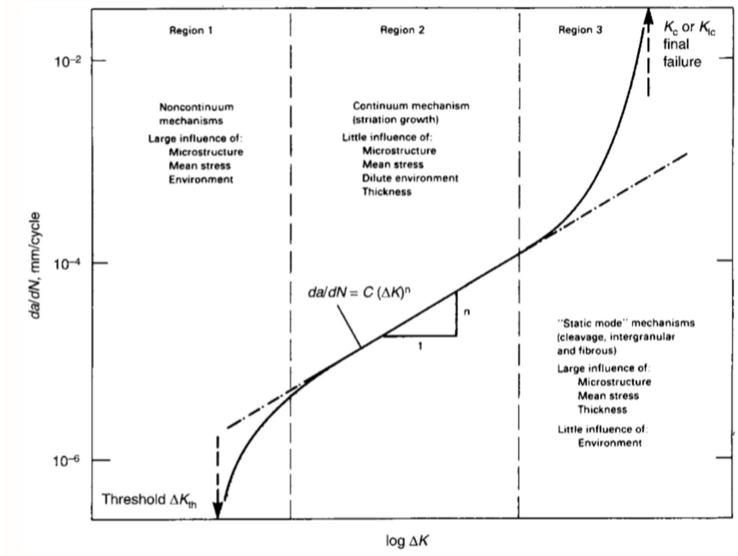

Figure 57: FCG graph da/dn versus Δ*K* (Becker, 2018)

The middle of the graph in Figure 57 is explained by the Paris equation:

$$\frac{da}{dn} = C\Delta K^m \quad \text{Equation 12}$$

Where *C* and *m* are material constants. Various figures have been reported for *C* and *m* which suggests the possibility of been influence by material chemistry and processing parameters. This is in particular when inclusions like sulphides are present. During crack propagation, there is a zone around the crack tip where deformation necessary for the growth of the crack occurs. This is called the cyclic plastic zone and is shown in Figure 58.

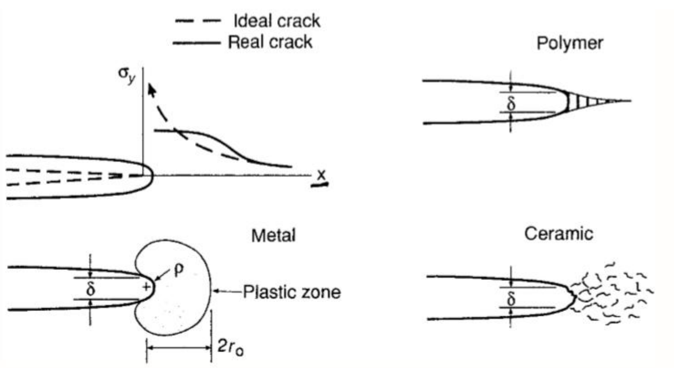

Figure 58: Crack tip behaviour (Dowling *et al.* 2013)

The size of the zone around the crack tip where plastic deformation occurs to allow for crack growth can be calculated using the equation below where *Ry* is the size of the plastic zone around the crack tip.

$$R_y = \frac{1}{2\pi}\left(\frac{K}{\sigma_{ys}}\right)^2 \quad \text{Equation 13}$$

Where *K* is the fracture toughness of the material and $\sigma_{ys}$is the yield strength of the material

The processes dictating fatigue crack growth rate in materials can be categorised into the following (Becker, 2018):

- Ductile striation
- Crystallographic (crack growth on a specific crystallographic plane)
- Cyclic brittle cleavage
- Cyclic micro-void processes
- Cyclic inter-granular processes

These are defined in more detail below:

Ductile striation – As the name implies, it occurs mainly in ductile material and the growth is distinctively noted with striation marks on the fracture face. This is due to the movement of dislocation carrying out the strain due to the applied stress. The striations can be seen on the fracture surface of the specimen or the engineering component. One striation can be linked to a cycle and as such it can be used to tell the number of cycles that occurred before failure finally happened.

Crystallographic – This is when the cracks grow in the preferred plane. Cracks are propagated by the movement of dislocation, so it is when the dislocations interact on the crystallographic level.

Cyclic brittle cleavage – This is a brittle type of crack growth and tends to be associated with dual phase material. The dislocation propagating the crack travels through the grains causing the cleavage.

Cyclic micro void process – This is associated with ductile material and occurs when the dislocations interact with the particles present in the matrix. The inter-particle spacing plays a crucial role here as it determines the ease at which the voids which form as each particle coalescence which in turn drives the crack.

Cyclic inter-granular processes – as the name suggests, occur when the crack travels inter-granularly. This can happen when the cyclic plastic zone is smaller than the grain size of the material. Figure 59 shows a dislocation interacting at a grain boundary to form inter-granular fracture.

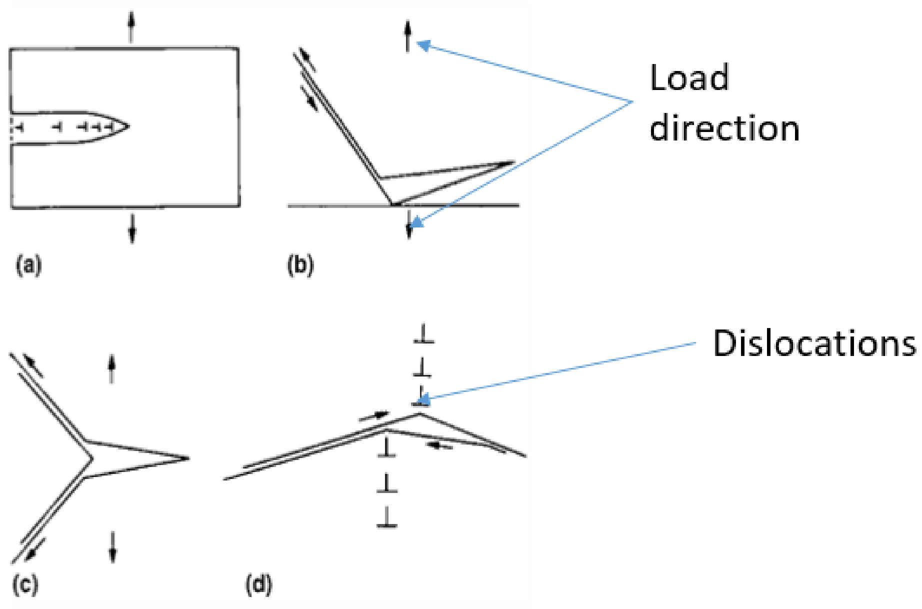

Figure 59: Dislocation interaction at grain boundary (Becker *et al.*, 2018)

The fatigue crack propagation rate is the crucial property to be studied in this research and as a result, factors affecting it need to be understood. Factors which can affect the fatigue crack propagation rate are:

- Microstructure – grain size and inclusions
- Notch orientation (inherent anisotropy)
- Test temperature
- "R" Value

However, this research will be focused on the microstructure and not orientation in the deformed layer

3.6.1.1 Microstructure

As shown in Figure 58, the microstructure has a significant influence on the fatigue crack propagation rate. High strength materials have a higher fatigue crack propagation rate. This is due to the grain size which contributes to their strength becoming detrimental in this case. A small grain size can become smaller than the cyclic plastic zone thereby leading to inter-granular `propagation of the crack.

The constant "C" and "m" are reported as follows for the following type of steels (Barsom and Rolfe, 1999) (mm/cycle):

$0.66x10^{-8}(\Delta K)^{2.55}$ for martensitic steels Equation 14

$3.6\ x\ 10^{-10}(\Delta K)^3$ for ferrite and pearlitic steels Equation 15

These figures were generated in unstrained conditions. It is very possible that the exponent "m" and "C" could change due to the severe plastic deformation. This could account for the very high FCG rate observed (Leitner, Hohenwarter and Pippan, 2019).

The presence of inclusions or particles within the microstructure influence the whole fatigue crack propagation process as well which could lead to a ductile material behaving in a brittle manner and lead to an anisotropic behaviour within the material which is shown through the notch orientation which will be discussed later. The effect of the presence of inclusion on the crack propagation cycle can be seen from the Figure 60 (Agarwal *et al.*, 2014).

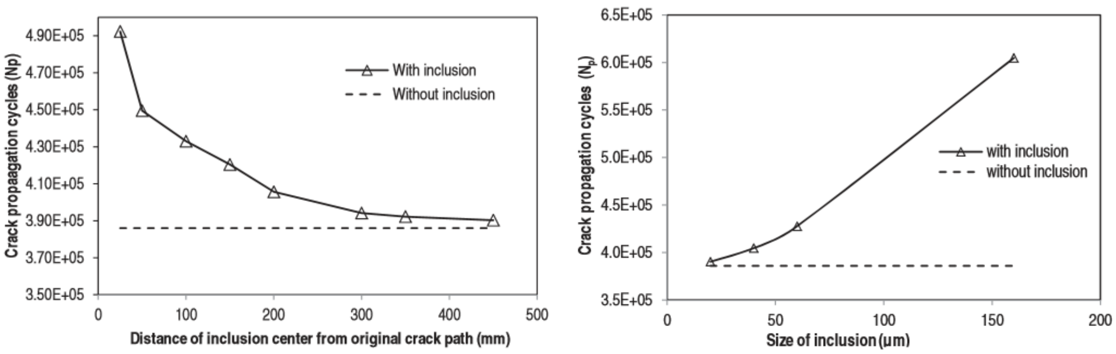

Figure 60: Effects of inclusions on fatigue crack growth (Agarwal *et al.*, 2014)

This is in particular for inclusions like sulphide which tend to be elongated in the deformation direction. As a result of this, the crack growth rate is faster in the deformation direction due to the sulphide stringers. This effect can be reduced by modifying the sulphides into globular particles which reduces this anisotropic behaviour to a degree. Ideally, very low sulphur levels are recommended as this will reduce the volume fraction of the sulphides and in turn the crack accelerating particles. As well as the inclusions affecting the propagation rate, they can also increase the $\Delta K_{threshold}$. This is the point at which there is very little or no crack growth and has been indicated to be between a value for a of 10^{-9} and 10^{-10} or less. Apart from this, the inclusions or particles serve no benefit.

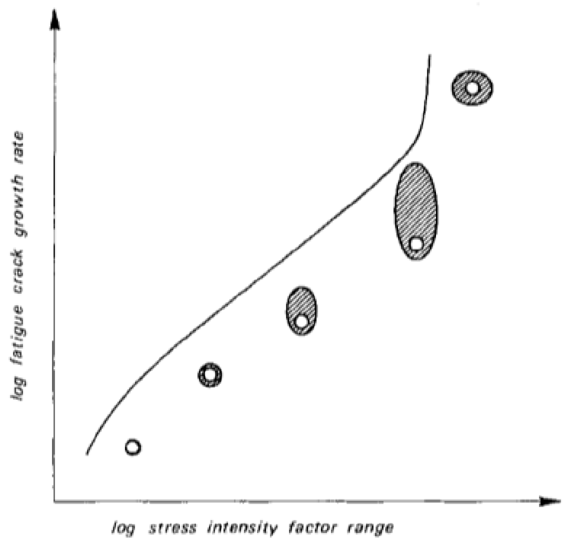

Figure 61: Void growth during FCG process (Barbangelo, 1985)

Figure 61 shows the formation of voids around an inclusion which is typically expected in a ductile material during the crack propagation process. This mechanism increases the rate at which a void coalesces, which is one of the fatigue crack growth processes that can take place. Failure leads to formation of a dull surface because of the void formations at the inclusion sites because of the fracture toughness being exceeded due to the applied stress.

In the severe plastic deformed material, there is an increase in dislocation density within the material after undergoing an increase in strain from Figures 62 and 63. This leads to a grain refinement and accounts for the small grain size. However, given the inherent anisotropic behaviour within the material due to sulphides, the increase in dislocation in the original deformation direction can lead to a crack tip that is associated with a brittle material.

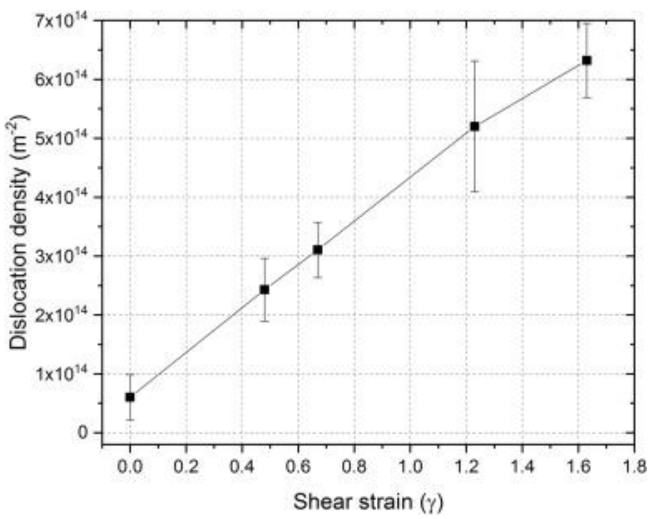

Figure 62: Effects of strain and dislocation density (Nikas *et al.*, 2018)

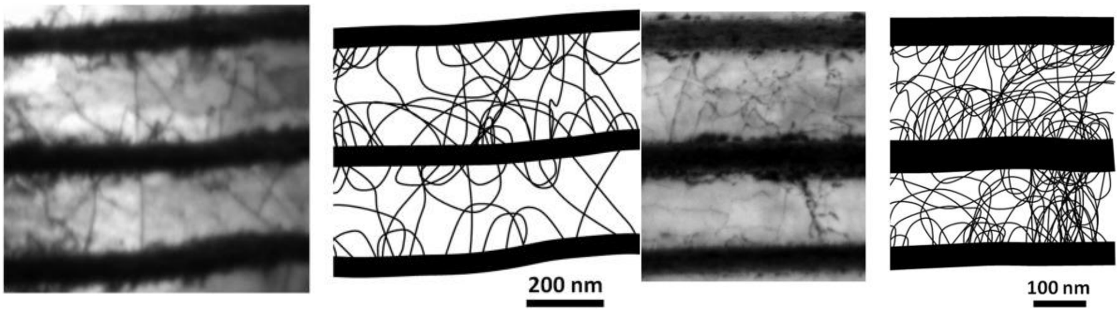

Figure 63: Effects of strain on microstructure (Nikas *et al.*, 2018)

As stated earlier, the ΔK threshold can be affected by particles present within the materials. It is also affected by the type of crack closure mechanism. There are four types of crack closure that can occur within the material as shown in Figure 64 (Barsom and Rolfe, 1999).

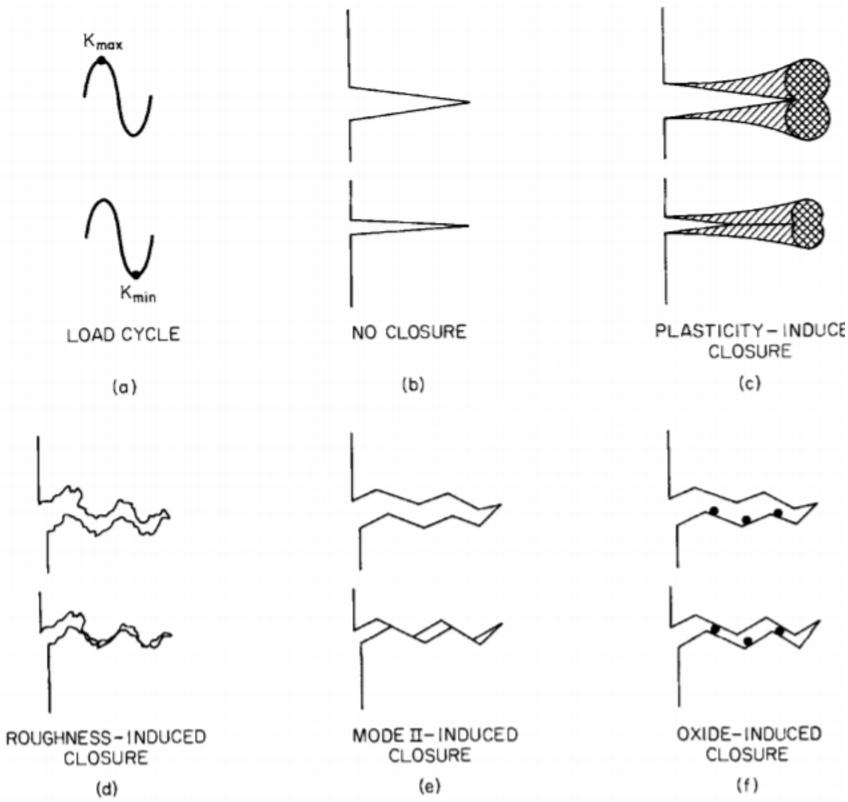

Figure 64: Crack closure mechanisms (Barsom and Rolfe, 1999)

The plasticity induced closure is most prominent in all materials and is to be expected in this research. This is where the intrinsic nature of the material itself resists the crack propagation.

Roughness induced closures are associated with the asperities on the crack face of the specimen. This type of closure is prominent in material that exhibit brittle behaviour

Mode 2 induced closure can occur where there is a mixture of grains in the path in which the crack is travelling.

Oxide induced closure involves oxides present within the crack. This kind of behaviour is when an oxidising environment is present which drives the formation of oxides.

These crack closure mechanisms are not restricted to just affecting the $\Delta K_{threshold}$, but can also affect other parts of the of the FCG behaviour. This is the case for plasticity induced closure which has an impact on higher ΔK values

3.6.1.2 Notch orientation

Another factor that can affect the fatigue crack propagation is the direction in which the cracks are traveling relative to the microstructure. The orientation effect especially at the wheel-rail interface can be put down to the orientation of inclusions present especially manganese sulphide as shown in Figure 65. The volume fraction increases with increasing levels of Sulphur and as a result there are more sites for crack propagation.

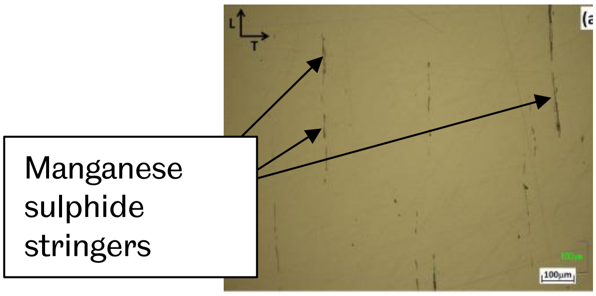

Figure 65: Manganese sulphide stringer (Maya-Johnson *et al.*, 2015)

Previous literature has shown severe anisotropy affects the fatigue crack growth rate (Leitner *et al.*, 2019). This is especially important when the principal shear direction is considered.

Dislocation piles up at the elongated manganese sulphide sites in the shear direction which could lead to formation of micro-cracks which is why the sulphides contribute to the crack length. The crack tip that can arise because of this is shown in Figure 66.

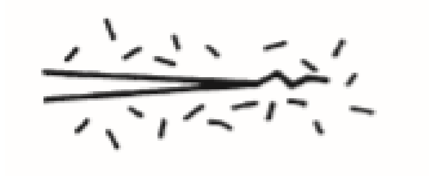

Figure 66: Brittle crack tip in FCG sample (Jenkins, 2018)

Figure 66 shows what the crack tip is expected to look like as a result of the numerous sulphide volume fractions after undergoing severe plastic deformation.

Also it is possible that in previous research (Leitner *et al.*, 2019) that the crack propagation is in the direction of the shear strain which has resulted in the alignment of the grains in the plane and direction. This is shown in Figure 30a. Crack propagation across the structure will be going between the grains boundaries thus resulting in a brittle type of appearance as well as a high fatigue crack propagation rate.

3.7 Wheel-rail interface modelling

Modelling has long been used to try and predict material behaviour. It involves the application or development of mathematical equations to help in predicting wear or crack initiation or growth at the interface as a result of the formation of the deformed layer. It tends to involve trying to predict the behaviour in two dimensions first, as it is easier when compared to a three-dimensional approach. The first attempt at trying to model wear was the Archard model; after which other modelling approaches were developed which include the brick model, wedge model and finite element analysis of the contact area, to mention a few. Whilst some of these approaches can use existing data like Poisson's ratio and Young's modulus as the case is for finite element analysis; others like the wedge model require experiments to be conducted in order to generate constants for the equations used due to their approach. The main focus of this review was not modelling, however, some of the modelling approaches will be discussed in brief as it is important to know how they work when planning experiments for entering inputs and validation.

3.7.1 Archard wear modelling

Before the emergence of the latest models like the wedge model and finite element approach, the Archard model was the first to try and predict the material behaviour because of a sliding contact which was then applied to wheel-rail interaction.

This uses an empirical wear coefficient to predict the material removal from different parts of the rail or wheel and hence can be used to determine the profile evolution. It is based on the principle that one component is harder than that other which leads to abrasive or adhesive wear and involves the use of the Archard equation.

Although it was a good attempt at the time, it was only based on the interaction between the asperities of both component and does not consider the plasticity that results from the rolling and sliding contact which creates the deformed layer as well as contributes to wear debris formation. It was also based on data generated in the laboratory using a pin-on-disc approach. This does not consider other factors like contact area or real-life conditions like leaves on track or environmental condition which can affect the traction and therefore give different set of results. As a result of this, this makes this model no longer suitable today. Especially since it is intended that the planned model is to be used to generate real life conditions.

3.7.2 T-gamma modelling

This is a modification to the Archard model. It implies the frictional energy is proportional to the material loss as a result of wear and tries to quantify the loss within the contact area which is something the Archard model does not do. It links the volume of material lost to the traction energy divided by the contact area. It can be used to account for the material loss even when there is a change in surface condition due to leaves, water or the presence of friction modifiers. This model is based on data generated from laboratory experiments using the twin disc approach and not true scale test rigs. Figure 67 shows the graph generated using the T-gamma approach from a series of twin disc experiments at different conditions. It shows the prominent wear mechanism in play at the various stages. This model is a macro approach. The effects of the deformed layer are accounted for based on the volume of material lost.

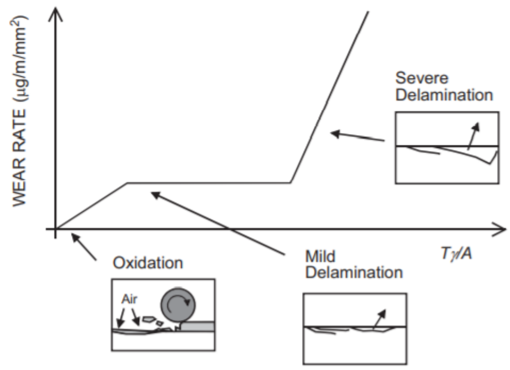

Figure 67: T-gamma model schematic (Lewis *et al.*, 2010)

3.7.3 Finite element modelling

Finite element analysis has been used for crack growth analysis, but it has been acknowledged that it can be a difficult process. It involves dividing the component into elements with each element following a set of rules or equations, this is called a mesh when this is done. Due to the nature of wear and crack initiation, the elements in the mesh need to break down to show when the material has undergone plasticity and as result renders the model ineffective. Properties of the material are assigned to the individual elements alongside equation which consider the amount of strain the material is undergoing or in the case of fatigue crack propagation, it will be an equation which calculates the stress intensity that the material is experiencing because of the crack growth. Complete failure of the element occurs when the stress intensity exceeds the fracture toughness thereby leading to formation of debris.

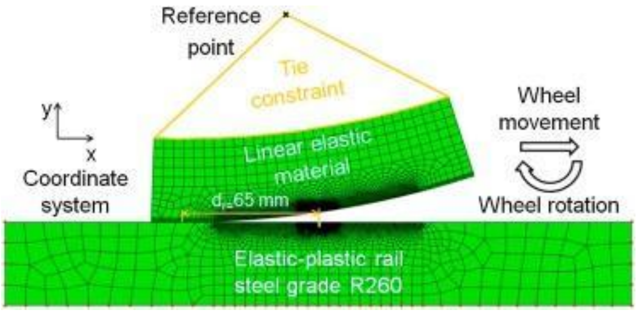

Figure 68: FEM analysis of wheel rail interface (Daves *et al.*, 2019)

When this occurs, the model has to be re-meshed, and the program run again which is the problem as the whole model will no longer be representative of the wheel-rail interface as in reality the material is not renewed and any new surface exposed as a result of wear or material breaking off is already been plastically deformed to a degree and the profile is no longer the same. To increase the accuracy of the model, an increase in the number of elements is required as shown in Figure 68 as well as a lot of computational work which is time consuming. The FEM approach can be used for both two- and three-dimensional modelling. This model does not consider the real-life change in profile that occurs due to wear and plasticity and as a result is not ideal.

3.7.4 Brick modelling

The brick model was developed in recent years and is a 2D model. It involves using small rectangles to represent the material with the yield stress and shear strain of the material assigned to each brick and as a result shares this similarity with the finite element analysis approach. However, this is where the similarity ends as it only looks like the finite element, but it is far from it. During the simulation, the bricks accumulate strain because of the repetitive loading. This is shown in Figure 69 (Asih *et al.*, 2012).

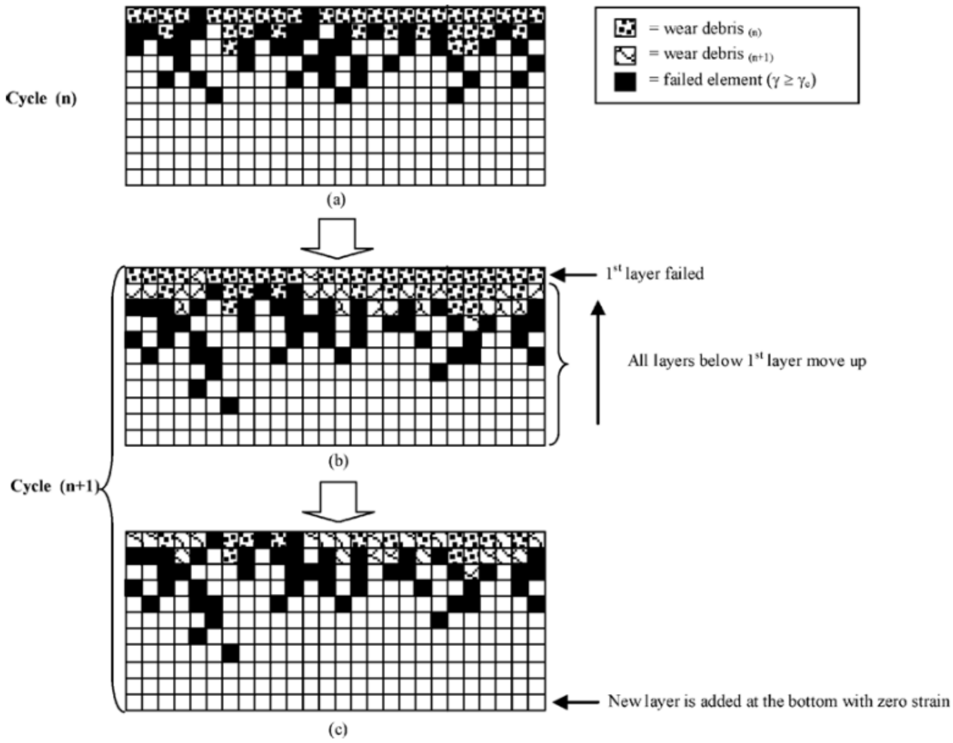

Figure 69: Brick model of contact layer (Asih *et al.*, 2012)

Other factors that affect the strain can also be simulated by this model. The dark bricks represent failed elements of the model and can be regarded as cracks or debris due to the plasticity the material is undergoing as a result it can be difficult to distinguish when a crack is propagating due to rolling contact fatigue to form wear debris. When an entire layer is dark then the next layer below becomes the new surface. This new surface layer has already had some degree of plasticity from the previous loading processing. This is something that cannot be done in the finite element analysis approach without re-meshing and more computational work. The brick model can be used to indicate to a degree the overall profile of the contact surfaces after several passes due to the loss of surface as shown by the dark or compressed bricks. This model is acceptable to help quantify the strain at the interface, however, still falls short due to it being 2D. It also does not show how cracks propagate but rather gives an indication of how wear debris can be formed and assumes the absence of inclusions which can be the case depending on the steel making process.

3.7.5 Wedge modelling

The wedge model is another recently developed approach and is a two-dimensional model. This is an approach developed which involves the mathematical interaction of the various strain factors in effect at the surface of the material and assumes a crack initiation layer is the location where this interaction takes place (Trummer, Marte, Scheriau, *et al.*, 2016). The assumption of the crack initiation layer is based on the formation of the deformed layer created at the interface. The crack initiation layer mirrors the deformed layer at the interface. The model allows for the prediction of a wear particle or ratcheting leading to a rolling contact fatigue crack depending on interactions at the deformed layer as well as the isotropy of the layer.

The model incorporates the other modelling equations developed historically to aid in its prediction of the formation of a crack within the deformed layer. This includes a standard approach to predicting the fatigue life, the contact model approach as well as the model developed by Krause and poll to predict the change in profile because of wear and plastic deformation. This model utilises constants which are derived from full-scale experiments and is used in the calculation.

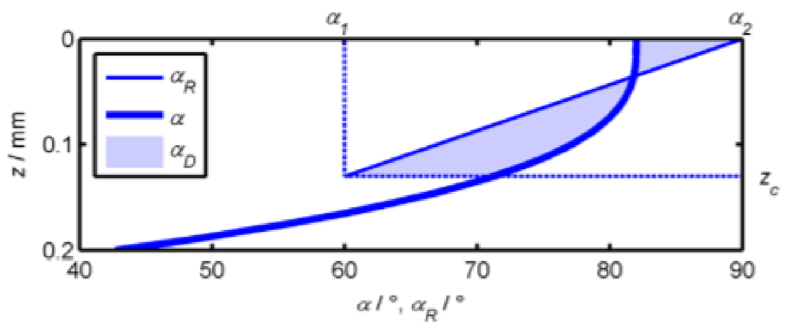

Figure 70: Layout of wedge model (Trummer, *et al.*, 2016)

The parameters α_1, α_2 (angular plastic shear strain limits) and z_c (crack initiation layer) from Figure 70 are derived from experiments which are then used to derive the similarity parameters which dictate if a fatigue crack or a wear particle will be formed depending on the factors in play. The crack initiation level in the models refers to the deformation layer that arises because of the wheel-rail interaction. Due to the utilisation of a full-scale rig; this puts it in good stead to be applied in real world situation as it accounts for contact patch which is not accounted for in some of the other models. This model does not consider the fatigue crack propagation through the material. This model again assumes the absence of inclusions which is possible and depends on the steel production route, however, it is still a good model and puts it in better stead compared to the others.

3.8 Deformed layer analysis

The fatigue crack propagation (FCG) in the deformed layer in wheel and rail materials is not fully understood as it appears to have consistently displayed anisotropic behaviour when studied. Previous work presented specimens with severely deflected crack paths and very high crack growth rate depending on orientation (Leitner, 2017). This could be due to the grain size and orientation, as shown in Figure 29b.

The microstructures can be assessed by polishing the sample to a smooth finish and viewing under an optical microscope before etching and viewing under the scanning electron microscope. Etching is done with Nital and is needed to distinguish the ferrite and carbide phase in pearlitic or bainitic rail. The percentage of Nital in solution can vary between 2-3%. However, care has to be taken in order avoid over etching as this can make viewing under the optical microscope difficult. Due to the depth of field, the microstructure and fracture face will have to be viewed under the electron microscope.

Micro hardness measurements have been conducted on the deformed layer in the past revealing the hardness profile which starts off very high at the surface of the wheel and rail material and drops sharply (Larijani *et al.*, 2014). This reflects the change in microstructure associated with the plasticity during the process. The measurements are typical done using Vickers indentation. This is carried out with a pyramid shape tip. A load is applied to the diamond tip and an indentation is created. The geometry of the indentation reflects the hardness of the material.

3.8.1 Microscopy

An optical microscope utilises a series of lenses which help to magnify the images and can go as high as 500x magnification. In the case of an electron microscope, it utilises electrons accelerated through a chamber where a large potential difference is set-up. The electron is generated using either an electron gun, tungsten carbide filament or Lanthanum Hexaboride (LaB_6). The whole set-up is enclosed within a vacuum chamber. Magnification is increased by increasing the potential difference accelerating more electrons. Electrons are utilised as they have a smaller wavelength than light and therefore give a better resolution.

There are two types of electron microscope; namely the scanning electron microscope and the transmission electron microscope, however, the scanning electron microscope is what was most likely to be used in this research as it is sufficient for generating the information needed like analysis of inclusions if there are any and examination of fracture surface and the associating microstructure. The transmission electron microscope is suitable for viewing the crystal structure of the material. Figure 71 shows the volume of the electron interaction as well as the associated resulting wavelength generated due to the primary electron interacting with the intended sample. The electron beam allows information to be generated from the sample even below the surface up to a depth of 2.5 microns.

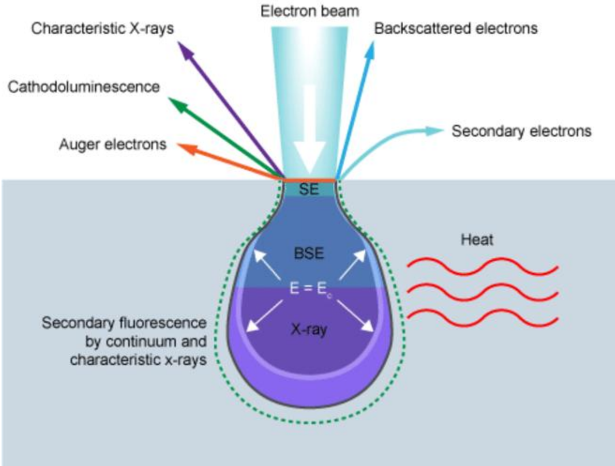

Figure 71: Electron volume interaction characteristics (Pletincx, 2014)

Unlike an optical microscope, there is no need for an optical lens, but rather electro-magnetic lenses are used to help with focusing the electron on the sample.

When the electron interacts with the sample, it interacts with the atoms. The microscope has special detectors which allow it to collect data based on the reflected electrons as well as the secondary electrons generated because of the interaction from the first electron. X-rays are also generated due to the excited electrons returning to their ground state. This allows the electron microscope to perform chemical analysis of phases present within the sample. This is called energy dispersive X-ray (EDX) analysis.

The transmission electron microscope has a similar set-up to the scanning electron microscope with the following exceptions. The electrons are accelerated through the samples. This leads to the ability to reveal more details of the sample like the crystal structure and dislocations. For the electrons to go through the sample; it must be thin and as a result special preparation techniques are involved like electron beam polishing. The sample itself is 4 mm in diameter and placed on a specialised sample holder that goes into the chamber of the transmission electron microscope.

It is worth noting that the sample must be able to conduct electrons to gain the information mentioned above. If this is not possible, then electrons accumulate on the surface of the sample and leads to a process called electron charging. To avoid this, a conductive layer of graphite can be applied to the sample to allow for the current to flow through. Gold can also be applied to help with the conduction of the electrons.

Atomic force microscopy is another microscopic technique that can review the topography of the wear debris or the resulting fracture surface which can become the new running surface. The atomic force microscope gives a better accuracy of the asperities associated with the sample involved. This contains a probe made from silicon nitride. It works by using a probe to track the surface of the material. It is connected to a piezo electric device which then generates an electric signal which is used to monitor the surface. Figure 72 shows a schematic layout of an atomic force microscope.

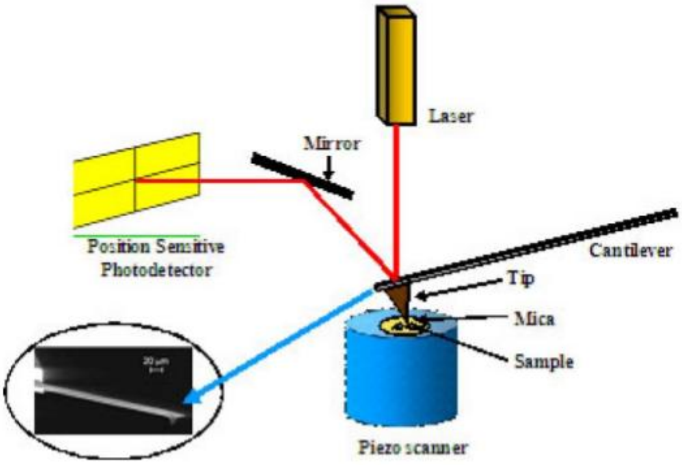

Figure 72: Schematic of atomic force microscope (Chatterjee *et al.*, 2010)

To review the internal microstructure of the material without destroying it, X-rays are needed again. X-rays are already used to view internal defects in casting. A Fluorescent pad is placed on the other side of the casting and then the casting is bombarded with X-rays. As stated earlier in the electron microscope description, X-rays are generated because of electrons returning to their ground state after been excited to a high energy level. The X-rays have a very small wavelength which is why they can travel through objects and reveal details within. Particle like inclusions or carbides absorb the X-rays and appear as dark patches on the fluorescent pad. Cracks are also visible due to the distinction between the matrix in terms of how the x-rays interact with the surfaces. Whilst this is a basic description of the x-ray machine; the type that could be used for this investigation is the 3D X-ray tomography machine. This can provide useful information on the integrity of the material after processing.

3.9 Summary

The high pressure torsion test will be used as it is the available severe plastic deformation technique for this experiment in addition to that fact that it is very capable of creating the plasticity undergone by the wheel and rail material at the strain levels intended to be investigated. The strain at which the FCG test has been done thus far do not accurately represent the same level of strain the materials experience at the wheel-rail interface. The microstructure will also be investigated to find out what role it plays in the fatigue crack propagation rate of the material after it has undergone the severe plastic deformation especially when anisotropy is considered which was displayed in previous research (Leitner, Hohenwarter and Pippan, 2019). Given the small sample that can be made from the HPT process, new fixtures would be needed to hold the FCG sample that would be manufacture from them.

The scanning electron microscope will be needed to review the fracture surface of the cracked FCG specimen as well as the microstructure of the steels due to the interaction with the crack and the microstructure. Any inclusions present will also be identified during the SEM examination.

Optical microscopy will also be needed to assess the microstructure after etching the material in Nital as well as carry out initial assessment of inclusions present.

4 HIGH PRESSURE TORSION EXPERIMENTAL DESIGN

4.1 Introduction

The aim of this work was to create a deformed layer similar to that shown in Figure 73 and determine its fatigue crack propagation properties. Of the available severe plastic deformation (SPD) techniques used in investigating the deformed layer which were equal channel angular processing (ECAP) and high pressure torsion processing (HPT), the HPT approach is the most suitable due to its ability to create a sample with very large strain levels. This is something that cannot be achieved with the ECAP processing (Arun Kumar *et al.*, 2019). A fatigue crack growth test (FCG) is then to be conducted from the created deformed layer.

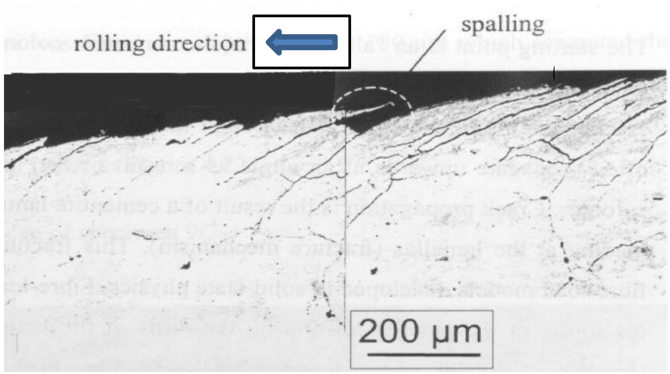

(a)

(b)

Figure 73: Deformed layer in a rail material: (a) un-etched (Kapoor, Fletcher & Franklin, 2003); (b) etched

The whole process involved first identifying the specimen dimensions than could be processed within the HPT rig specification, then designing the HPT anvils. The FCG specimens were also derived from the HPT disc and then grips were designed which could hold it followed by the way crack monitoring was done and then calculations on how the testing was conducted to have an indication of how many data points could be gather as well as the duration of the test. All this was done whilst still trying to conform to ASTM E647 as closely as possible. ASTM E647 is the international standard for fatigue crack growth testing. The flow chart in Figure 74 gives an overview of the whole process.

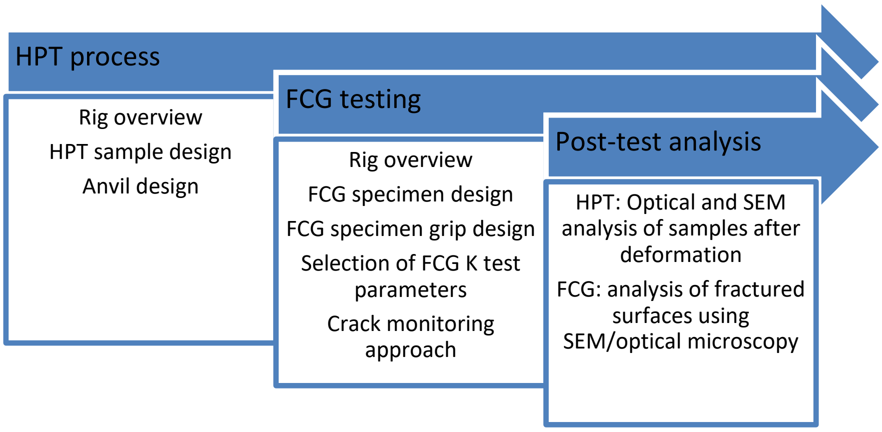

Figure 74: Overview of experimental process

4.2 High pressure torsion test machine

The high pressure torsion approach is a technique for creating a severe plastically deformed layer in a material, as outlined earlier. It involves placing a sample between two anvils and applying pressure and then rotating the anvils whilst maintaining the pressure (see Figure 75). The specimen rotates as the anvils are turned. The rotation of the specimen whilst under pressure needs to be as slow as possible to prevent heat generation within the specimen.

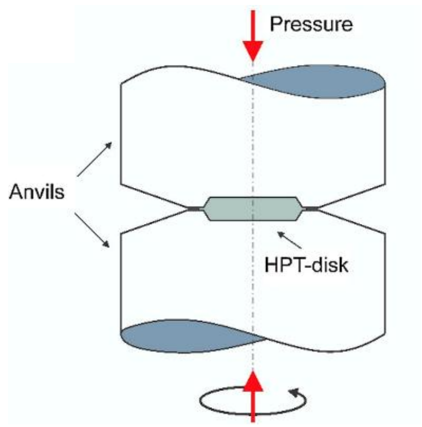

Figure 75: Schematic diagram of HPT rig and HPT disc (Leitner *et al.*, 2019)

However, it would seem the minimum pressure requirement to prevent slipping of the material is linked to the rotation rate as well as the material being processed a shown in Figure 76 (Edalati *et al.*, 2009). The minimum pressure intended for this experiment will be 5GPa at a maximum rotation speed of 1mm per second (Edalati *et al.*, 2009). This is needed to prevent slip occurring during the HPT process.

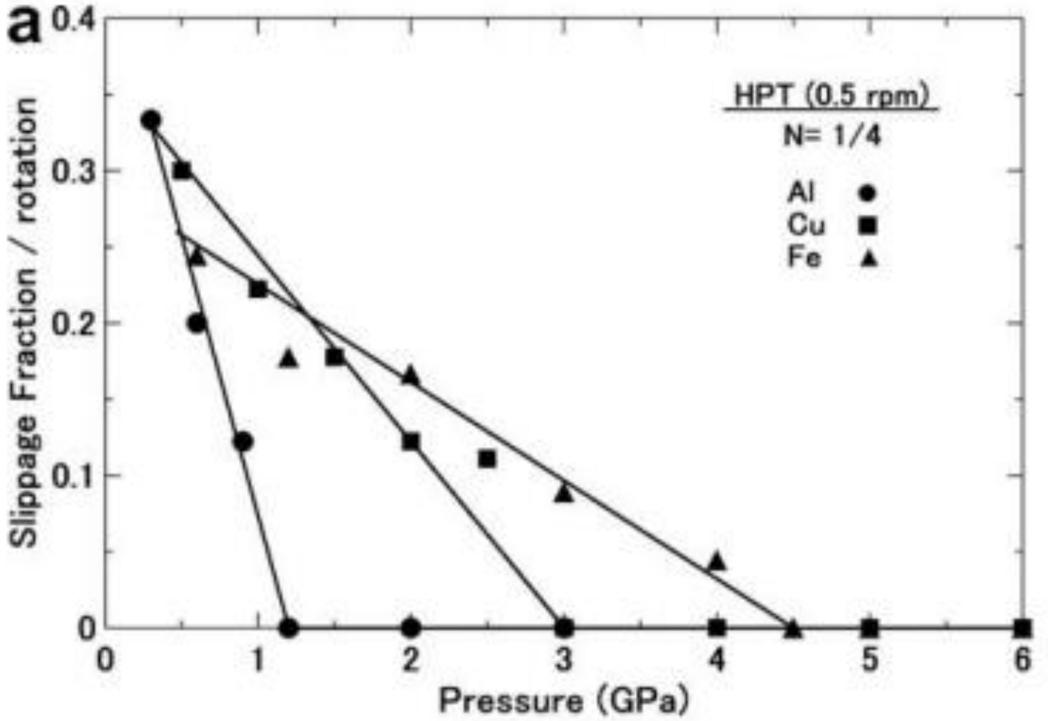

a)

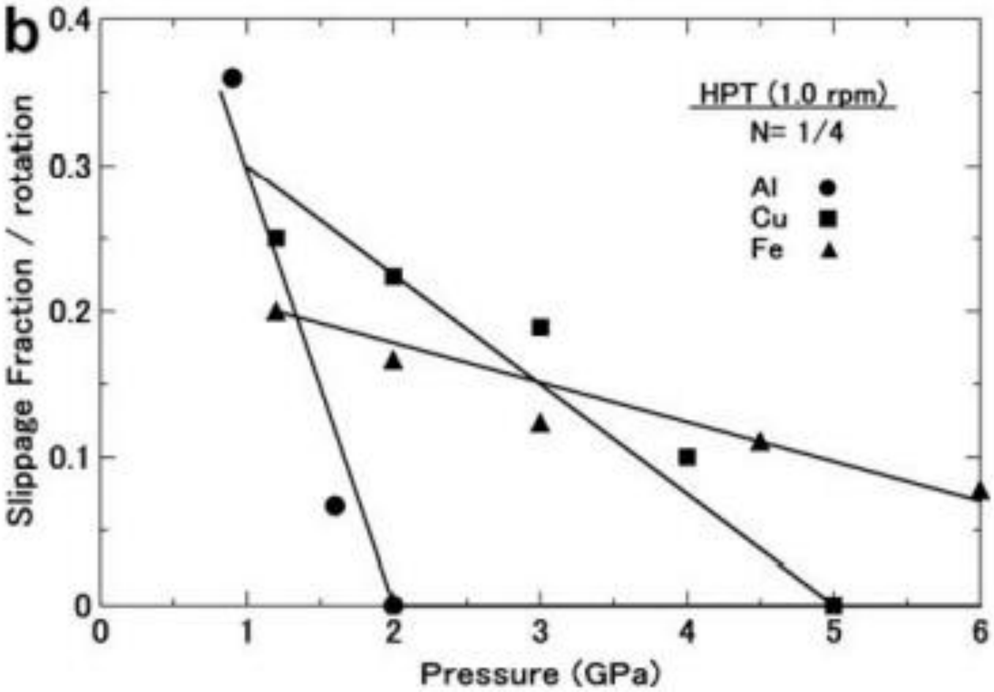

b)

Figure 76: Slippage fraction versus pressure for rotational speeds of: (a) 0.5rpm and (b) 1rpm (Edalati *et al.*, 2009)

The objective of the HPT process is to produce a deformed layer in a specimen with a strain level of at least of 6. This level of strain is approximately the amount of strain typically experienced at the top of a rail, as shown in Figure 77.

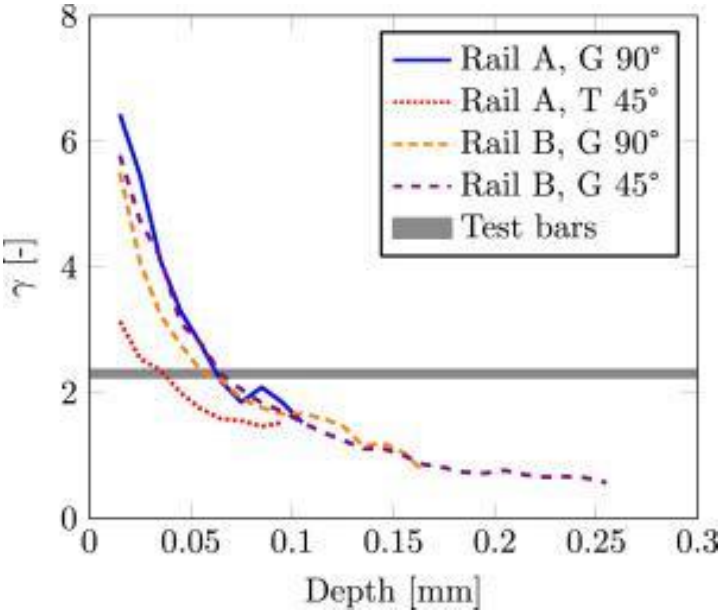

Figure 77: Strain levels in a rail surface (Meyer *et al.*, 2018)

However, in previous work where deformed layers were created with high strain levels, machines with higher limits in terms of torque and force were utilised, as shown in Table 3 (Hohenwarter and Pippan, 2019).

HPT Classification	Max Load (Tonnes)	Max Load (kN)	Max Torque (Nm)	Speed (rpm)
“Small”	40	392.3	500	0.2
“Medium”	400	3922.7	10000	0.07
“Large”	1000	9806.7	130000	0.016

Table 3: HPT test facilities capabilities used in previous studies

These capabilities allowed processing of HPT discs as large as 30mm. This is shown in Table 4.

Study Reference	Pressure (GPa)	Specimen Diameter (mm)	Specimen Thickness (mm)	Thickness/ Diameter ratio
Leitner *et al.* (2019)	5.6	30	7	0.23
Larijani *et al.* (2015)	4	25	8	0.32
Kapp *et al.* (2016)	5	26	5.9	0.23
Scheriau and Pippan (2008)	6	8	0.8	0.1

Table 4: Previous HPT experiments and the processing parameters

The test machine available within The University of Sheffield has reduced capability over the machines outlined in Table 3. The maximum load and torque that can be applied are 400kN and 1000Nm respectively.

This meant that a new HPT disc design was needed. The design was not straight forward as machine capability had to be considered alongside the need to create a deformed layer large enough for specimens for fatigue crack growth experiments to be extracted.

4.2.1 High pressure torsion sample

Before looking at the exact design of the HPT disc, the position that it was machined from in a rail head must be considered. Rail head microstructure is not completely homogenous across the rail head and variation can be greater when the rail is heat treated. The production of the rail involves air cooling the material after rolling. In some cases, this can lead to the formation of a hardness gradient. Figure 78(a) shows approximately where the HPT disc was to be taken from. Figure 78(b) shows a hardness map of an R260 rail head (Christoforou *et al.*, 2018) (Table 5 shows the chemistry of R260 rail material). As can be seen the hardness is consistent in the region where the disc will come from. In fact, in this case the disc could come from anywhere in the rail head. This will not be the case for a heat-treated rail such as R350HT or R400HT.

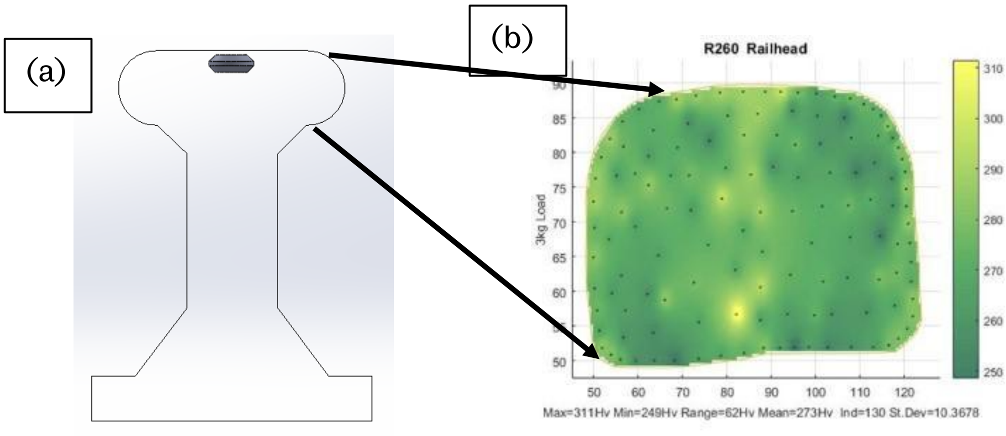

Figure 78: (a) Schematic of HPT disc location in rail head and (b) hardness map of R260 rail head (Christoforou *et al.*, 2018)

	C	Si	Mn	P	S	Cr	Al	V	N
Minimum	0.60	0.13	0.65						
Maximum	0.82	0.60	1.25	0.030	0.030	0.15	0.004	0.030	0.010

Table 5: R260 rail chemistry (BSI Group, 2011)

Cutting the sample was done using the wet cutting technique so as not to alter the hardness and microstructure from frictional heating.

The HPT disc was originally intended to have a thickness to diameter ratio of 0.1 or less (Pippan *et al.*, 2010). However, recent work has shown that it is possible to process samples larger than this, but at the expense of strain inhomogeneity, as shown in Figure 30. The amount of strain dictates the properties the material has as it indicates the amount of work hardening that has taken place. As a result of this there is a variation in properties along the length of the specimen from the bottom to the top with the hardness being one of them.

Due to this strain inhomogeneity, initial HPT samples were to be deformed to see the size of the area in which there is strain homogeneity and ensure the FCG sample was taken from that region of the sample.

Figure 79 shows HPT discs used in previous studies as well as the fatigue crack growth specimens machined from them post-test. The number of specimens obtained, and the type of specimen taken can be seen.

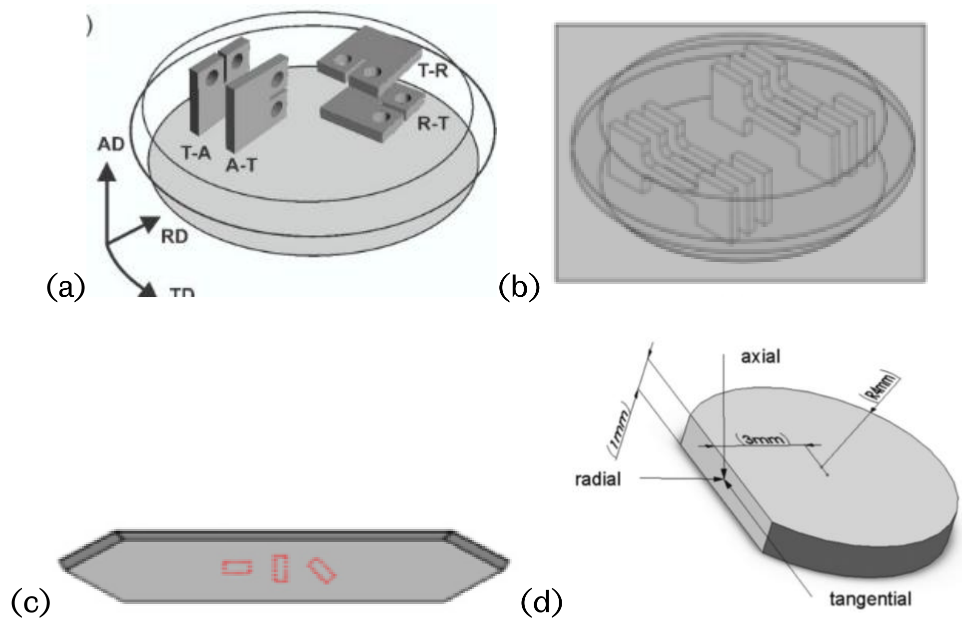

Figure 79: HPT specimens from previous studies and details of the fatigue crack growth specimens: (a) Leitner, Hohenwarter and Pippan (2019); (b) Larijani, Kammerhofer and Ekh (2015); (c) Kapp *et al.* (2016); (d) Scheriau and Pippan (2008)

From Table 3, it was evident that the torque was a major limitation for the test machine in Sheffield, as these levels cannot be reached.

Torque "M" for a given specimen radius can be calculated after making it the subject (Edalati and Horita, 2016):

$$M = \frac{(2\pi r^3)}{3} \qquad \text{Equation 16}$$

The shear stress was read from the graph in Figure 80 which was taken during a high pressure torsion experiment (Scheriau and Pippan, 2008). The graph was created by measuring the von Mises strain in-situ during the deformation process.

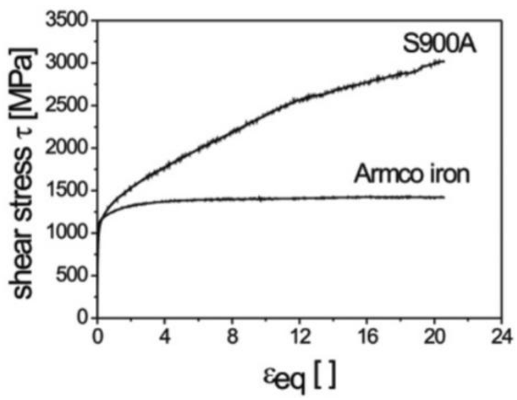

Figure 80: Stress/strain relationship for R260 rail (S900A) (Scheriau and Pippan, 2008)

As well as the shear stress at the radius, *r*, of interest; the shear stress for the radius at the outer circumference was also needed to ensure it conforms to HPT rig capabilities.

If a disc diameter of 30mm and thickness of 8mm was assumed (as indicated in Figure 79(a), the target strain of 6 is at a radius 9.5mm).

Strain for the HPT disc is calculated using the following equation:

$$\gamma = \frac{2\pi r n}{t} \qquad \text{Equation 4}$$

(Repeat from Chapter 3)

Where *r* is the radius, *n* is the number of turns (on the HPT machine), and *t* is the thickness of the specimen prior to deformation.

To achieve a minimum strain of 6 at the radius of 9.5mm the number of rotations *n* is 0.8. This achieves of 5.97 with a thickness of 8mm.

The corresponding strain at the outer radius (15mm) would be 9.43. The von Mises strain is calculated by:

$$\varepsilon = \frac{\gamma}{\sqrt{3}} \qquad \text{Equation 5}$$

(Repeat from Chapter 3)

This is equal to 3.44 at a radius of 9.5mm and 5.44 for a *radius* = 15mm.

The corresponding shear stresses for these strain values were read off the graph in Figure 80. This is 1750MPa at 9.5mm and 2250MPa at *r* = 15mm. Torque at *r* = 9.5mm = 3143Nm (from Equation 16) and torque at *r* = 15mm = 15904Nm. These values are far above the capability of the HPT rig at Sheffield.

The above approach was used again with various specimen dimensions and after trial and error, a diameter of 7.5mm and thickness of 4.4mm showed parameters which were compatible with the HPT rig at Sheffield.

For a disc diameter of 7.5mm and thickness, *t* of 4.4mm, the target radius, *r*, is 3.1mm. The number of turns, *n*, required is 1.36. This gives a strain of 6.02 and a von Mises strain of 3.5. The values at *r* = 3.75mm is 7.29 for the strain and 4.2 for the von Mises strain.

The associated shear stress at *r* = 3.1mm is approximately 1750MPa and 1800MPa at *r* = 3.75mm. The torque amounts to 93.4Nm at 3.10mm and 198.9Nm. These figures are much lower than the rig capability and can be handled given the HPT parameters available for this experiment.

However, to ensure the HPT anvils (see Figure 82) did not come into contact during the process, further adjustments were needed. Figure 81 shows an assumed shape for the disc after deformation during the test process.

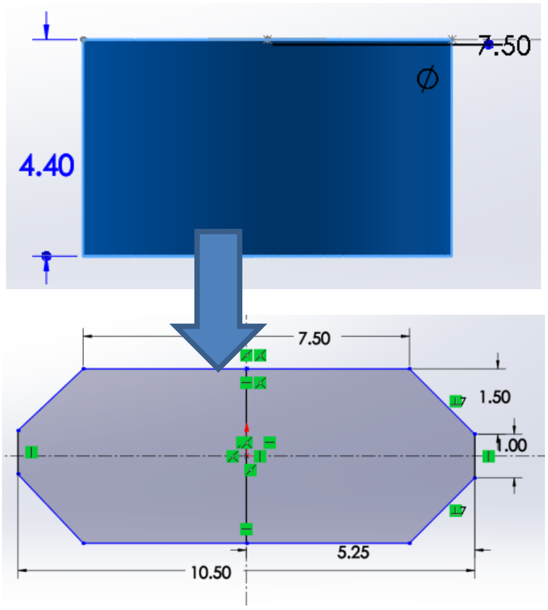

Figure 81: Dimensions of cavity between anvils for a 7.5mm dia. x 4.4mm thick HPT disc before and after deformation (assumed to be filled after deformation process)

To avoid the contact issue of the upper and lower anvil coming into contact, the thickness of the deformed discs needed to be high enough that it kept the anvils apart. The sponsor therefore recommended that the HPT disc be adjusted to be 20% larger than the volume of the disc shown in Figure 81. Figure 82 assumes the shape of the cavity based on an HPT disc with dimensions 7.5mm diameter by 4.4mm thick at the start of the process. The volume was calculated using dimensions from "after deformation" in Figure 81. The taper angle was made to 45° as advised by the sponsor as well. The taper was necessary to help reduce the strain inhomogeneity when the thickness to diameter ratio is greater than 0.1.

The total volume is equal to the sum of the central cylinder added to two times the volume of the "truncated" outer cone.

Volume of cylinder $=\pi r^2 \times h$ Equation 17

Where *r* is 5.25mm and *h* is 1mm.

Volume of Truncated cone = $\frac{1}{3} \times \pi \times h(r^2 + (r \times R) + R^2$ Equation 18

Where *r* is 3.75mm, *h* is 1.5mm and *R* is 5.25mm. The volume was then multiplied by 2 since there are two truncated cones present.

Total volume = 86.50+192.62 = 279mm^3

Therefore, a 20% increase of the starting HPT disc volume is 279×1.2 = 334.8mm^3

The radius was fixed so the height for the new volume had to be derived. Making *h* the subject of the formula for the volume of a cylinder gives:

$h = \frac{Volume}{\pi r^2}$

This makes *h* 7.58mm. Therefore, the dimensions of the HPT disc were 7.5mm diameter and 7.58mm.

The number of turns to achieve the strain of 6 at a radius of 3.1 also had to be recalculated. As a result of this Equation 4 had to be rearranged to make "*n*" the subject. This gives:

$$n = \frac{t\varepsilon}{2\pi r} \qquad \text{Equation 19}$$

This meant that *n* = 2.4 turns. This parameter of *n* = 2.4 now had to be applied to the extreme case where the radius was 5.25 and the thickness, *h*, is 7.58. For this case, the strain was: $\frac{2\times\pi\times5.25\times2.4}{7.58} = 10$ and von Mises strain, $\varepsilon = \frac{10}{\sqrt{3}} = 6$. From Figure 80, the associated shear stress was approximately 2000MPa.

Using Equation 16, the torque came to a value of 606Nm. This is below the maximum 1000Nm, so this was acceptable.

The anvil for the HPT process also had to be designed. The design drew on knowledge gained from the literature review carried out. This was all in a bid to keep the torque requirement as low as possible and ensure there was enough space in the void for material flow to be accommodated. The final design can be seen in Figure 82.

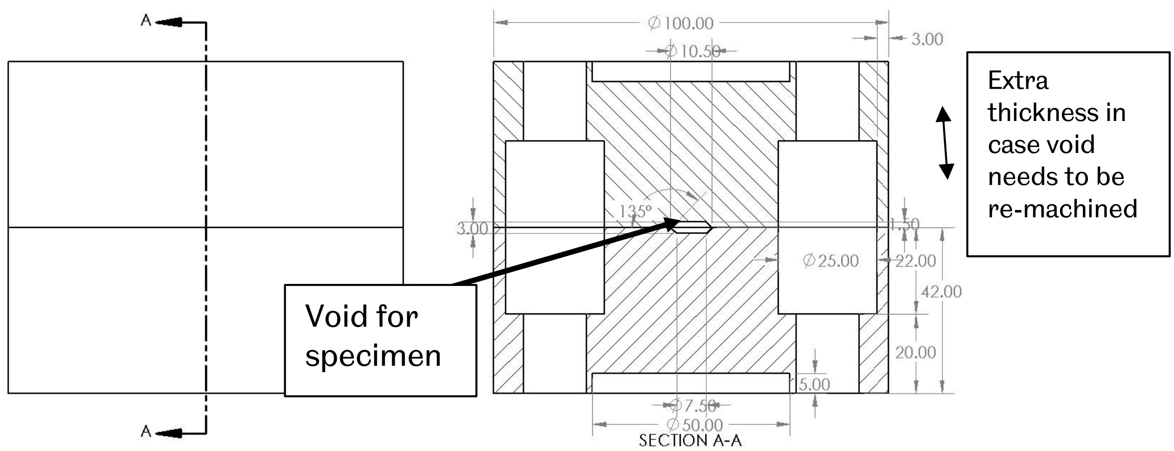

Figure 82: Final anvil design

The anvil was also designed to be 10mm thicker than the nominal requirement. This was to allow for modification to the anvil with minimal downtime if required.

Due to the thickness to diameter ratio being larger than 1/10, there will be inhomogeneity with the sample after testing. The anvil design had to account for this with a larger taper. Previous research had suggested a larger angle would need a lower torque requirement. However, the angle of 45 degrees was selected due to it being similar to what was used in previous research (Hohenwarter and Pippan, 2019).

There were no recommended materials to use for the anvils. However, the conditions were extreme and as a result materials used in the tooling manufacturing sector were considered since they go through similar extreme conditions. As a result of this, ASTM A681 O1 tool steel was selected (see Table 6 for composition). This can achieve a minimum hardness of 59HRc after heat treatment in accordance with the ASTM A681 heat treatment cycle.

UNS Number	C	Mn	P	S	Si	Cr	V	W	Mo
Minimum	0.85	1.0			0.1	0.4		0.4	
Maximum	1.00	1.4	0.030	0.030	0.5	0.7	.30	0.6	

Table 6: ASTM A681 O1 steel chemistry

The chemistry shown in Table 6 achieved a hardness between 212 – 241HB (approximately 22HRc maximum) in the annealed condition thereby making it easy to machine into the desired shape before heat treatment. Figure 83 shows the anvils in position in the HPT machine.

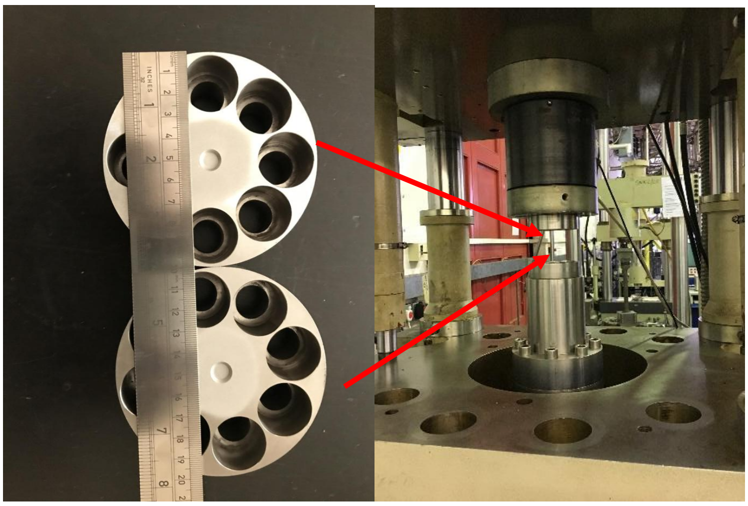

Figure 83: Manufactured HPT shot blasted anvils and their position in the HPT rig

5 HIGH PRESSURE TORSION EXPERIMENTS

5.1 Introduction

The purpose of this chapter is to outline the test approach and parameters to be used for the HPT experiments. Devices to be used are the high pressure torsion device, optical microscope and scanning electron microscope.

5.2 Test approach

5.2.1 Exploratory high pressure torsion experiments

Prior to embarking on the first successful high pressure torsion experiments, there were other attempts to try and create the deformed layer. First at relatively lower pressures of 3.3GPa and 4GPa were trialled for R260 specimens. The rotation speed used was as slow as possible to err on the side of caution. The graphs below in Figure 84 show the torque data generated from both experiments. Full detail of the final test method is presented in a later section

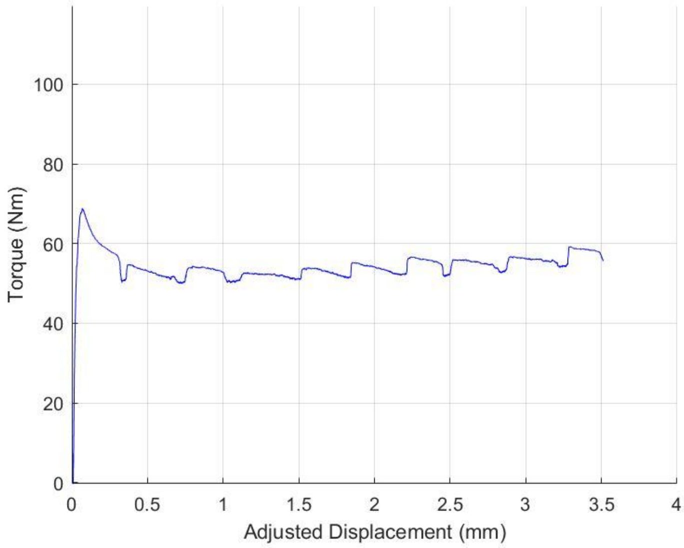

(a)

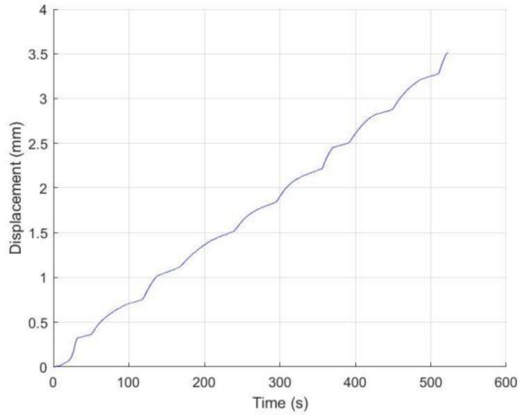

(b)

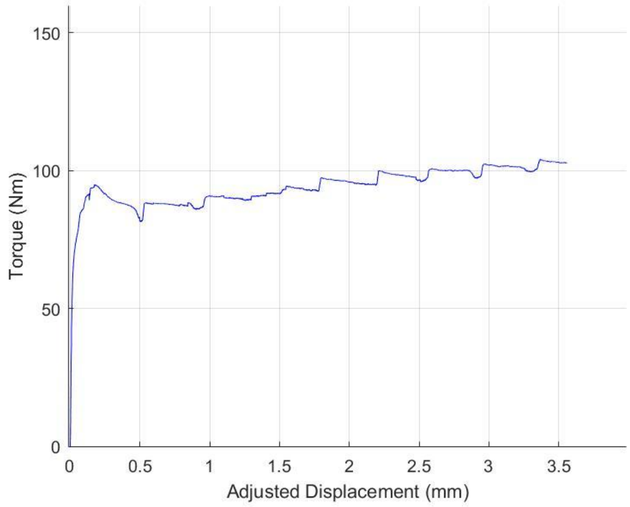

(c)

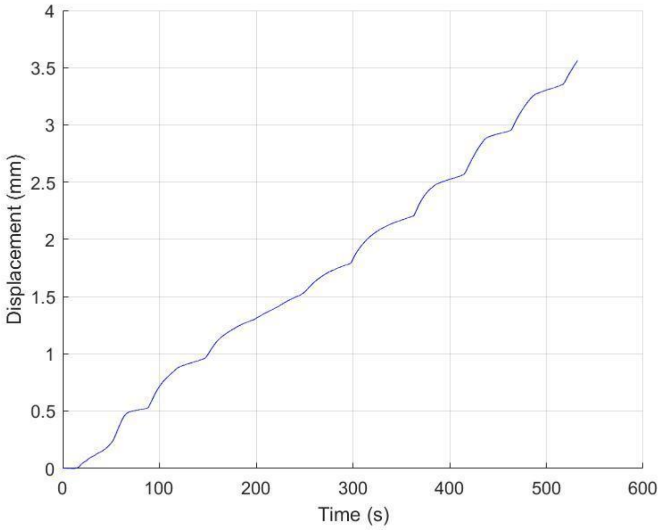

(d)

Figure 84: (a) Torque data from HPT test at 3.3GPa; (b) Displacement and time data at 3.3GPa; (c) Torque data at 4GPa; (d) Displacement and time data at 4GPa to show rate

From Figure 84(a) and Figure 84(c), it is evident that there was an increase in the torque required as the pressure is increased as would be expected. However, the undulation of the data was due to slipping taking place due to both the surface of the HPT sample and the anvil not having the appropriate surface condition needed to ensure good grip.

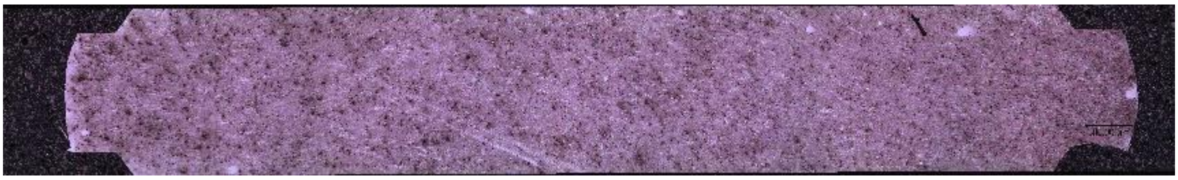

Figure 85: Specimen from 4GPa test with no visible deformed layer formed after etching in oxalic acid after nothing was evident in Nital

Figure 85 shows the specimen created at 4GPa etched with oxalic acid. There was no evidence of deformation when etched in Nital so oxalic acid was then considered as an exploratory means to try and see if microstructural features could reveal any evidence of deformation. Following this 5GPa was chosen as the test pressure.

5.2.2 High pressure torsion disc

A cylinder of rail material was used as the sample, as shown in Figure 81 in the experimental design section 4.2.1. This was cut from the rail head, as shown in Figure 78, and had a diameter of 7.5mm and a height of 7.58mm.

5.2.3 High pressure torsion pilot test

An image of the high pressure torsion machine as well as the anvil positioning is shown in Figure 83 in the experimental design section 4.2.1. Figure 86 shows the result machined HPT disc from the rail head.

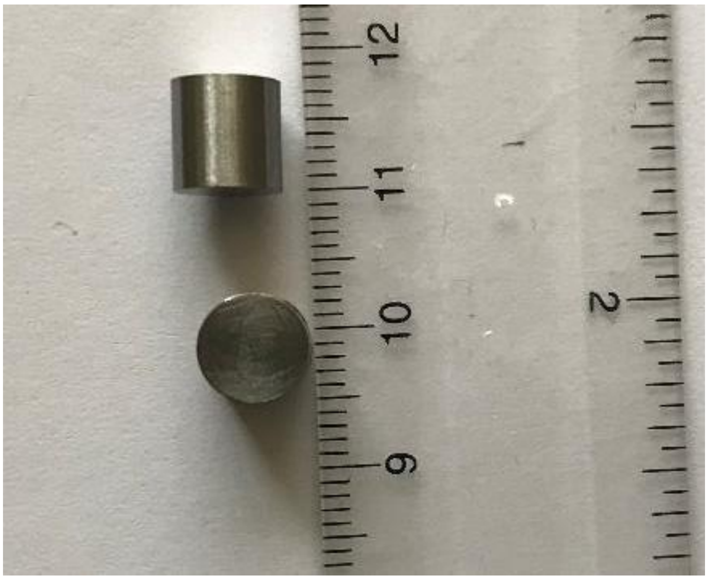

Figure 86: Machined HPT disc

The high pressure torsion sample was marked to show the original longitudinal direction of the rail and then placed between the anvils as shown in Figure 85.

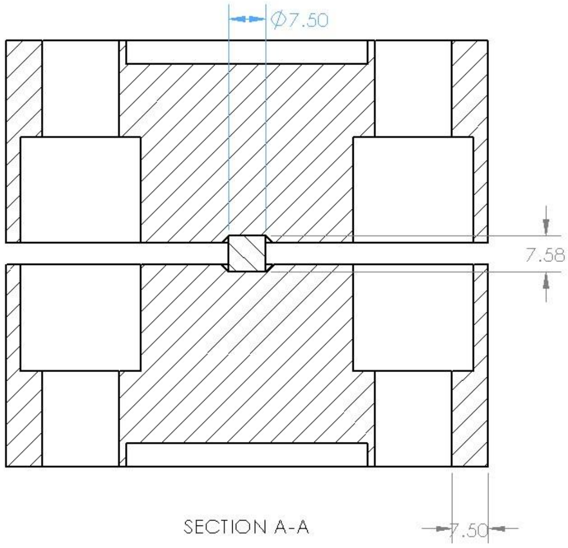

(a)

(b) 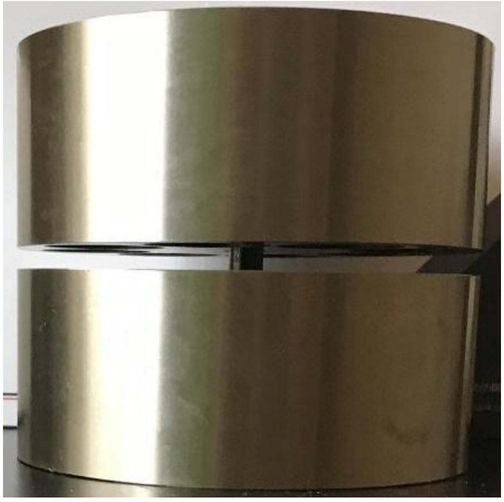

Figure 87: (a) Anvil drawing; (b) Actual anvil and high pressure torsion sample.

A pressure of 5GPa was applied and a rotation of the top anvil was applied to a total angle of 80°, as this is the maximum possible. This was to be done a total of 10.5 times as this equates to 10x80° to achieve a strain of 6 at the target radius of 3.10mm (see Chapter 4).

The HPT anvil was shot blasted to help with preventing sliding during the turning process (Figure 88).

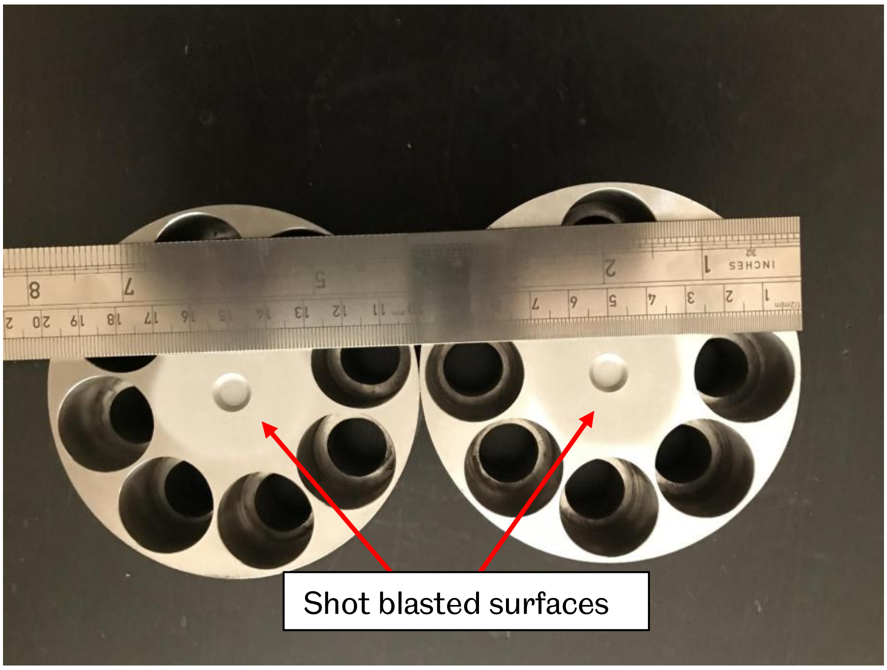

Figure 88: Shot blasted anvils

HPT discs were processed in this manner and labelled in the order in which there were processed i.e., "i" and "ii".

The HPT discs were sectioned as shown in Figure 89 and etched according to ASTM A381. An optical image was taken of the surface to show the grain flow of the deformed HPT sample as well as any inclusions present. A second HPT disc was be used for the FCG test which will be discussed in the next chapter.

(a) 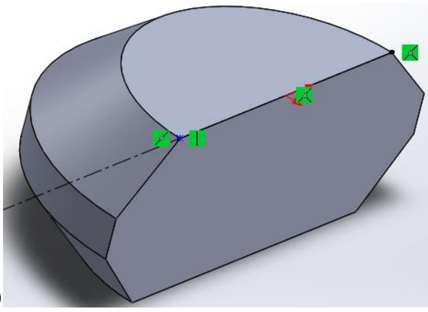

(b) 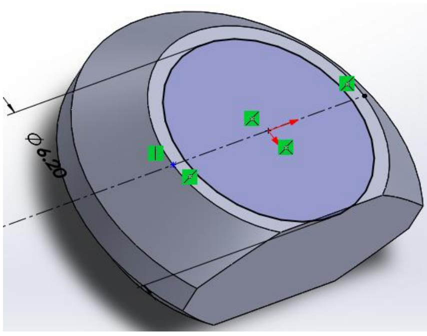

Figure 89: (a) Mid-sectioning of HPT sample; b) Sectioning at target radius of 3.1mm

5.3 High pressure torsion experimental results for R260

5.3.1 Torque data

Figure 90 shows the processed R260 specimen, Figure 90(a) showing the top surface and Figure 90(b) the approximate geometry of the sample after the normal loading and rotation. It can be seen in Figure 90(a), that there are marks on the surface that suggests there has been some relative slip between the specimen and the anvil during the rotation part of the process. Clearly while the anvil has been shot blasted to help avoid this, it has not completely worked.

Figure 90(a) shows the torque data collected during the rotation part of the process. This is useful to show how the strain in the specimen is accumulating. Torque is plotted against "adjusted displacement" which is calculated using $(\frac{\emptyset}{360}) \times 2\pi r$. This is basically the length of an arch, where Ø is the degree of rotation and "r" is the radius of the specimen.

As the rotation increases the rate of increase in torque is reduced as the material strain hardens. The strain hardening has increased from turn 1 to 2.

The slip events are also evident in Figure 91(a) where the torque value has dropped sharply. It can be seen in Figure 91(b) how the displacement has changed at these points as well as how the HPT machine controller has brought the slip back under control.

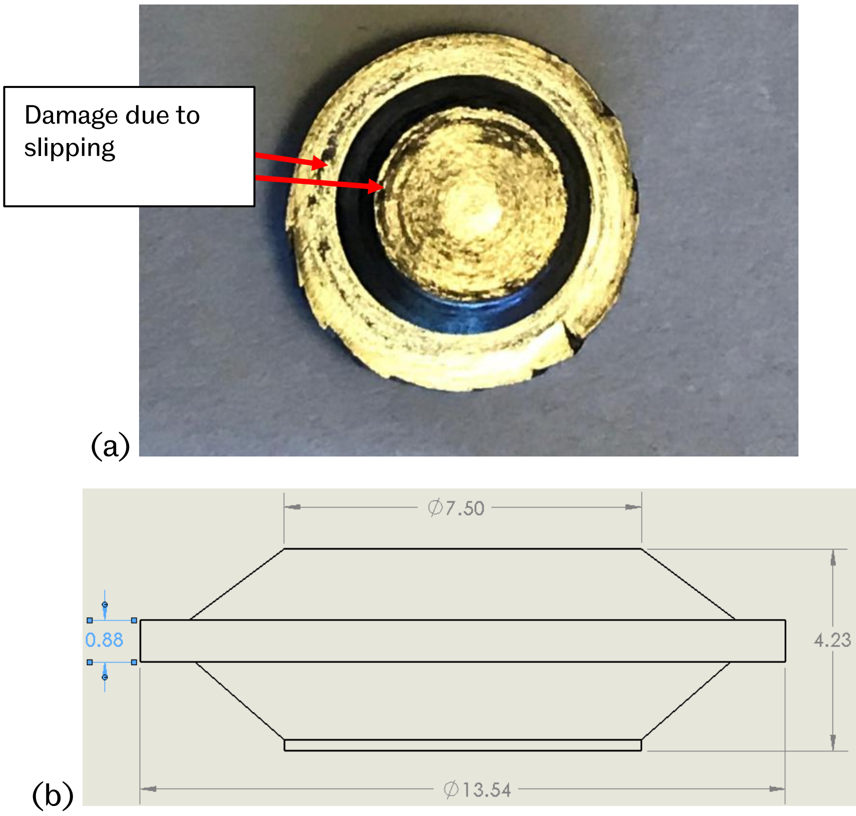

Figure 90: (a) Deformed R260 HPT sample; approximate dimensions of processed specimen

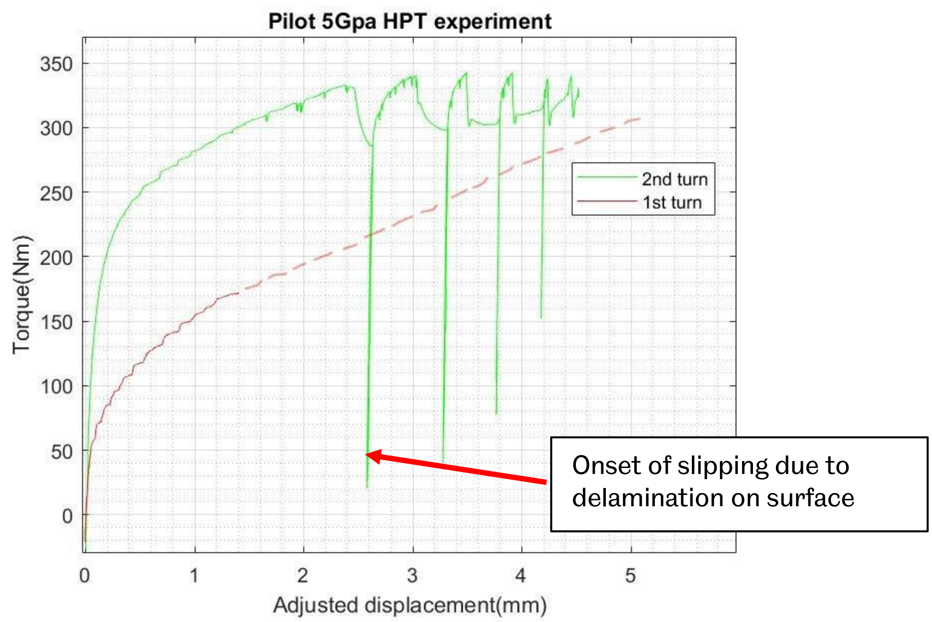

(a)

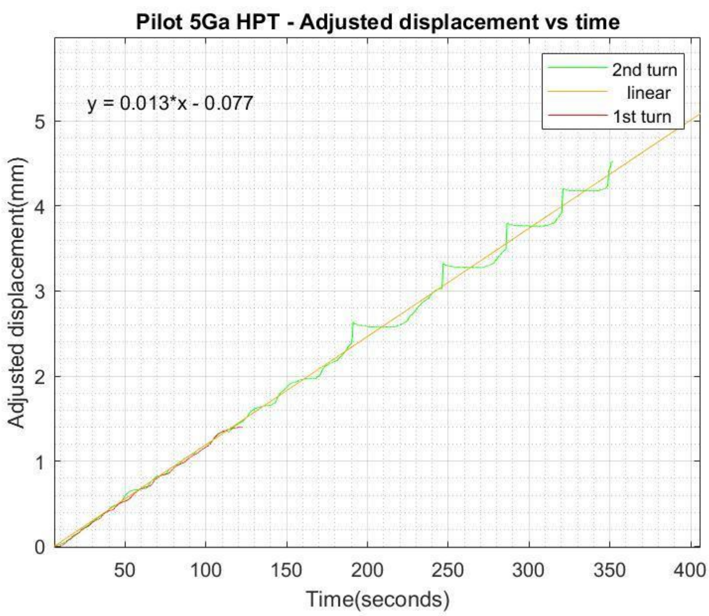

(b)

Figure 91: (a) Torque versus displacement for pilot 5GPa HPT experiment; (b) Displacement time plot.

Figure 92(a) shows the torque data from the second 5GPa test and Figure 92(b) the displacement data. There are many more slip events here, although many are quite small. The increase may have been due to degradation of the anvil surface, which is illustrated in Figure 92(c). However, the torque value imparted was higher than the first test. This test comprised of two turns each of 80 degrees.

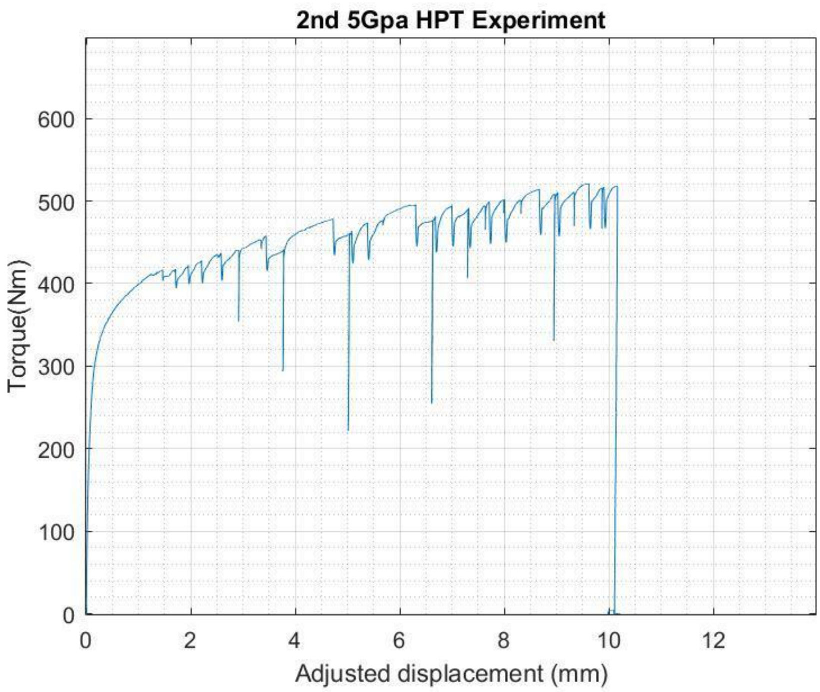
2nd 5Gpa HPT Experiment
Torque(Nm)
Adjusted displacement (mm)
0
100
200
300
400
500
600
0
2
4
6
8
10
12

(a)

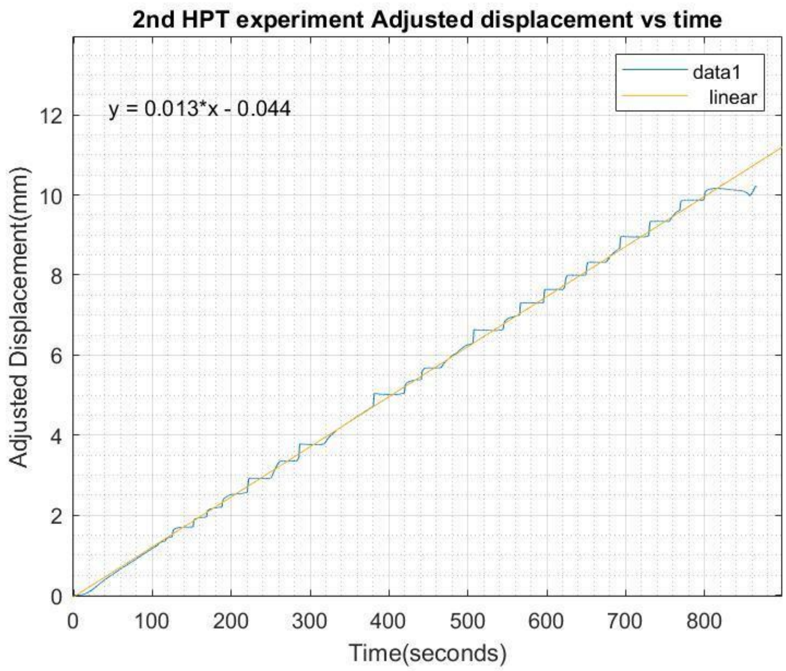
2nd HPT experiment Adjusted displacement vs time
data1
linear
y = 0.013*x - 0.044
Adjusted Displacement(mm)
Time(seconds)
0
2
4
6
8
10
12
0
100
200
300
400
500
600
700
800

(b)

c) 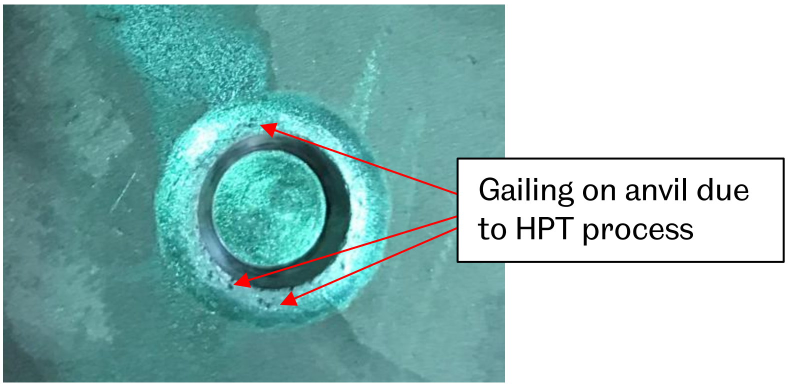

Figure 92: (a) Torque versus displacement for second 5GPa HPT experiment; (b) Adjusted displacement and time data; (c) Anvil condition post-test

5.3.2 Microstructure and hardness

Figure 93(a) shows how the first tested 5GPa disc was sectioned with the surface exposed at the centre and at 3.1mm, along with the location of FCG specimen extraction where strain should in theory be 6.64. The samples were sectioned, mounted in Bakelite and ground/polished to achieve a 1 micron finish and then etched in 2% Nital solution to expose the microstructure.

Figure 93(a) shows the etched surfaces. The deformed layer that is the subject of this investigation is clearly visible in the centre of the specimen. The test has successfully created what was intended. The microstructure outside of this is also compressed as a result of the initial normal force applied. It would be interesting to see if the required deformed layer was created with this load application alone and exactly what the effect of the rotation is on the microstructure. Figure 93c is an attempt to try and quantify the grain size of the microstructure. The structure is severely deformed that it is not possible to distinguish where the grain boundaries are which is needed to quantify the grain size.

(a)

(b)

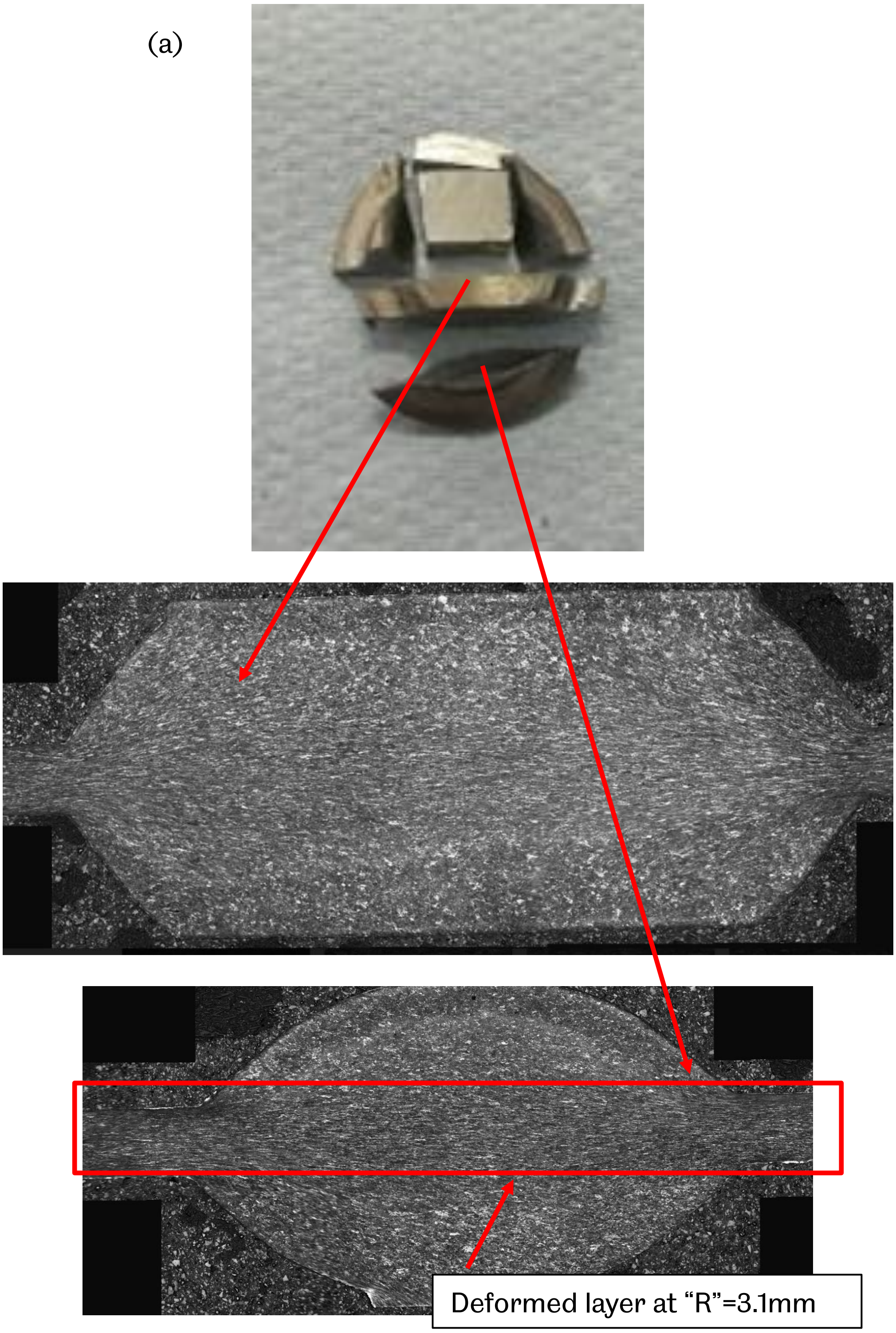

(c)

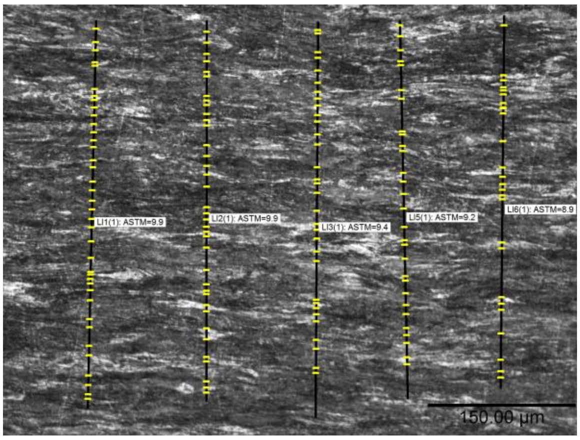

Figure 93: (a) Sectioned 5GPa HPT specimen; (b) Etched surfaces at the centre and at 3.1mm; (c) Grain size quantification of deformed layer

(a)

(b)

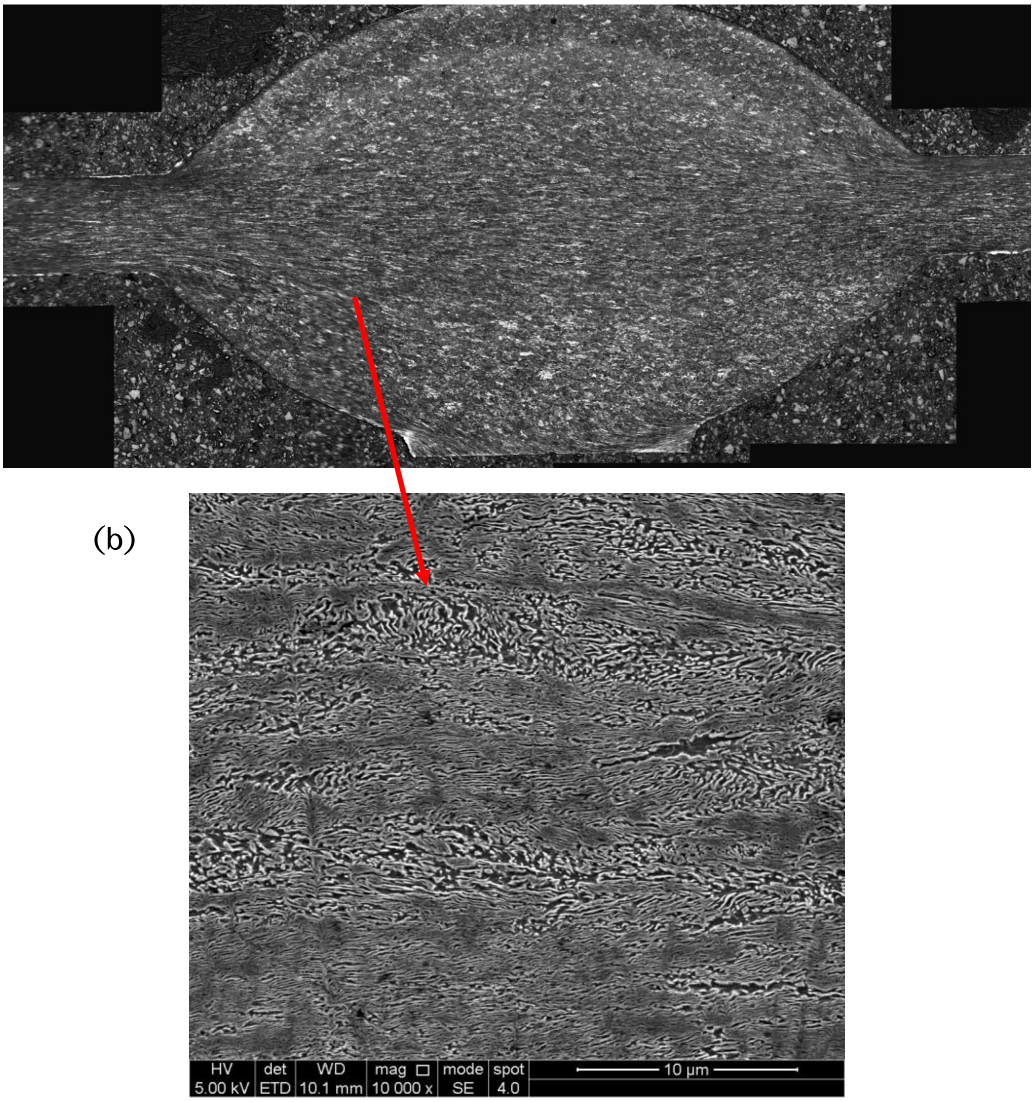

(c) 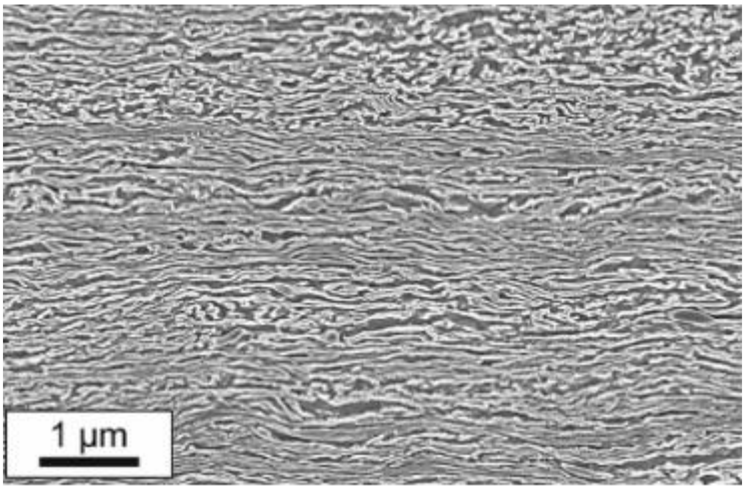

Figure 94: (a) Sectioned 5GPa HPT sample with deformed layer; (b) SEM of deformed layer showing aligned cementite; (c) Aligned microstructure from previous work (Leitner *et al.*, 2018)

Figure 94(a) shows the SEM image of the first 5GPa HPT sample at the target radius. The grains are clearly aligned in the shear direction. Most of the lamella also appear to be aligned in the shear direction just like the grains which is visible in Figure 94(b).

Figure 95 shows SEM images of the second HPT specimen from which the FCG samples were cut from. Figure 95(c) shows the grains clearly deformed and aligned in the shear direction. Figure 95(d) is an image of the deformed layer formed in a previous HPT experiment on R260 at a pressure of 5GPa. Its location is not clear, however, from the scale of the image. The deformed layer formed in the current work is significantly larger in thickness and sufficient to take samples from for further study. As well as the evidence of the formation of the deformation layer, the scale of the deformed layer formed is significantly more when compared to previous work done elsewhere (Leitner *et al.*, 2018). Figure 94b appears to show some similarities microstructurally to 94c. However, it is not sure exactly where in the specimen it is taken.

Overall, the grains align in the shear direction when Figure 94(a) and 95(b) are compared which is evidence of the repeatability and effectiveness of the process. The difference in Figure 94(b) and Figure 95(c) is not quite clear. It could be due to difference microstructural feature present. Figure 95(c) shows a pro-eutectoid ferrite phase which has undergone deformation. This feature is not present in Figure 94(b).

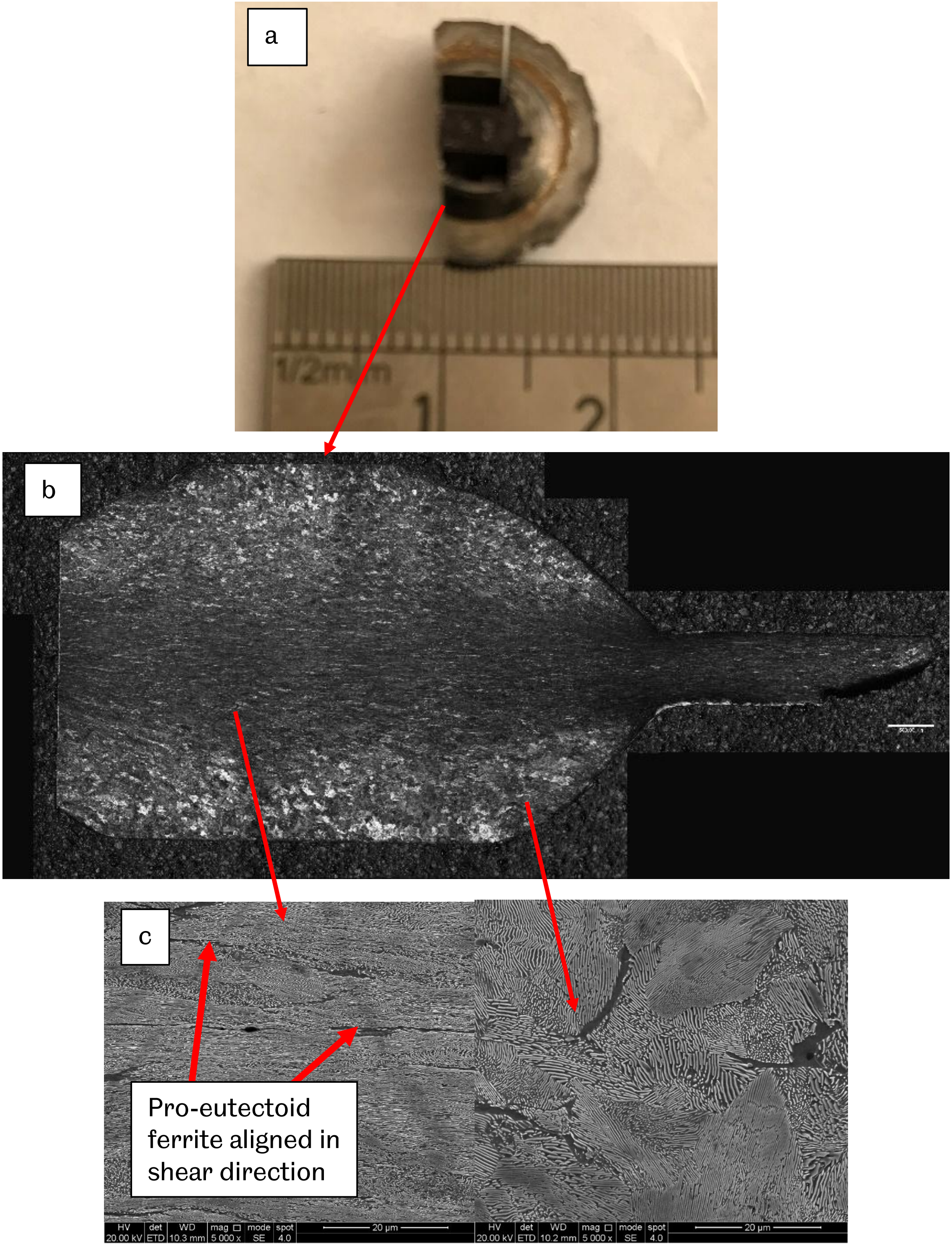
a
1/2mm
1
2
b
c
Pro-eutectoid ferrite aligned in shear direction
20 µm
20 µm

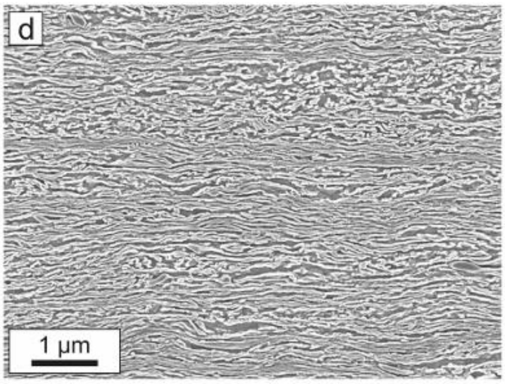

Figure 95: (a) Sectioned HPT specimen from 5GPa with FCG already extracted from radius of interest; (b) Metallography of deformed layer from radius of interest; (c) Secondary electron microscopy of deformed layer at radius of interest; (d) Deformed layer from Leitner *et al.*(2018)

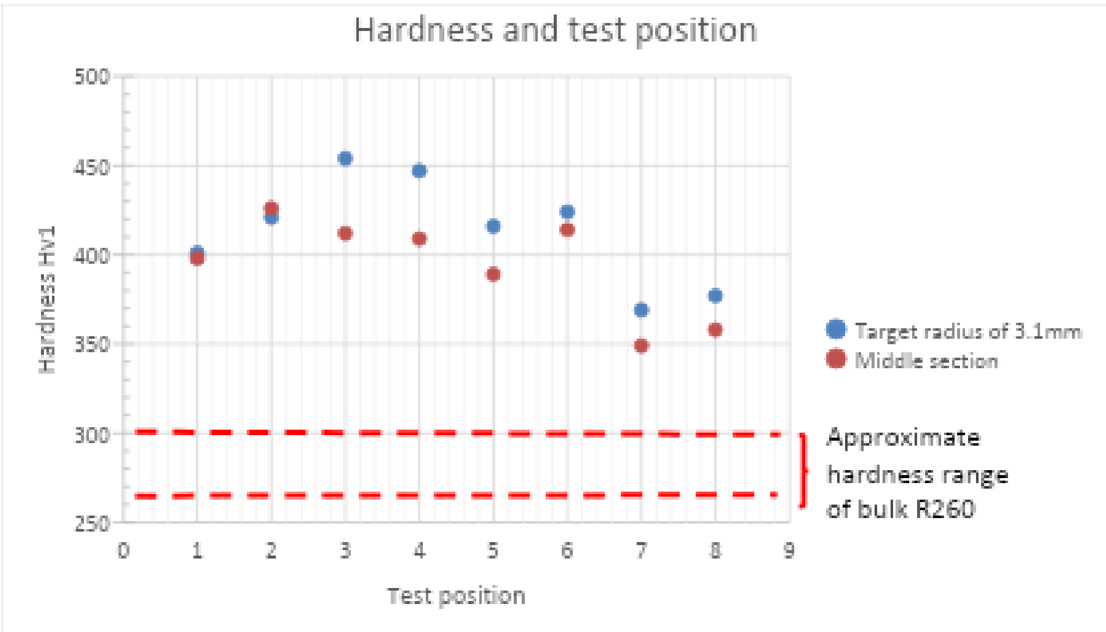

(a)

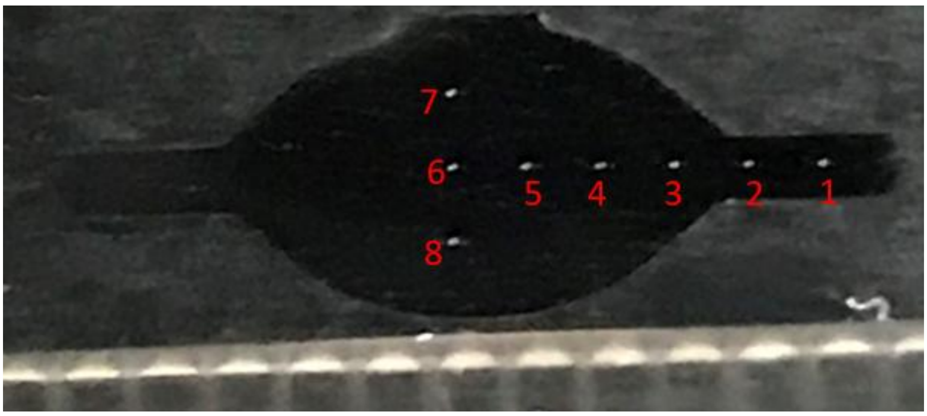

(b)

(c)

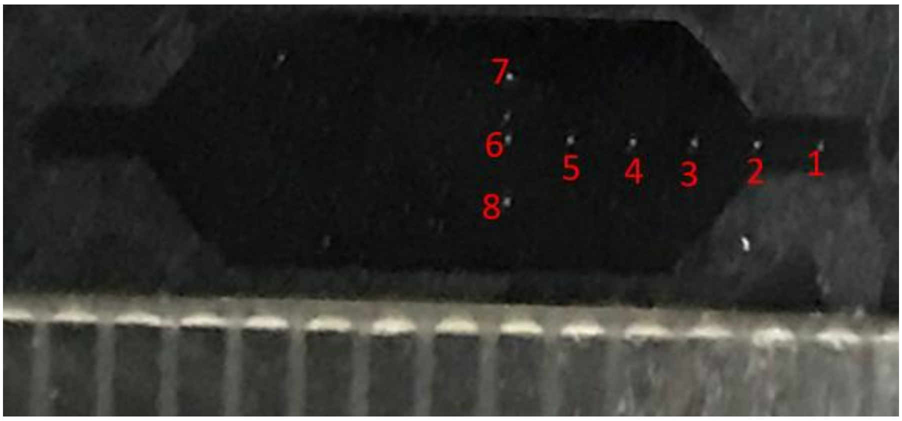

(d)

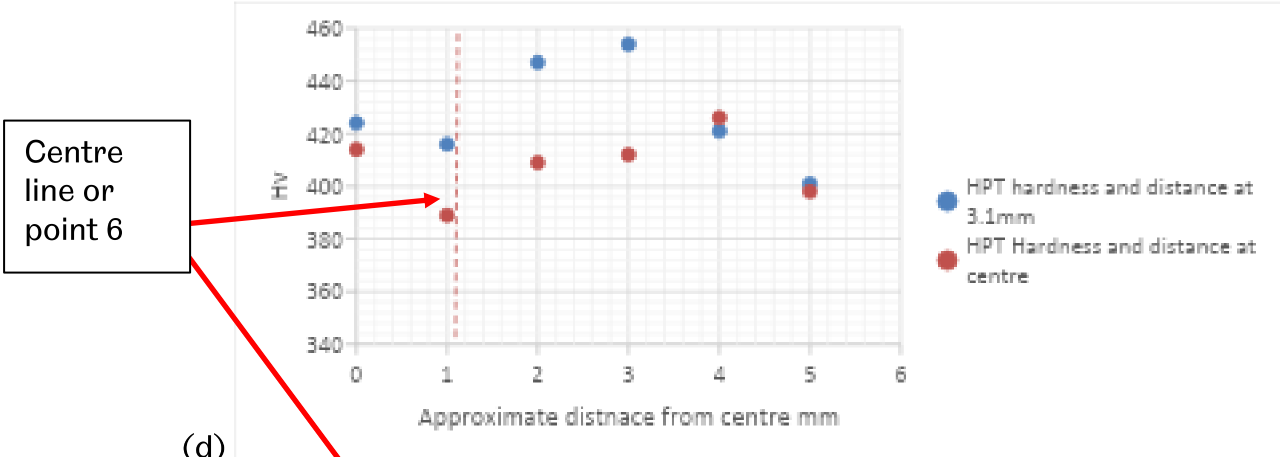

(e)

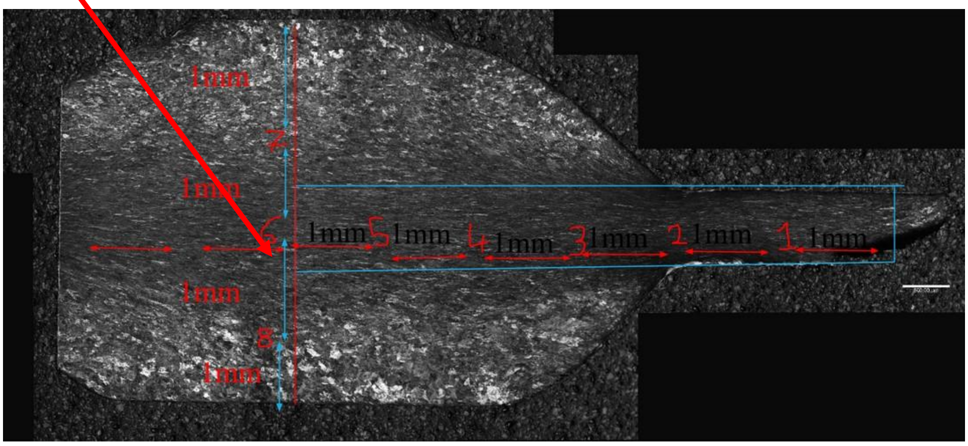

Figure 96: (a) Hardness data for first specimen; (b) Hardness measurement locations for first specimen approximately 1mm apart at target radius of 3mm; (c) Hardness test locations at mid-section for first specimen; (d) Hardness data against approximate distance from centre and at target radius of 3.1mm for second specimen; (e) Etched image of second specimen with approximate distance from centre at target radius of 3.1mm

The hardness profile displayed in Figure 96(a) is what is expected from an unconstrained high pressure torsion process. A constrained pressure torsion process would lead to an increase in the material hardness even into the tapered region. This is shown in Figure 97(b) and another distinction from the device used previously by Leitner (Leitner *et al.*, 2018).

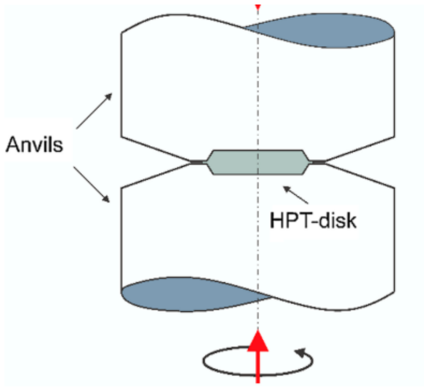

(a)

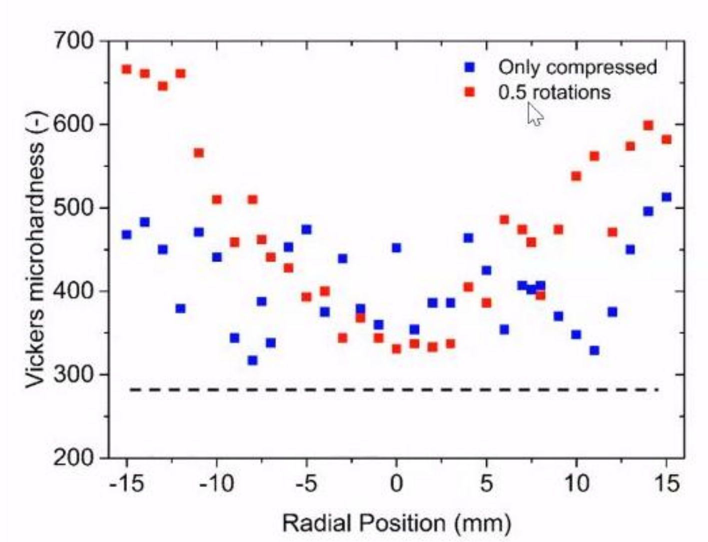

(b)

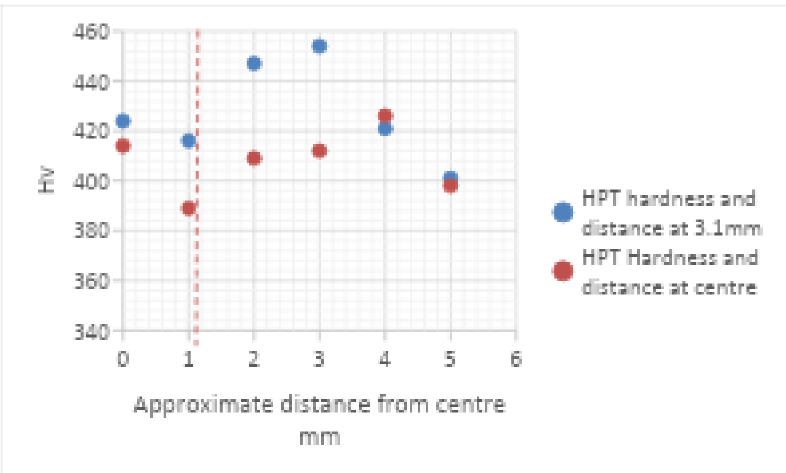

(c)

Figure 97: (a)Section from Constrained HPT sample (Hohenwarter and Pippan, 2019); (b) Hardness profile from Materials Center Leoben (MCL) test (unpublished – included here with permission); (c) Hardness profile across the second 5GPa specimen sample from this research.

The hardness reading appear to be inconsistent from previous research with results for compression only being higher than results from when rotation is added. This could be due to the extremely thin layer present or probably due to its absence and rather just a compressed or cold worked region formed. Another distinction from the deformed layer formed in the current work compared to previous work is the continued increase in hardness towards the outer radius of the HPT sample. The hardness starts to drop in the HPT sample created in the current work which is due to it being an unconstraint process while it appears to continue to increase in the previous MCL work which is indicative of it being constrained process. This could also indicate the presence of residual stress with the FCG sample extracted.

More R260 HPT experiments were conducted to further show the repeatability of the process. The thickness formed in each experiment is shown in Figure 98(a).

From Figure 98(a), the difference in deformed layer thickness across the first three specimens is relatively low. It becomes more variable for specimens 4 and 5, but this could be due to anvil wear.

Torque data for the specimens is plotted in Figure 98(b). The increase in torque is as a result of the material work hardening which is further evidence of the formation of the deformed layer. The difference in displacement reported was as a result of the machine not recording the data generated.

Table 10 shows the Von mises strain calculated for each layer (using Equation 4). The strain values are as anticipated (see Chapter 4).

Using the thickness of sample 1 and applying Equations 4 and 5:

$$\gamma = \frac{2\pi r N}{t\sqrt{3}}$$

"t" = 0.88, r = 3.75, N = Degree of rotation which was derived by dividing the maximum length achieved in the turn by $2\pi r$, t = 0.88 (this is the thickness of the layer created after the HPT process

γ = 6.56

Whilst the complete torque data is not available for all the experiments, the rotation continued until the sample could no longer be turned on all samples.

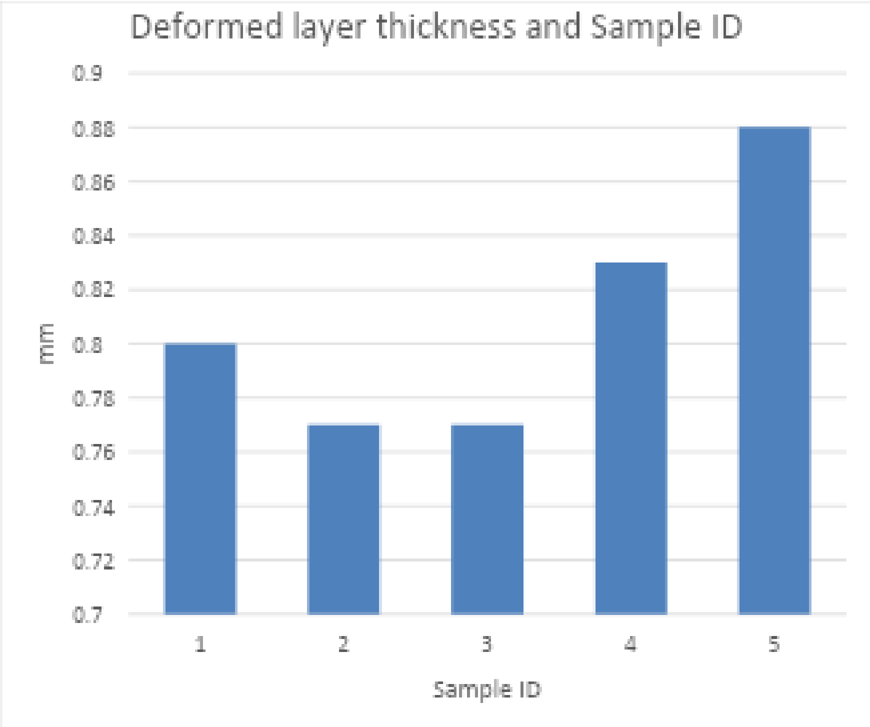

(a)

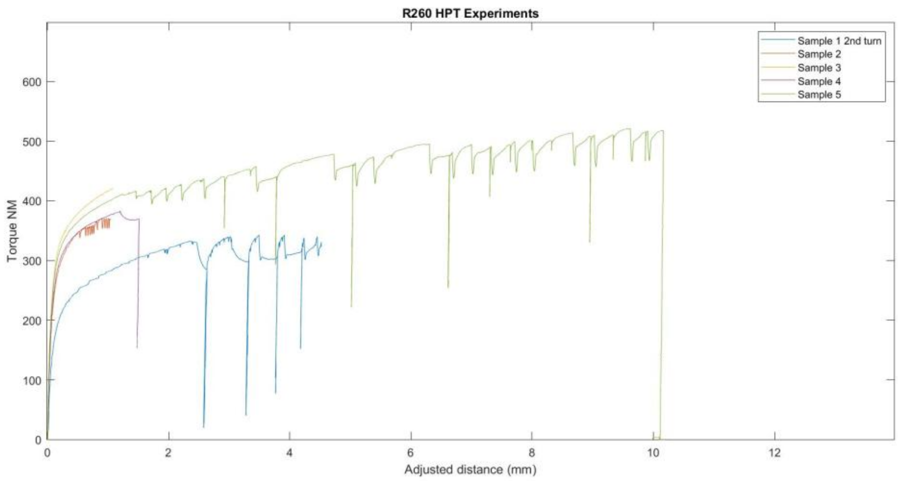

(b)

Figure 98: (a) R260 sample ID and the measured deformed layer thickness, (b) Torque data

Sample ID	Measured thickness (mm)	Von-Mises Strain at 3.1mm radius
1	0.88	6.56
2	0.8	7.22
3	0.77	7.5
4	0.77	7.5
5	0.83	6.96

Table 7: Deformed layer thickness and calculated strain at 3.1mm radius

5.3.3 R260 HPT, twin disc and in-service comparison

As stated in the design section, the strain level of in-service rail at the interface has been measured as approximately 6 on a straight track based on a mixed traffic condition but can vary depending on the location in addition to the maintenance regime used. For example, use of friction modifiers reduces the shear stress and thereby the strain experienced by the material, while tracks in curves will experience a higher amount of strain compared to straight tracks. Rail speeds can also influence the strain experienced (He *et al.*, 2016). As a result of this, the comparison between the HPT processed samples from Section 5.3 and actual rail given here will be a general overview.

Overall, the conditions at the wheel-rail interface lead to the formation of a deformed microstructure, an example of which is shown in Figure 98(b).

(a) 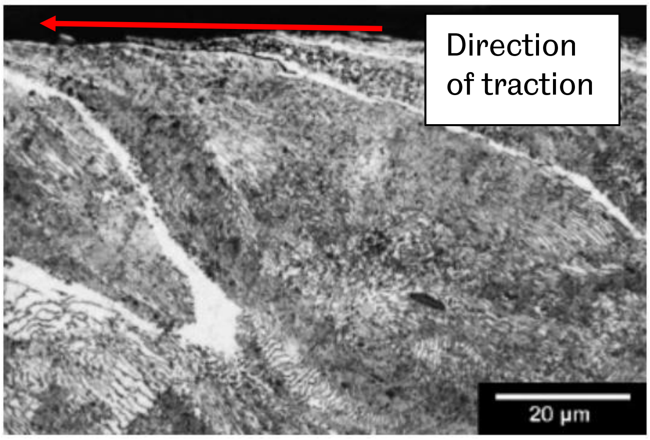

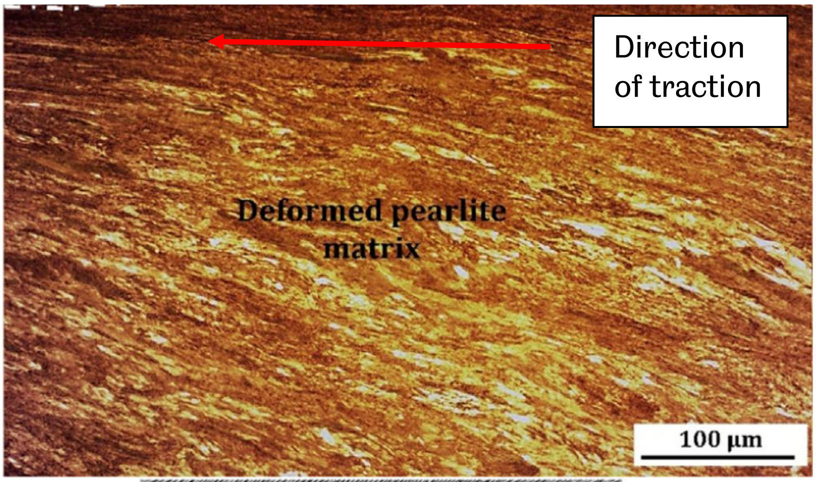

(b)

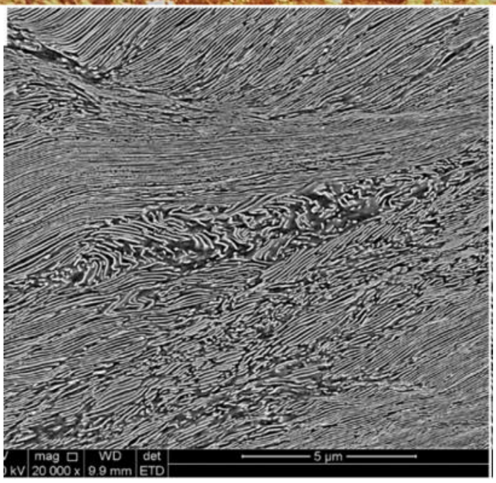

(c)

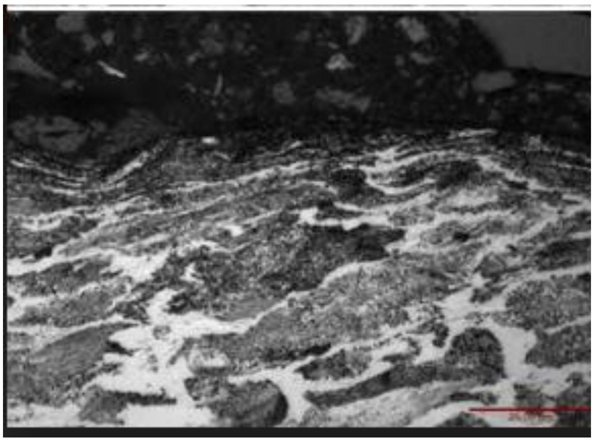

Figure 98: (a) Microstructure from twin disc test of R260 material (Garnham and Davis, 2008); (b) Microstructure of in-service R260 from a 344m radius curve and an SEM image of deformed layer (Masoumi *et al.*, 2018); (c) Full scale rig microstructure after 5,000 cycles (Yildirimli et al., 2024)

Figure 98(a) shows a microstructure created during a twin disc experiment using R260 rail material (1500MPa, 1% slip, 400rpm) from Garnham and Davis (2008). It is noticeable that the grains are aligned similarly to the in-service material in Figure 98(b). The absence of ferrite in the in-service material which is noticeable in the twin disc material, is down to the chemistry of the individual material. Even though they are both R260 material, the range is wide and can result in various microstructural features being present or absent. Figure 98 shows an absence of sulphides which are present in Figure 18.

The deformed layer because of the HPT process also shows this in Figures 94 and 95. Both are from two different batches of rail material and it is evident in Figure 95 that there is an abundance of Pro-eutectoid ferrite present in the microstructure. The ferrite aligns in the shear direction, as shown in the Figure 95. This is similar in comparison to Figure 98(a) which shows the ferrite been aligned in the shear direction in the twin discs. But one noticeable difference between the HPT deformed layer and the twin disc is the amount of deformed layer that is created.

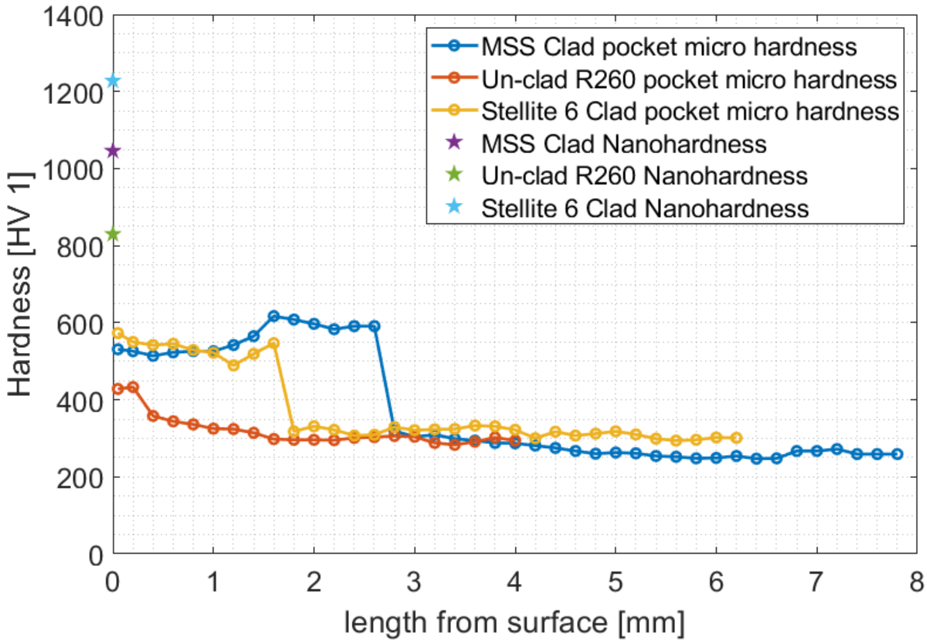

(a)

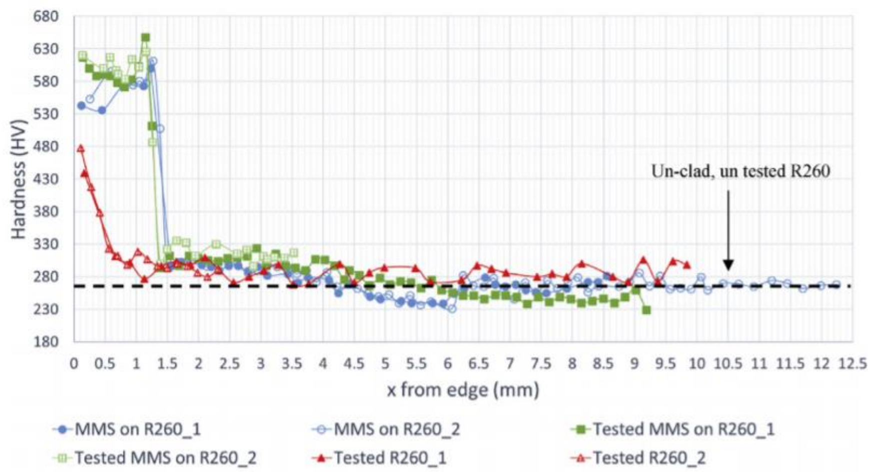

(b)

Figure 99: (a) Hardness profiles in a rail head from full-scale testing (Yildirimli et al., 2024); (b) Hardness profiles from twin disc tests (Lu *et al.*, 2019)

The maximum hardness achieved in the R260 deformed layer of the HPT process is 415Hv from the mid-point to 454Hv at the outer circumference of the deformed discs (see Figure 97(c)). Full-scale tests of R260 under realistic conditions of load and slip yielded similar hardness values, as shown in Figure 99(a). This shows the strain levels reached in both the HPT and full-scale contact are similar. The hardness is also similar to that seen in twin disc tests (see Figure 99(b)), the other approach that could have been used to create a deformed layer.

Figure 100 shows nano hardness data for the deformed layer and the material just below.

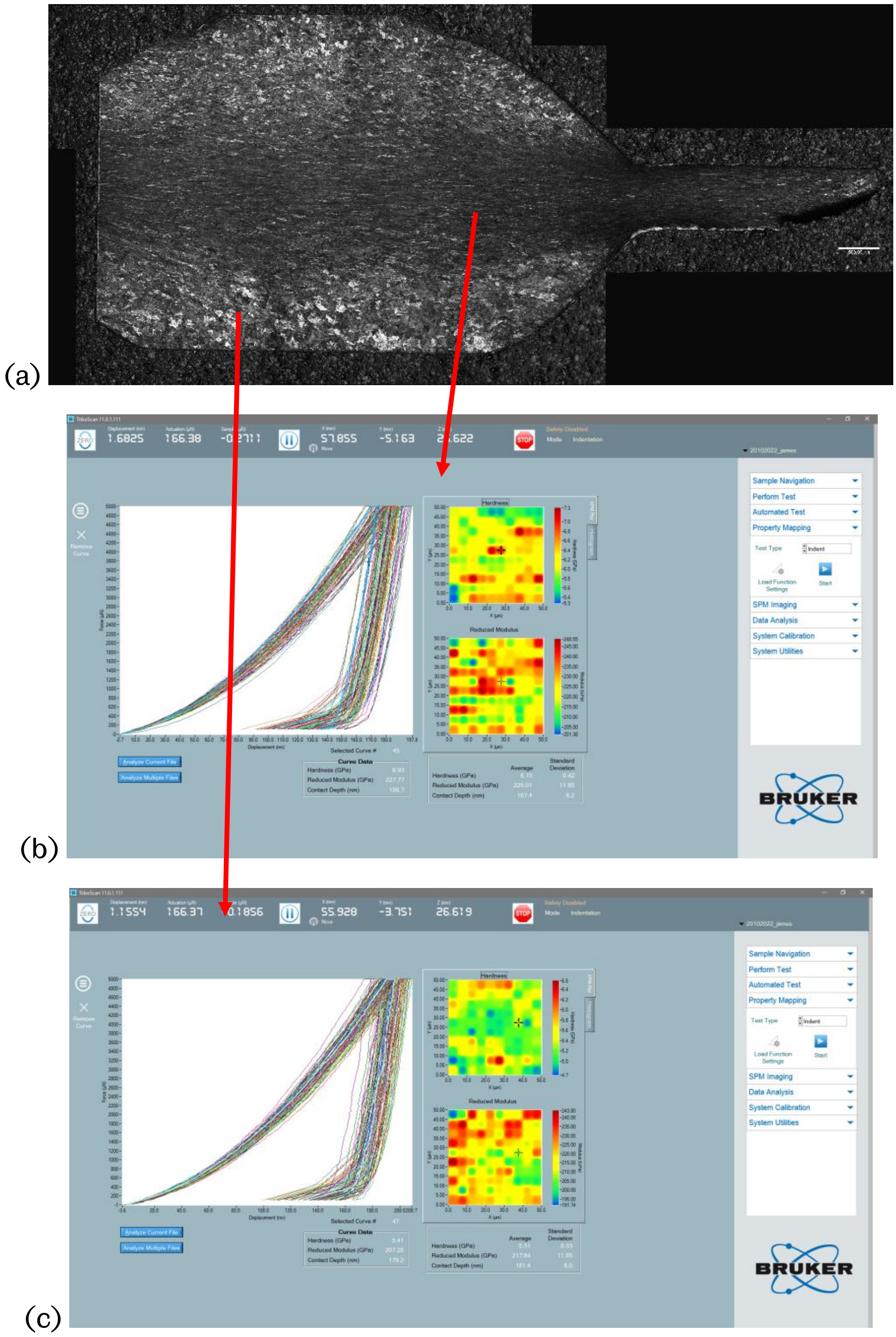

Figure 100: (a) Deformed layer; (b) Nano indentation result of deformed layer averaging 6.15GPa (627Hv); Nano indentation result of region below deformed layer averaging 5.31GPa (541Hv)

5.3.4 HPT experiment discussion

It is evident from the images in Figures 90 and 93 to 95 that the deformation takes place in the middle of the sample with the grains aligned in the direction of shear.

The strain within this region can be calculated using the thickness of the deformed layer as opposed to the thickness of the entire HPT sample as suggested in the experimental design section. As a result of this the maximum strain that can be achieved with the entire FCG specimen fully enclosed within the HPT sample ranges from 6.64 to 7.6 at a radius of 3.1mm which is slightly higher than the strain of 6 which is reported to exist at the wheel-rail interface on mixed traffic rail. This is due to the variation in the thickness of the layer that is formed due to the wear of the anvil after each process.

The hardness profile in Figure 96(a) shows the strain is concentrated in the central region of the processed HPT disc at the target radius and was taken from sample 5 in Table 7. Even though there is an increase in hardness, the hardness profile moving from the start of the taper towards the other side of the specimen shows a drop. This contradicts Equation 4 which is used to calculate the strain thereby indicating a drop in strain at the start of the taper. The taper was introduced to aid in strain homogeneity, but the hardness result shows the presence of this taper actually reduces amount of strain experienced by the material in this region.

The torque requirement appears to be lower than what is calculated in the experimental design section (see Chapter 4). This could be due to a few reasons. Firstly, the shear stress versus strain graph was generated (see Figure 80) at a pressure of 6GPa therefore it is not the same as my experiment which was conducted at 5GPa. Also, the two turns were done one week apart. The second HPT process which shows a higher final torque value is due to the process being carried out in one go. The slight drop in torque results is due to galling occurring at the anvil interface due to the highly demanding process of the high pressure torsion experiment.

The repeats of the HPT process on the other samples, as shown in Figure 91(b), show consistent behaviour in terms of torque increasing then levelling off. The is due to the work hardening effect of the process taking place.

5.3.5 Conclusions

From the work carried out using the HPT process to generate deformed layers in R260 material, the following can be concluded:

- The process is capable of repeatedly creating a deformed layer
- The volume of layer is appropriate for creating FCG specimens. The schematic shown in Figure 101 indicates that the entire notch is within the deformed layer created

- The microstructure and hardness of the deformed layer is similar to that seen in extracted rail from the field and rail from full-scale laboratory tests

- Issues arise with slip of the specimens relative to the anvils. This can be reduced through good surface preparation and load selection. However, the state of the anvils must be monitored and re-finishing applied where needed.

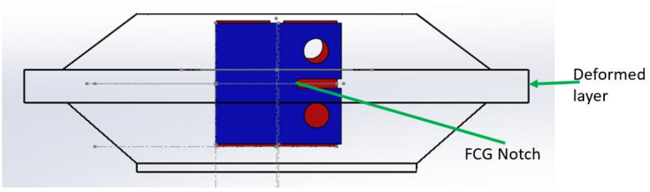

Figure 101: FCG specimen dimensions overlaid on a processed HPT specimen

5.4 HPT of premium rail materials

5.4.1 Introduction

In light of the response of the R260 to the HPT experiments. R350 and R400 material were processed to see how their behaviour compares. The materials were processed in the exact manner as described in the pilot R260 experiment (see Section 5.3.2).

5.4.2 R350 HPT results

The sample parameters used for the R260 were applied to try and replicate a deformed layer for the R350HT material. There is no evidence of this ever been done at the time of processing.

Figure 102 shows the data collected from an HPT test of an R350HT sample. The test was run at a contact stress of 5GPa over 0.24 turns of 80 degrees. As noted in Section 2, R350HT rail is also pearlitic rail, but has enhanced properties over R260 as a result of the heat treatment it undergoes. This is immediately evident in the hardness plot shown in Figure 102(a), where hardness of the deformed layer can be seen to be between 450 and 500Hv, compared with seen for 420Hv for R260. The hardness is very consistent in the deformed layer (points 1-6 (see Figure 102(b)), which is good for FCG specimen manufacture. The hardness is slightly lower at points 7 and 8, from above and below the deformed layer respectively, as would be expected and this is only affected by the initial compression applied to the specimen.

The torque recorded (see Figure 102(f)) was consistent between the cycles data was available for. The value recorded was similar to that seen in the early cycles for R260. The resulting thickness of deformation is shown in Figure 102(c). The value is higher than that seen for the R260. The microstructure in the deformed layer is shown in Figures 106(d) and e. As can be seen the microstructure aligns in the shear direction.

Figure 102(g) shows the nano indentation measurements taken in the deformed layer. The average value of the 10x10 matrix was 6.78GPa and the spread was approximately 5-8GPa. The high pressure shows how and why it is still able to withstand the 2700MPa pressure experienced at the contact patch (Lewis and Olofsson, 2009).

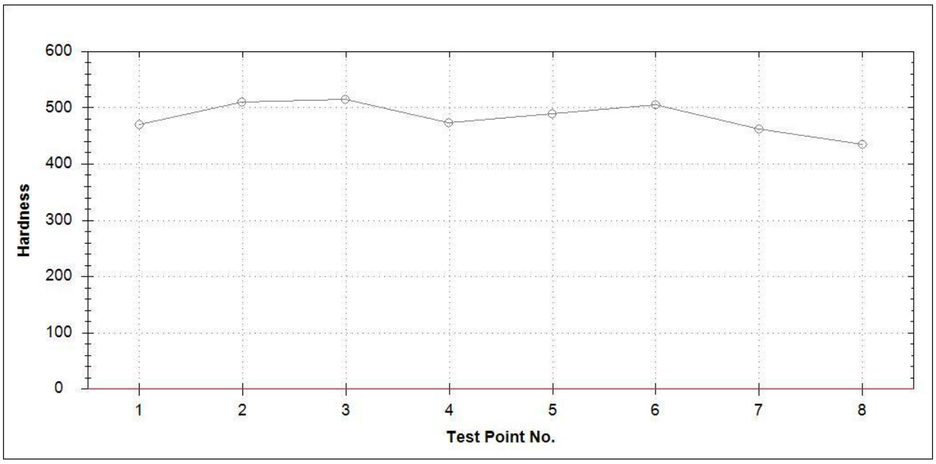

(a)

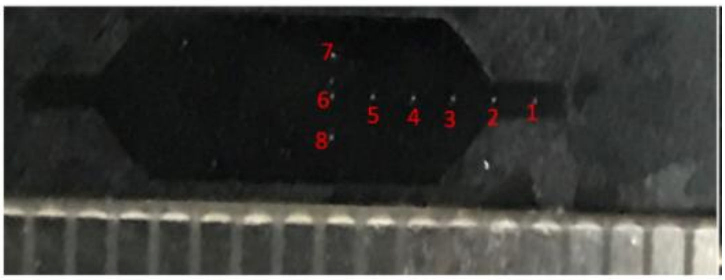

(b)

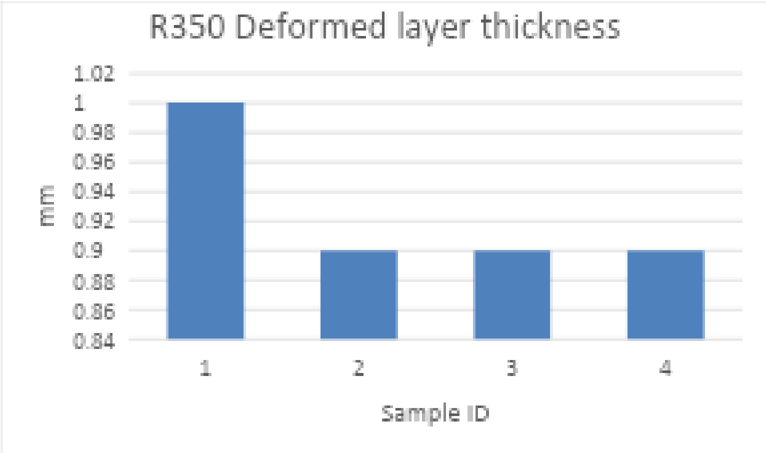
R350 Deformed layer thickness
mm
Sample ID
1.02
1
0.98
0.96
0.94
0.92
0.9
0.88
0.86
0.84
1
2
3
4

(c)

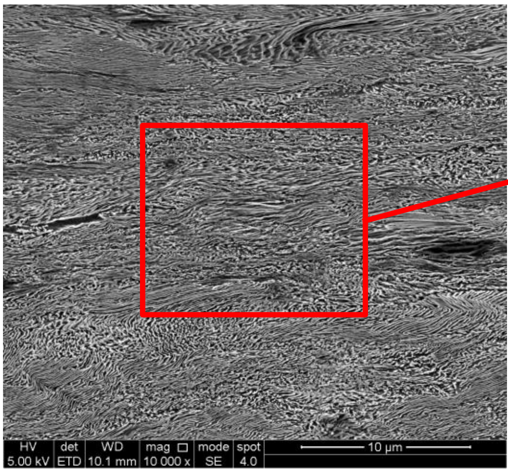
HV 5.00 kV
det ETD
WD 10.1 mm
mag 10 000 x
mode SE
spot 4.0
10 µm

(d)

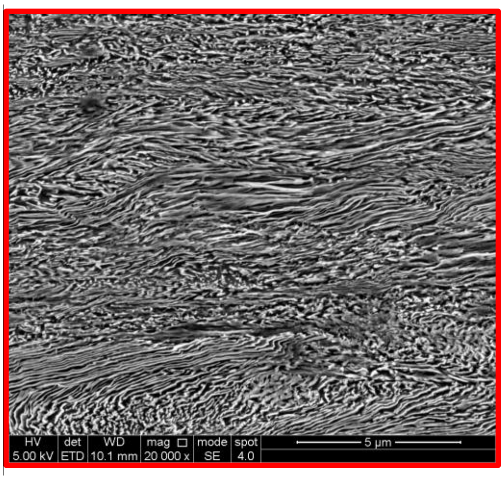
HV 5.00 kV
det ETD
WD 10.1 mm
mag 20 000 x
mode SE
spot 4.0
5 µm

(e)

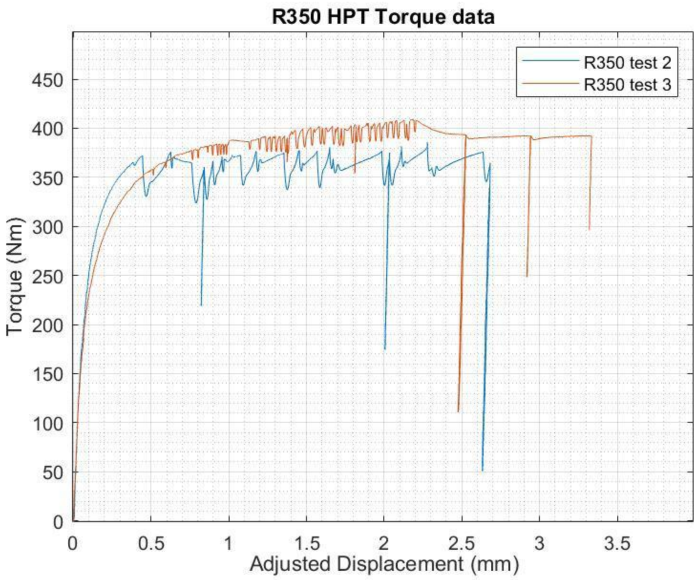
R350 HPT Torque data
R350 test 2
R350 test 3
Torque (Nm)
Adjusted Displacement (mm)
0
50
100
150
200
250
300
350
400
450
0
0.5
1
1.5
2
2.5
3
3.5

(f)

(g)

roman numeral	thickness	strain at 3.1mm	CT samples produced
1	1	1.5	
2	0.9	1.7	
3	0.9	1.7	2 CT samples produced
4	0.9	1.7	

(h)

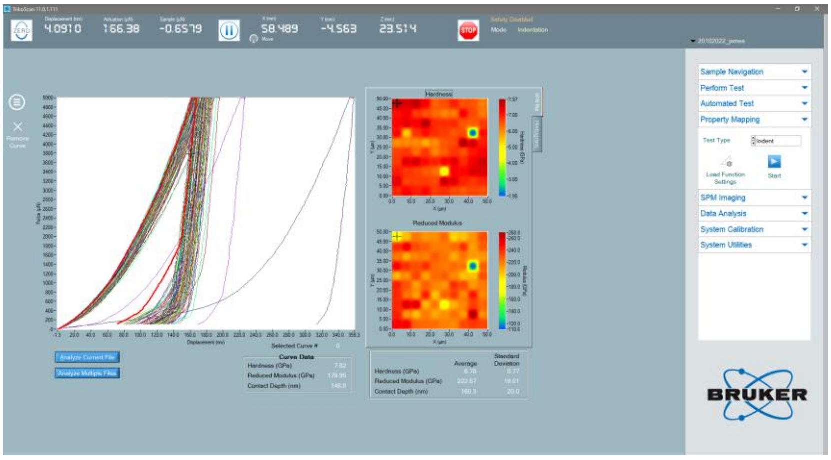

Figure 102: R350HT HPT test outcomes: (a) Micro hardness measurement data; (b) Micro hardness measurement locations; (c) Layer thickness of test samples; (d) SEM image of deformed layer at 10000x magnification; (e) SEM image of deformed layer at 20000x magnification; (f) Torque data; (g) Table showing HPT samples and the number of CT samples produced; (h) Nano indentation of deformed layer

5.4.3 R400 HPT results

The sample parameter used for the R260 were applied to try and replicate a deformed layer for the R400 material. There is no evidence of this ever been done at the time of processing.

Figure 103 shows the outcomes of an HPT test on an R400HT specimen. The test was run at a contact stress of 5GPa over 2 turns of 80 degrees. As seen with the R350HT, the deformed layer is harder than the R260, but only slightly higher than the R350HT (see Figure 103(a)). The maximum torque values measured were more variable, between specimens, as shown in Figure 103(e). The variability is possibly due to the HPT specimens being extracted from different positions in the rail head. As the

R400HT is heat treated, its hardness will decrease with distance down into the rail head from the rail surface (as shown in Figure 104). The microstructure in the deformed layer is shown in Figure 103(c). This is like that seen in the R350HT.

Figure 103(f) shows the nano indentation measurements taken in the deformed layer. The average value of the 10x10 matrix was 7.31GPa and the spread was approximately 6-9GPa. This again is significantly higher than the 2700MPa measured at the contact patch (Lewis and Olofsson, 2009).

(a)

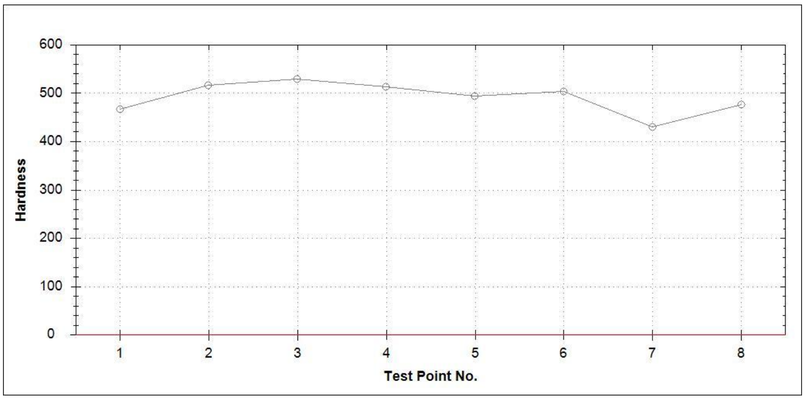

(b)

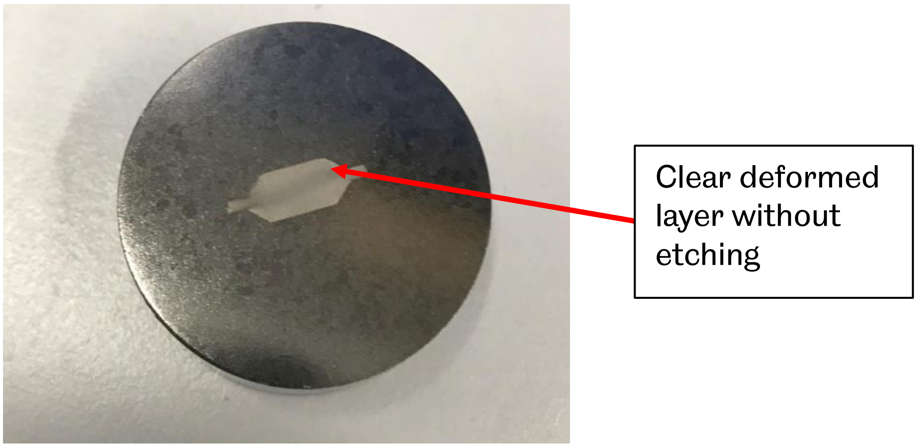

(c)

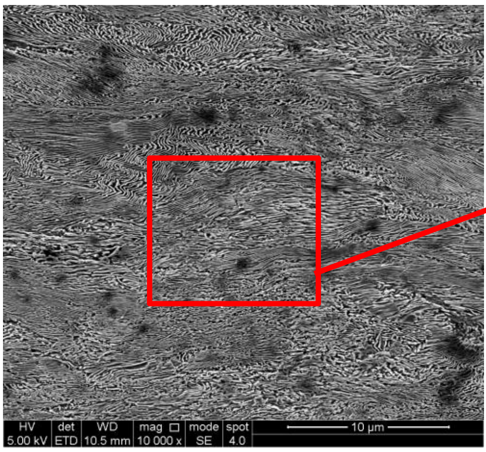

(d)

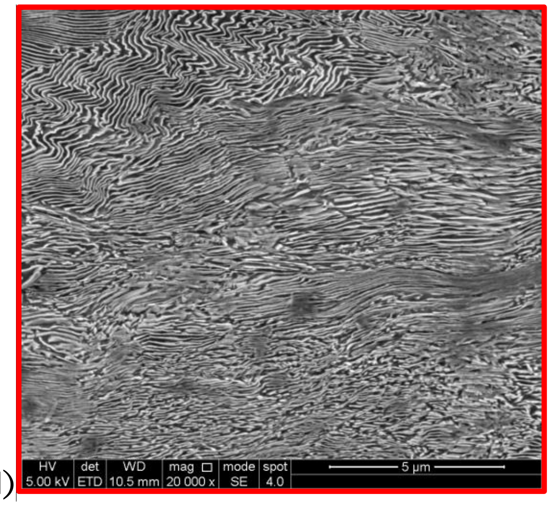

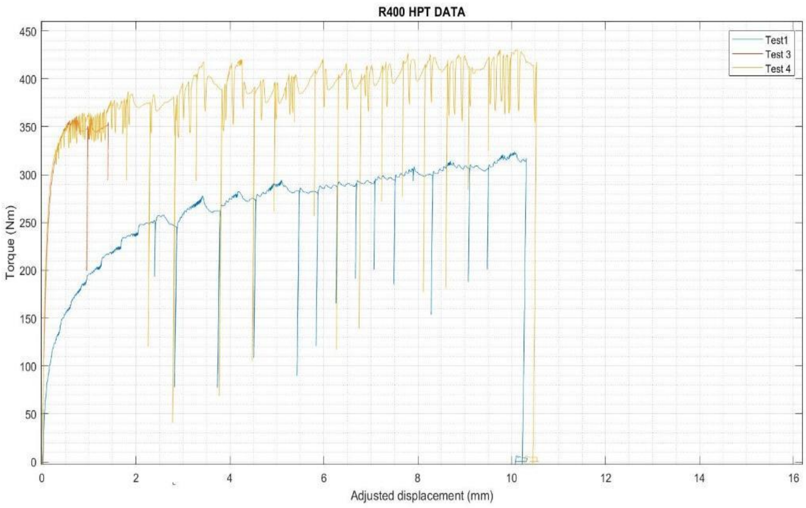

(e)

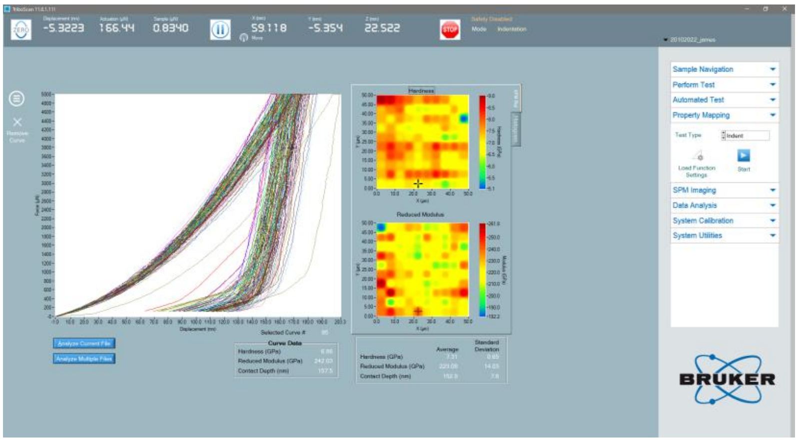

(f)

Sample ID	Deformed layer thickness	Calculated strain at 3.1mm	CT sample produced
1	1	1.5	
3	0.9	1.7	
4	0.9	1.7	2-CT samples produced

(g)

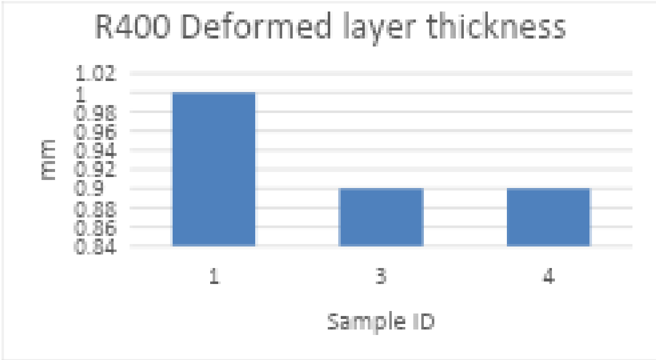

(h)

Figure 103: R400 HPT test outcomes: (a) Hardness profile of deformed layer; (b) Image of deformed layer; (c) & (d) SEM images; (e) Torque data; (f) Nano indentation of deformed layer; (g) Number of samples created, deformed layer thickness and Calculated strain h) graph showing deformed layer and sample ID

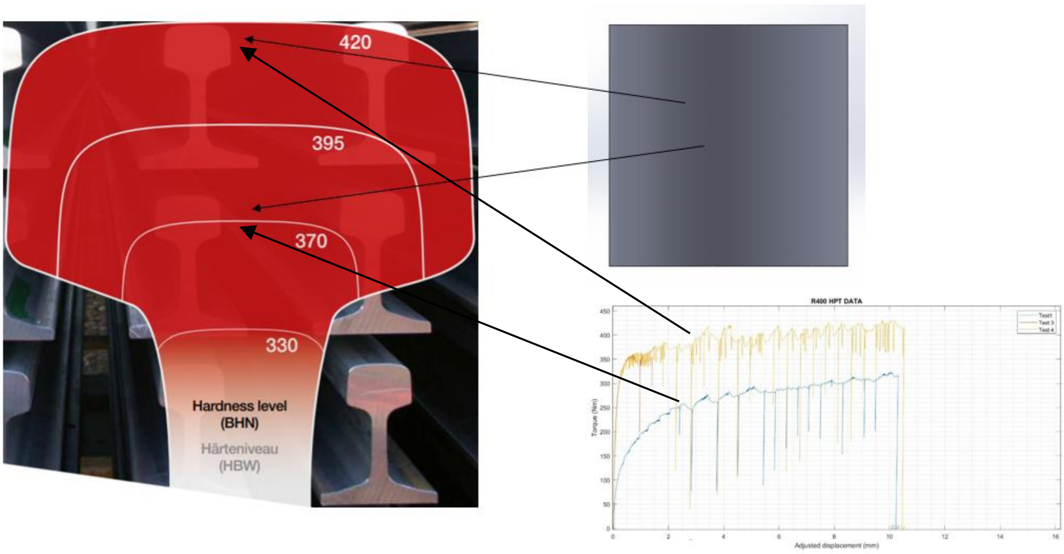

Figure 104: R400HT Rail head hardness profile and associated torque response

5.5 HPT comparison with full-scale wheel-rail rig data

Figure 105 brings together all the HPT outcomes across the three rail grades tested, R260, R350HT and R400HT. These are compared to sectioned rail samples from tests carried out on a full-scale wheel-rail test rig (FSR) (Yildirimli et al., 2024; Yang et al., 2024). The FSR tests were run at a contact pressure of 1300MPa, a slip level of

3% for 5,000 cycles. Comparing the processed HPT samples with full scale test rig sample is something that was not done in previous work.

Comparing between the test approaches, it can be seen that the deformed layer in the FSR tests is similar in terms of hardness and microstructure, but of course it must be noted that the strain/hardness varies through the FSR specimen getting harder moving from the bulk to the surface. This is why this kind of approach is not the best for generating a deformed layer for manufacturing FCG specimens.

Rail Grade	R260	R350HT	R400HT
HPT Micro hardness (avg. in deformed layer) (Hv)	408	493	499
FSR Micro Hardness Deformed Layer (near rail surface) (Hv) (Yildirimli et al., 2024; Yang et al., 2024)	395	461	525
HPT Deformed layer Thickness (mm)	0.81	0.93	0.93
FSR Deformed layer Thickness (mm) (Yang et al., 2024)	1.0	0.8	0.75
HPT Microstructure	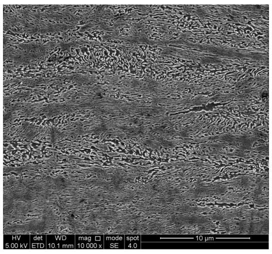	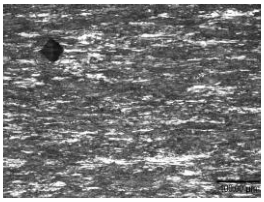 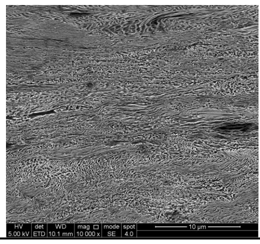	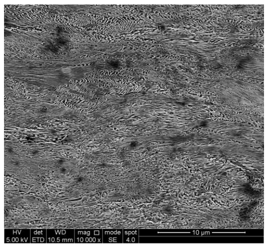

FSR Microstructure (Yildirimli et al., 2024; Yang et al., 2024)		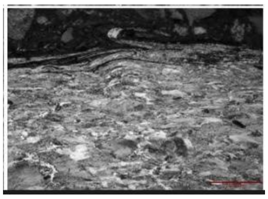	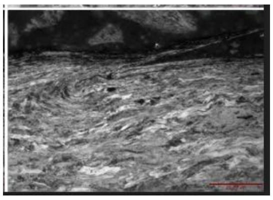
HPT test (Leitner et al., 2017)	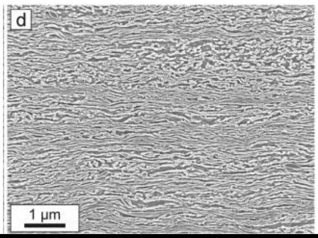		

Figure 105: HPT and full-scale rig (5,000 cycles)

6 FATIGUE CRACK SPECIMEN

The next part of the process was to design a fatigue crack growth (FCG) sample (see Figure 103) that could be manufactured from the HPT sample. Again it was a case of trial and error and the following dimensions were arrived at after following ASTM E647 requirement as closely as possible.

Previous work used a dimension of 1.3mm thickness, and a width, W, of 5.4mm (Leitner *et al.*, 2018). Maintaining the thickness of 1.3mm was also influenced by the potential fracture toughness gradient present in the deformed layer. It is evident that the hardness and therefore the fracture toughness drops the further you move away from the centre (see Figure 106(a)). As a result of this, it had to be as thin as possible. The difference in fracture toughness from one side of the specimen to the other could lead to different crack growth rate on either side of the specimen. Figure 106(b) is the final design of the FCG specimen with Figure 106(c) being what it was modelled from. The notch is different due to no available manufacturing method being available to create a V-notch as shown.

Previous work assumed the entire thickness of the HPT sample was involved in the strain calculation in addition to the fact that the location of the notch in relation to the actual deformed layer is not evident. Furthermore, there were no process data to confirm the effectiveness of the HPT process on the sample unlike the torque data available here.

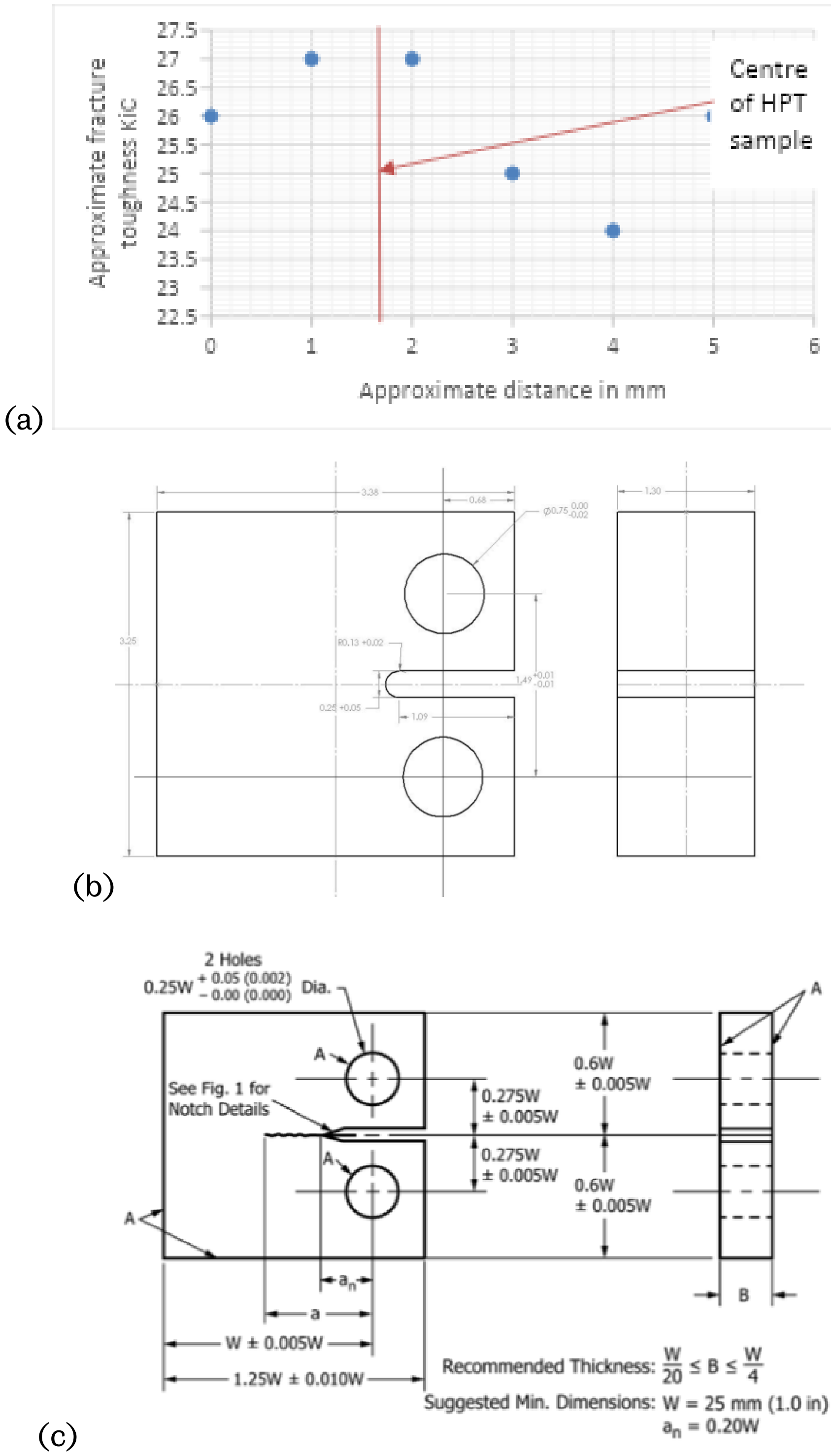

Figure 106: FCG specimens: (a) Estimated fracture toughness along deformed layer (b) Design for this project; (c) ASTM E647 FCG specimen criteria (ASTM, 1999)

The sample had to be taken from a specific location in the HPT disc (see Figure 107) due to its size which in turn dictated the number of revolutions needed to achieve the target strain of 6 as shown in the above calculations. Figure 107 shows the FCG specimen with the distance within the HPT sample.

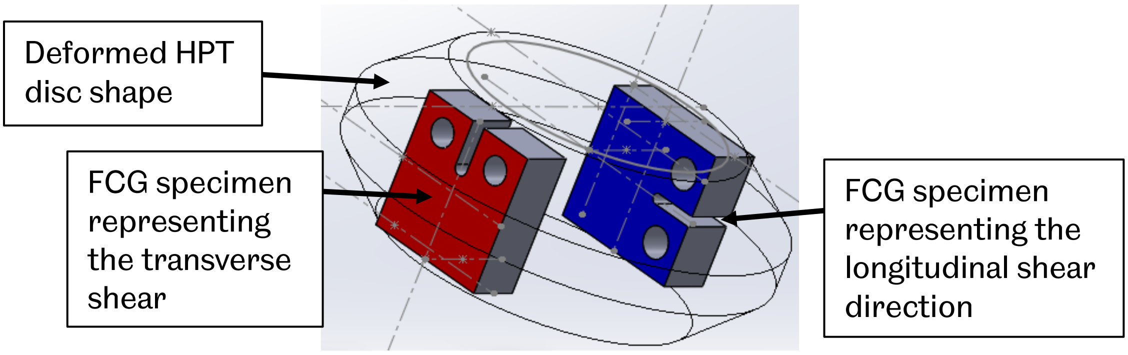

Figure 107: FCG specimen layout in the HPT disc

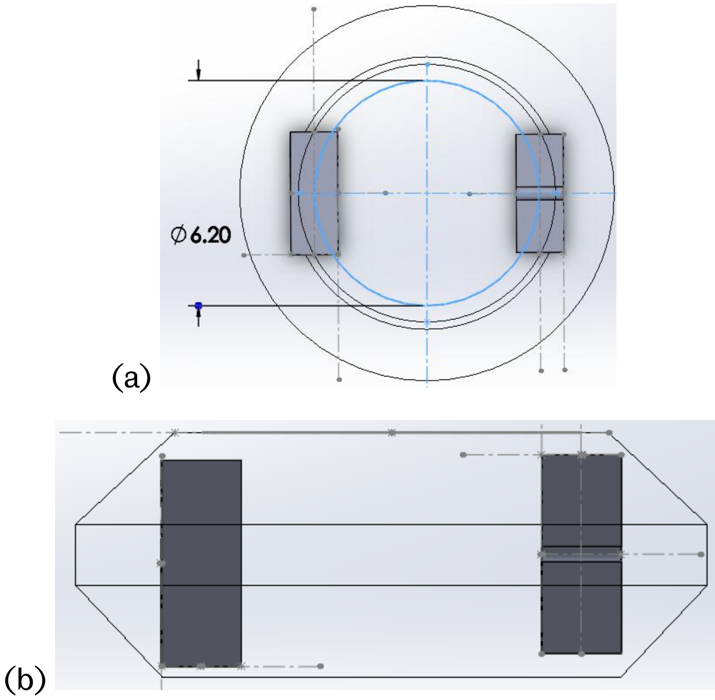

Figure 108: FCG specimen layout: (a) aerial view; (b) side view

Due to the size of the specimen, typical features of ASTM E647 cannot be met. One of these was the notch design on the FCG specimen. The specimen was required to have a notch with an angle of 120° and size of 0.167mm. However, due to the way the notch is to be made, which is by electric discharge wire cutting; the notch had feature associated with the wire used to make the notch. As a result, the width is going to be 0.25mm in thickness and a radius at the base of 0.125mm instead of the 120° originally intended. The FCG sample pieces were first cut out of the HPT sample and then the holes drilled into them before the notch was made.

6.1 Fatigue crack specimen grips and pins

Due to the extremely small specimen size, the grips had to be redesigned as the ones available were too big. The grip was designed in line with parameters stated in ASTM E647 Appendix A. The design and how it functions is shown in Figures 109 to 112. The FCG specimen will be placed in the clevis as shown in Figure 108a and a pin driven through to the holes in the FCG specimen and the clevis when they are aligned.

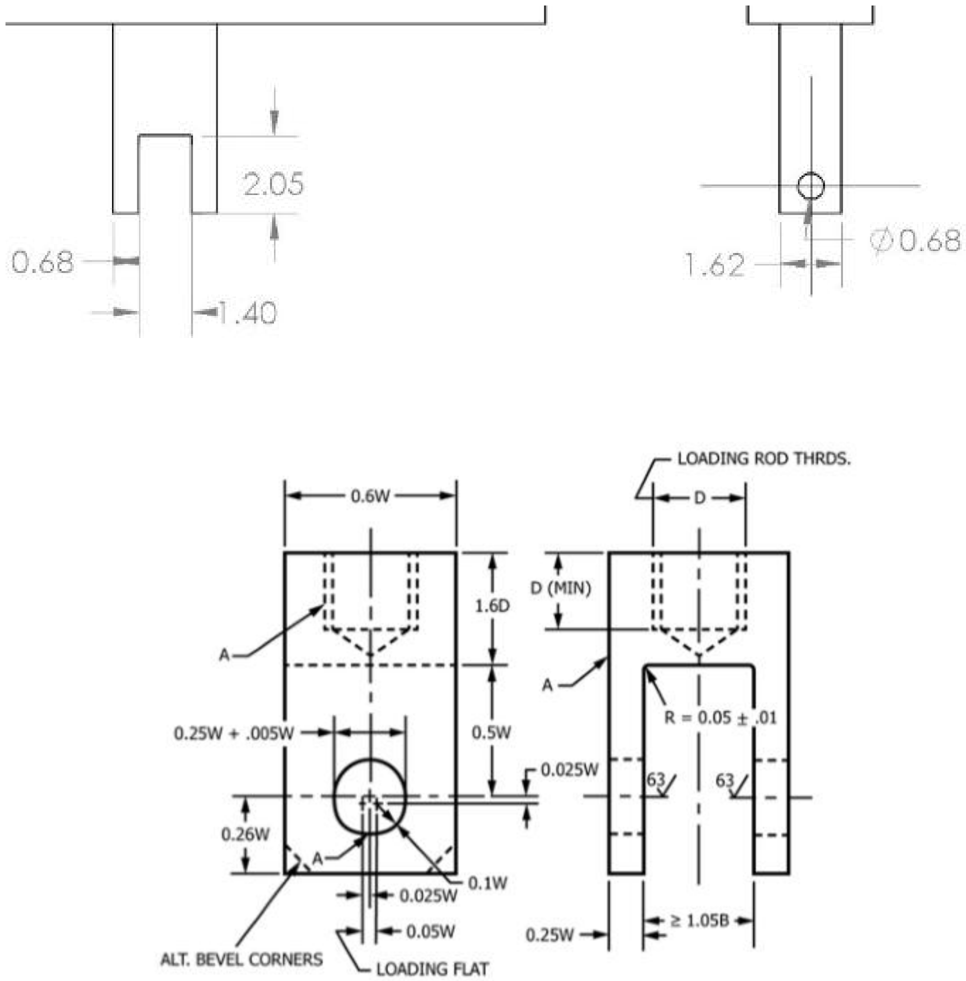

Figure 109: FCG specimen grip: (a) New design and (b) ASTM E647 derivative (ASTM, 1999)

The part going into the machine had to be designed to accommodate the adapter designed for the small specimen. This resulted in the design shown in Figure 110.

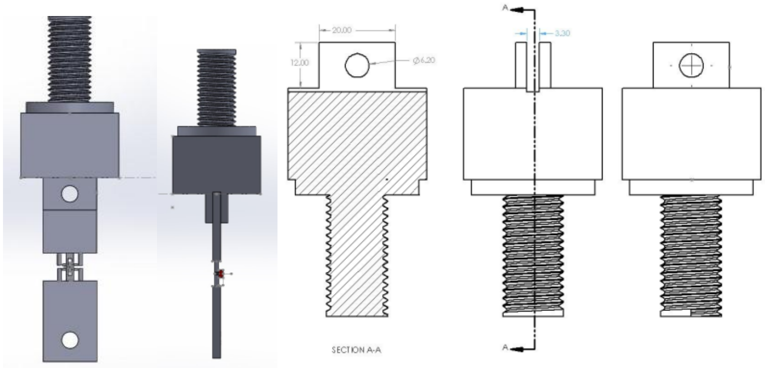

Figure 110: Connector to machine

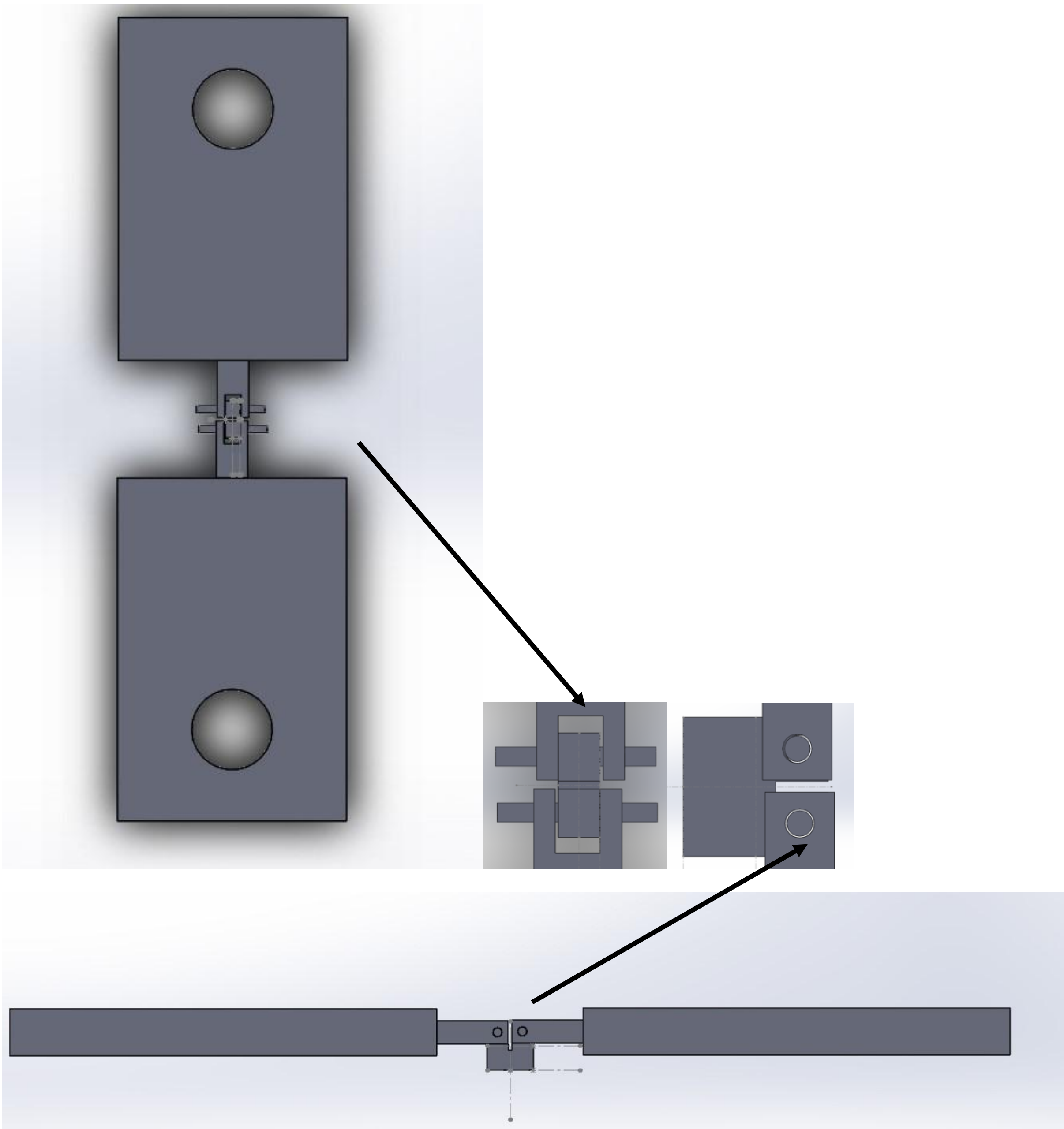

Figure 111: Adaptive Grip and FCG sample together

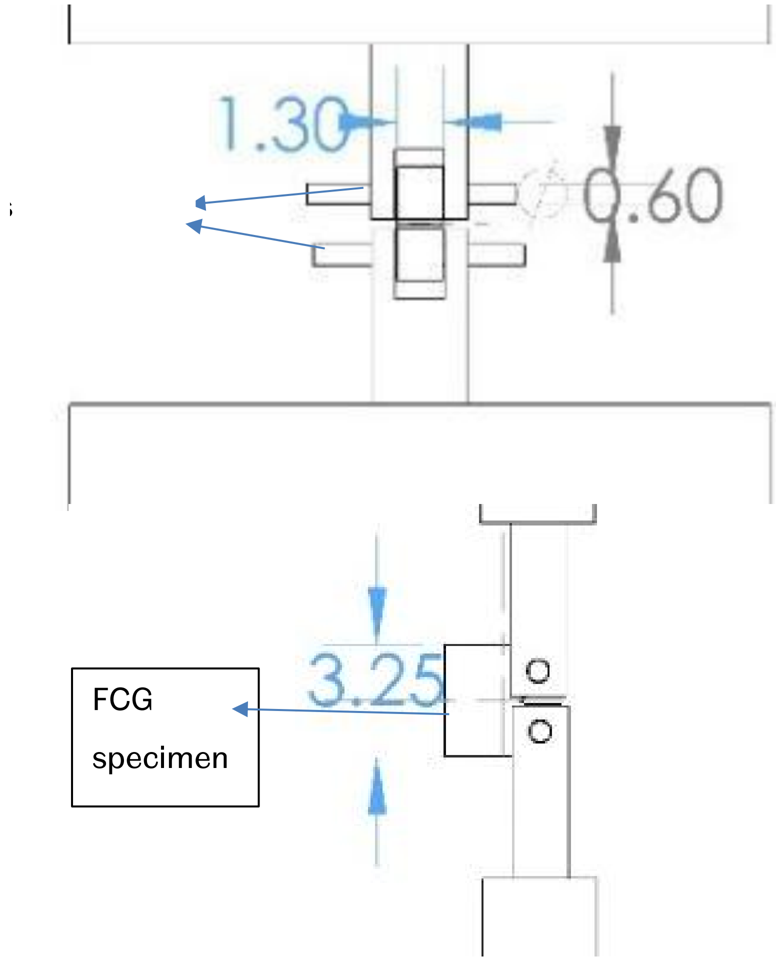

Figure 112: Initial FCG specimen, and FCG pin layout

The design shown in Figure 112 would be ideal if crack monitoring is to be done using the replica technique or other visual means alone. However, due to the anticipation of using the potential difference technique; the grips had to be able to accommodate the presence of the wires if needed. The diagram in Figure 113 shows where the wires should go on the specimen. As a result, the grip design shown in Figure 114 was also derived.

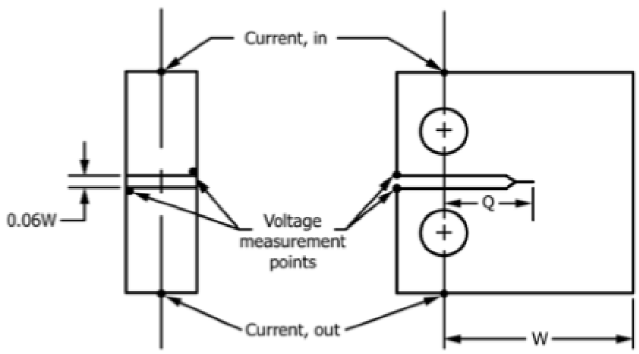

Figure 113: ASTM E647 Wire placement for crack monitoring (ASTM, 1999)

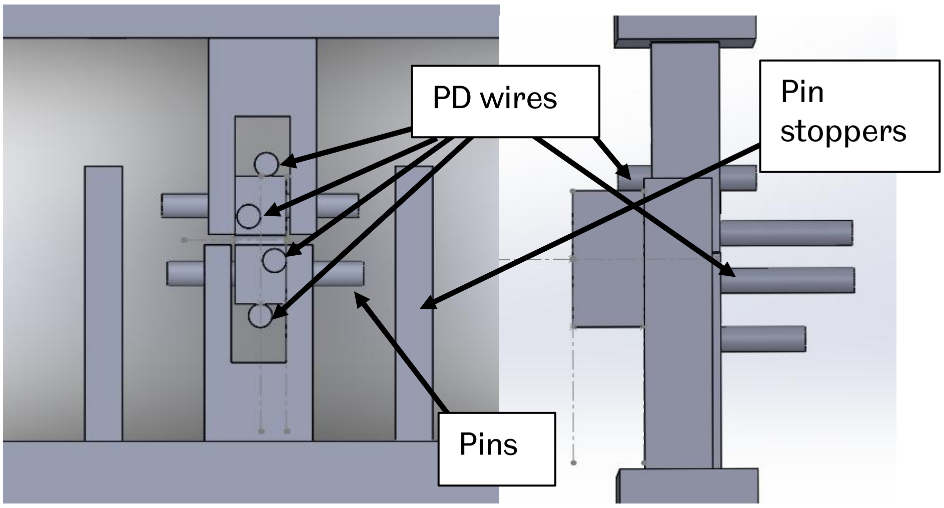

Figure 114: New layout with wires and pin stoppers

The pin had to be made from durable material that would not easily bend or fatigue due to the repetitive nature of the test. Fortunately, drill bits were of the correct size and could be bought and used as the pins for the experiment. These are made from high strength steel made to DIN 338.The rest of the grip was made from 4340 steel as recommended in ASTM E647, heat treated to 150Ksi (1034MPa minimum). Due to the tendency for the test for run for long periods of time, stoppers were also incorporated into the grip designs to stop the pins falling out during the test.

6.2 Crack monitoring

A major part of this experiment was monitoring the crack growth through the fatigue testing process. Previous work had done this by welding wires to the FCG sample and monitoring the potential difference as the crack grows. This is an approved method in accordance with ASTM E647. However, given how small the sample was, the welding process would have introduced heat into the sample which can result in significant grain refinement thereby affecting the crack propagation due to variation in grain size. As a result, the traveling microscope was selected to monitor the crack growth during the process. Although the grips were designed to accommodate the size of 0.6mm diameter wire for monitoring using the PD technique should the traveling microscope become unavailable.

6.3 Fatigue crack test procedure

A fatigue crack propagation test can be conducted with various methods according to ASTM E647 and involves two stages. The crack initiation and then the crack propagation test. The crack propagation can be conducted using the “K-increasing” or the “K-decreasing” technique (ASTM, 1999), where K is the stress intensity factor. This is basically starting with a high load being applied and gradually reducing it. This is due to the evident gradient in fracture toughness. A K increasing approach presents the strong possibility of pulling the sample part before testing since the crack is travelling into an ever reducing fracture toughness region. The presence of the fracture toughness gradient also makes it extremely difficult to model due to the crack always growing into a region of reducing fracture toughness and changing "C" and "m" constants due to the changing strain along the length of the specimen.

However, the crack initiation would be done using the decreasing K procedure. This is where a load is cyclically applied to the specimen at a high stress intensity and then reduced with each step. However, due to the probability of brittle behaviour, this will be done in compression-compression only. This is a technique developed for testing brittle material (Petersen *et al.*, 1994). The load applied had to be estimated based on the fracture toughness of the material so that it was not exceeded. This approach along with the K-decreasing procedure ensures that the stress intensity at the crack tip does not exceed the assumed fracture toughness of the material.

While the fracture toughness of the R260 rail material has been reported to be as low as 4MPa√m at a strain level of 17 (Hohenwarter *et al.*, 2011), for the strain level being used in this work it was estimated to be about 38MPa√m for the transverse direction and about 28MPa√m for the longitudinal direction as estimated from Figure 115. This is based on the highest hardness result of 426Hv which was achieved in the deformed layer after performing the HPT process. The Paris equation was based on the assumption of the absence of a fracture toughness gradient. However, it is impossible to adjust due to the changing fracture toughness, so a single fracture toughness figure was assumed.

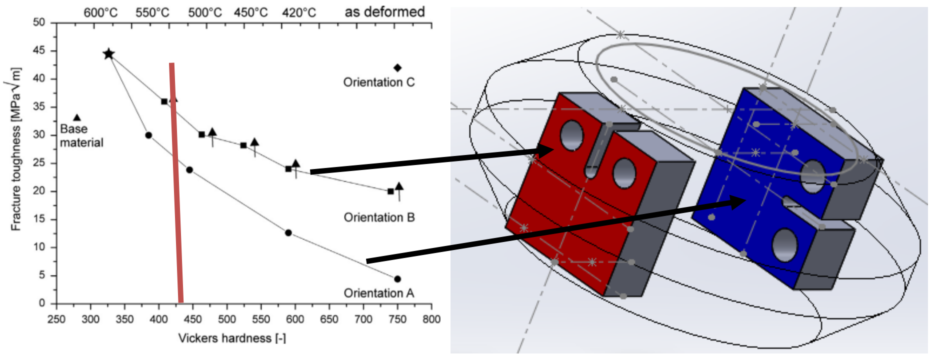

Figure 115: Proposed FCG specimen and the expected fracture toughness (Kammerhofer *et al.*, 2013)

The next step was to try and predict the manner in which the test would progress. This involved deriving the values "*C*" and "*m*" for the Paris equation from the graph shown in Figure 116 which resulted from pervious fatigue crack growth tests on a similar material with a similar hardness level (Leitner *et al.*, 2019)

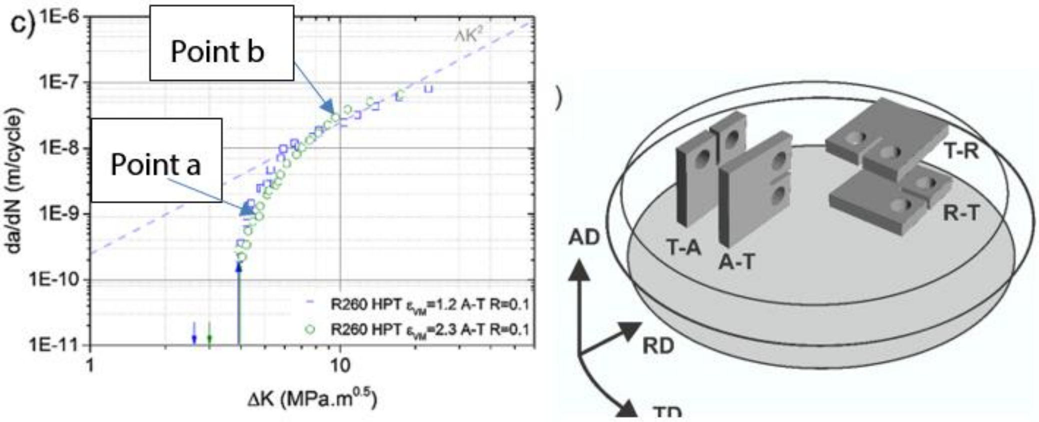

Figure 116: Crack growth data for R260 and FCG specimen layout (Leitner *et al.*, 2019)

From Figure 116 it was evident that the points of interest are orientation A-T and T-A as these represent the longitudinal and transverse direction in the shear plane therefore making them more relevant to this experiment. In addition to the fact that A-T was done at a strain more closely associated with the strain to be done in the experiment based on what was reported. As a result:

$$\frac{da}{dn} = C\Delta K^m$$

Point a: ΔK is 5MPa√m and $\frac{da}{dn}$ is 1x10^{-9}

Point b: ΔK is 10MPa√m and $\frac{da}{dn}$ is 4x10^{-8}

$$\left(\frac{da_{point\ a}}{dn_{point\ a}}\right) \div \left(\frac{da_{point\ b}}{dn_{point\ b}}\right) = \left(\frac{\Delta K_{point\ a}}{\Delta K_{point\ b}}\right)^m \qquad \text{Equation 19}$$

where:

$$m = \frac{log\ log\ (1 \times 10^{-9})\ -log\ log\ (4 \times 10^{-8})}{log\ log\ (5) - log(10)}$$

$$m = \frac{(-9) - (-7.3979)}{0.699 - 1}$$

$$m = \frac{-1.6021}{-0.301} = 5.323$$

$$m = 5.323$$

Substituting *m* into $C\Delta K^m$ for point "b" gives:

$$\frac{da}{dn} = C\Delta K^m$$

therefore $4 \times 10^{-8} = C(10)^{5.323}$

and $C = \frac{4\times10^{-8}}{10^{5.323}} = 1.90604 \times 10^{-13}$

The fatigue crack propagation test was intended to be carried out in specific crack length increments in accordance with ASTM E647. According to ASTM E647 the crack increment should be as follows:

$$\Delta a \leq 0.04W \; for \; 0.25 \leq \frac{a}{w} \leq 0.4$$

$$\Delta a \leq 0.02W \; for \; 0.40 \leq \frac{a}{W} \leq 0.6$$

$$\Delta a \leq 0.01W \; for \frac{a}{W} \leq 0.6$$

where "a" is the pre-crack length and "W" for the specimen is 2.7. This means (1/2.7mm) = 0.37. After some trial and error and due to the intended method of conducting the test, a planned crack increment of 0.025W was picked. The aim was to try and maximise the amount of data to be collected.

Table 8 shows the number of data points that can be collected for R = 0.1 in the longitudinal direction, where R is given by:

$$R = \frac{P_{min}}{P_{max}} or \frac{K_{min}}{K_{max}} \qquad \text{Equation 20}$$

Given the above parameters, this meant crack growth increments of 0.108mm. The ΔK value was then calculated in accordance with ASTM E647 using the following equations:

$$\Delta K = \frac{F\Delta P}{B\sqrt{W}} \qquad \text{Equation 21}$$

where F is the specimen geometry function:

$$F = \frac{\left(2+\frac{a}{w}\right)\left[0.886+4.64\left(\frac{a}{w}\right)-13.32\left(\frac{a}{w}\right)^2+14.72\left(\frac{a}{w}\right)^3-5.6\left(\frac{a}{w}\right)^4\right]}{(1-\frac{a}{w})^{3/2}} \qquad \text{Equation 10}$$

B is the thickness of the specimen; W is the distance from the centre of the grip to the end face of the FCG specimen and

ΔP is the difference between the minimum and maximum load in a cycle.

The stress intensity factor K after each cycle was also calculated to ensure it did not exceed the fracture toughness values as this would mean complete failure of the specimen:

$K = \frac{(F)P}{B\sqrt{W}}$ Equation 22

where P is the maximum load in the cycle.

Also the number of cycles needed to reach the required crack length was also calculated:

$\frac{da}{dn} = C\Delta K^m$ therefore $dn = \frac{da}{C\Delta K^m}$, integrating between the previous crack size (a_0) and the new crack size (a_f) gives:

$N_f = \frac{1}{C\int \quad (\frac{da}{\Delta K^m})}$ Equation 23

and since:

$\Delta K = F\Delta S\sqrt{\pi a}$ Equation 24

and:

$S_{max} = \frac{P_{max}(load)}{B\ (thickness\ of\ specimen)\times W(Withd)}$ Equation 25

$\Delta S = \ S_{max}(1 - R)$ Equation 26

where R is the ratio of the load or stress intensity factor per cycle as:

$R = \frac{P_{min}}{P_{max}}\, or\, \frac{K_{min}}{K_{max}}$ Equation 20

Therefore, $N_f = \frac{1}{C\int \quad (\frac{da}{F\Delta S\sqrt{\pi a}})}$ between the previous crack length a_0 and the new crack length a_f and therefore:

$N_f = \left(\frac{1}{\left(C\times F^m\times\Delta S^m\times\pi^{\frac{m}{2}}\right)}\right)\times ln\left(\frac{a_f}{a_0}\right)$ Equation 27

where a_0 is the crack size at the start of the cycle and a_f is the crack length after the cycle. Therefore, the time needed for the test to be done was:

Applying the above equations as well as crack growth increments in accordance with ASTM E647 led to the creation of Tables 7 to 9. These were done in the longitudinal direction as it is expected to be the direction with the worst fracture toughness (K_{IC}) as estimated in Figure 115 and limited data collection. The fracture toughness was assumed to be 38MPa√m in this case based on Figure 115 in the transverse direction and 28MPa√m in the longitudinal direction Figure 115.

Both the K-decreasing and K-increasing procedures were considered. The process applied below is the K-decreasing procedure for the second phase as this is seen to give more data points than the K-increasing procedure after trial and error. The K-decreasing technique involves using loads that produce a high stress intensity value of *K*, but not higher than the fracture toughness of the material at the start of the cycle. The load is then reduced by 10% when the cycle is completed. However, due to the size of the specimen and the loads, a reduction in 10% may not always be possible.

The yield strength was calculated using Equation 28 and then the figure generated was used to calculate the cyclic plastic zone associated with each hardness position in the deformed layer. The values ranged from about 583MPa to 639MPa, typical of literature values.

$$\sigma_{ys} = \frac{3\, H_v}{2} \qquad \text{Equation 28}$$

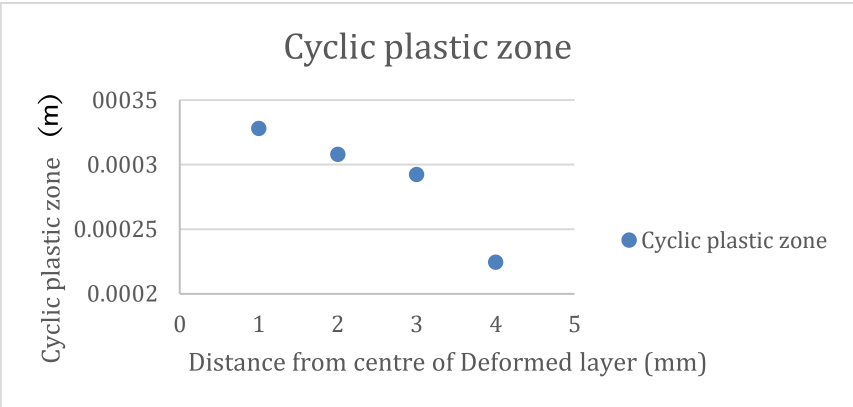

Figure 117: Cyclic plastic zone across the deformed layer

As expected, the cyclic plastic zone drops across the deformed layer due to the fracture toughness gradient present. Table 8 shows the proposed load and cycles in the longitudinal direction. Table 9 shows more data points due to the crack traveling across the longitudinal grains where there would be higher toughness. It is expected to lead to a deflected crack path. It is also expected that the crack would deflect since the shear plane in 90 degrees to the crack propagation.

An assumption of the load cell not being accurate below 0.5 N due to the high load range was considered when carrying out these calculations based on the advice of the supplier.

a (mm)	Pmin (N)	Pmax (N)	**ΔP**	F	**ΔK**	**K Max**	**Nf**
1.05	0.79	7.91	7.12	7.10	23.64	26	3848
1.11	0.71	7.12	6.40	7.48	22.43	25	4463
1.16	0.64	6.40	5.76	7.90	21.31	24	5166
1.22	0.58	5.76	5.19	8.35	20.27	23	5960
1.27	0.52	5.19	4.67	8.84	19.32	21	6846
1.32	0.57	**5.71**	5.14	9.38	22.55	25	3646
1.38	0.63	6.28	5.65	9.98	26.38	29	1927

Table 8: *R*=0.1 for K-decreasing approach for longitudinal direction

a (mm)	Pmin (N)	Pmax (N)	**ΔP**	F	**ΔK**	**K Max**	**Nf**
1.1	1.11	11.1	9.96	7.1	33.09	36.8	1071
1.1	1	9.96	8.97	7.48	31.4	34.9	1242
1.2	0.9	8.97	8.07	7.9	29.83	33.1	1437
1.2	0.81	8.07	7.26	8.35	28.38	31.5	1659
1.3	0.73	7.26	6.54	8.84	27.05	30.1	1905
1.3	0.65	6.54	5.88	9.38	25.83	28.7	2175
1.4	0.59	5.88	5.29	9.98	24.72	27.5	2466
1.4	0.65	6.47	5.82	10.6	29	32.2	1293
1.5	0.71	7.12	6.41	11.4	34.12	37.9	671
1.5	0.78	7.83	7.05	12.2	40.28	14.9	22280
1.6	0.86	8.61	7.75	13.2	47.73	17.7	11418
1.6	0.95	9.47	8.53	14.2	56.79	20.9	5829
1.7	1.04	10.4	9.38	15.5	67.88	24.7	2966
1.8	1.15	11.5	10.3	16.9	81.54	29.3	1504
1.8	1.26	12.6	11.3	18.5	98.51	34.8	761
1.9	1.39	13.9	12.5	20.5	119.7	41.3	384

Table 9: Data for transverse direction

The pre-crack would also be generated in accordance with the decreasing ΔK technique in compression. An alternative would be to introduce the pre-crack by using a razor blade or file the notch if possible. This was done in previous research (Leitner, Hohenwarter and Pippan, 2019). The K-decay pre-crack technique is the process of starting at a load which equates to a K_{max} value that is the same or just above the K_{IC} value of the material. This is then to be reduced 20% in accordance with ASTM E647 requirements after a fixed crack length is reached and then so on and so forth until the desired crack length of 1mm per E647 was reached. Due to the fracture toughness gradient in the deformed layer, the largest fracture toughness multiplied by 1.15 was assumed to be exceeded to initiate the crack. This is applied the compressive strength conversion to the fracture toughness. This is approximately 36.5 in the transverse direction and 31.05 in the longitudinal direction.

A (mm)	Pmin (N)	Pmax (N)	**ΔP**	**ΔK**	**K Max**	**N_f**
0.63	1.42	14.23	12.8	4.71	31	5837
0.72	1.14	11.38	10.2	5.17	28	8283
0.82	0.91	9.11	8.2	5.65	24	12131
0.91	0.73	7.29	6.56	6.17	21	18136
1	0.58	5.83	5.25	6.74	18	27424

Table 10: K-decreasing technique for pre-cracking cycle for longitudinal direction

A (mm)	Pmin (N)	Pmax (N)	**ΔP**	**ΔK**	**K Max**	**N_f**
0.63	1.68	16.76	15.1	33.28	37	3133
0.72	1.34	13.41	12.1	29.21	32	4447
0.82	1.07	10.73	9.65	25.55	28	6512
0.91	0.86	8.58	7.72	22.31	25	9736
1	0.69	6.86	6.18	19.48	22	14722

Table 11: K-decreasing technique for pre-cracking cycle for longitudinal direction

7 FATIGUE CRACK GROWTH EXPERIMENT

7.1 Introduction

This section outlines the planned experiment to show the fatigue crack propagation behaviour of R260 after undergoing severe plastic deformation to strain levels equivalent to the strain levels at the wheel-rail interface.

7.2 Fatigue crack growth specimen and grips

High pressure torsion samples were first generated as shown originally in Chapter 5 and FCG samples were cut and produced as shown in Chapter 4. Figure 118(a) shows the processed HPT specimen from above. The holes where the FCG specimens have been extracted are visible. Figure 119(b) shows one of the FCG specimens manufactured. The produced deformed layer in this case had a thickness of 0.77mm. Metallurgical analysis of the region of interest is shown in Figure 93. This gives a strain level of 7.6 at the planned target radius of 3.1mm when Equation 4 is applied.

(a)

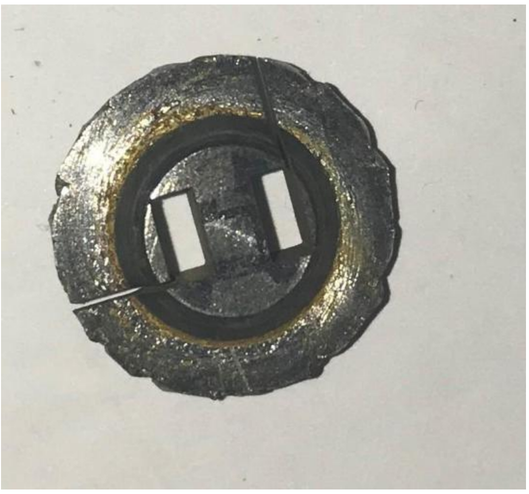

(b) 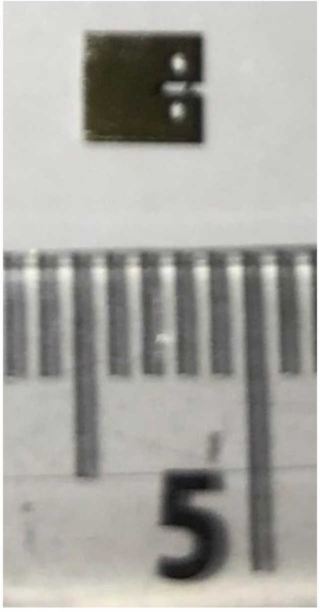

Figure 118: (a) Deformed HPT sample with FCG sample removed; (b) Machined FCG sample

The FCG specimens (see Figure 118(b)) were produced by first cutting blanks from the HPT sample. Holes were then drilled into the sample before the notch in the specimen was created using by electric discharge machining. The grips were also produced as designed in section 5.7 and shown in Figure 119.

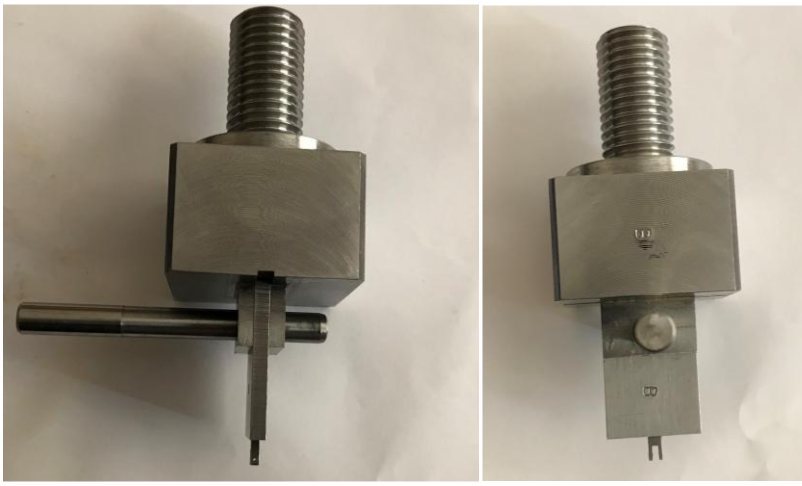

Figure 119: FCG specimen grip assembly

7.3 Fatigue crack growth testing

Due to the size of the FCG sample, an entirely new test machine had to be made. It involved modifying a shaker as shown in Figure 120.

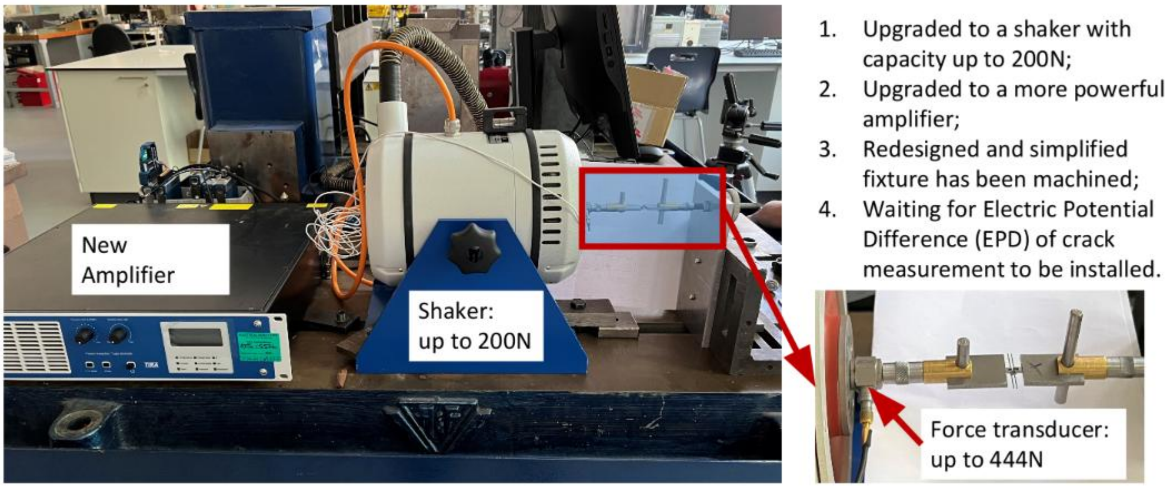

Figure 120: FCG testing machine set-up

The pre-crack cycles were originally performed as intended in the design section in tension-tension but resulted in no crack formed.

As a result of no crack forming, significantly higher loads were applied which then led to the specimen fracturing very quickly (see crack in Figure 121). A high definition camera attached to the FCG test up also showed flexing in the device thereby indicating not all the applied load was being transferred to the FCG sample.

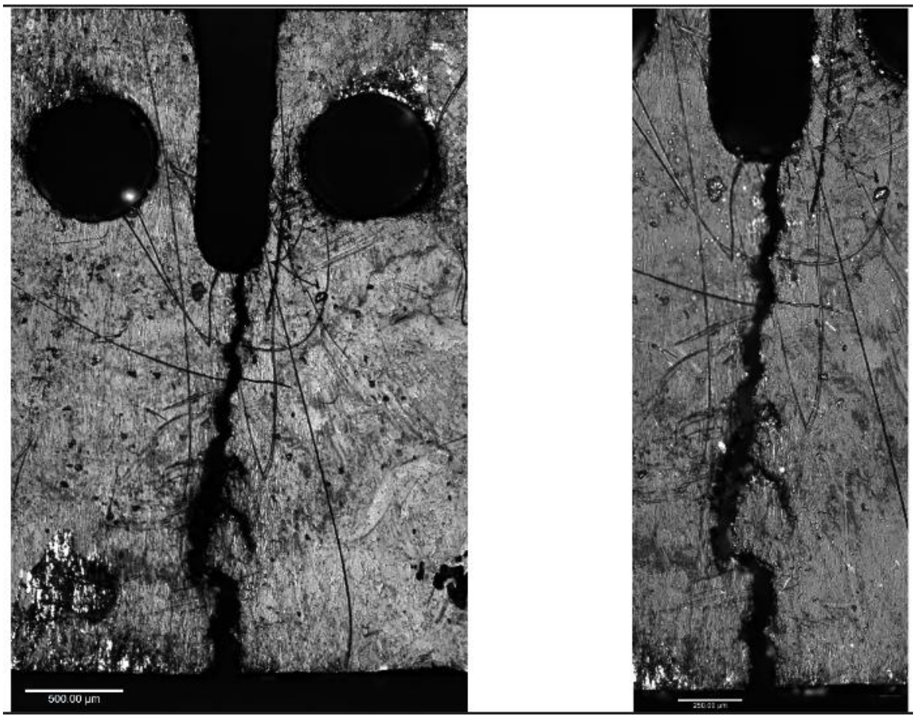

Figure 121: Image of fractured longitudinal samples

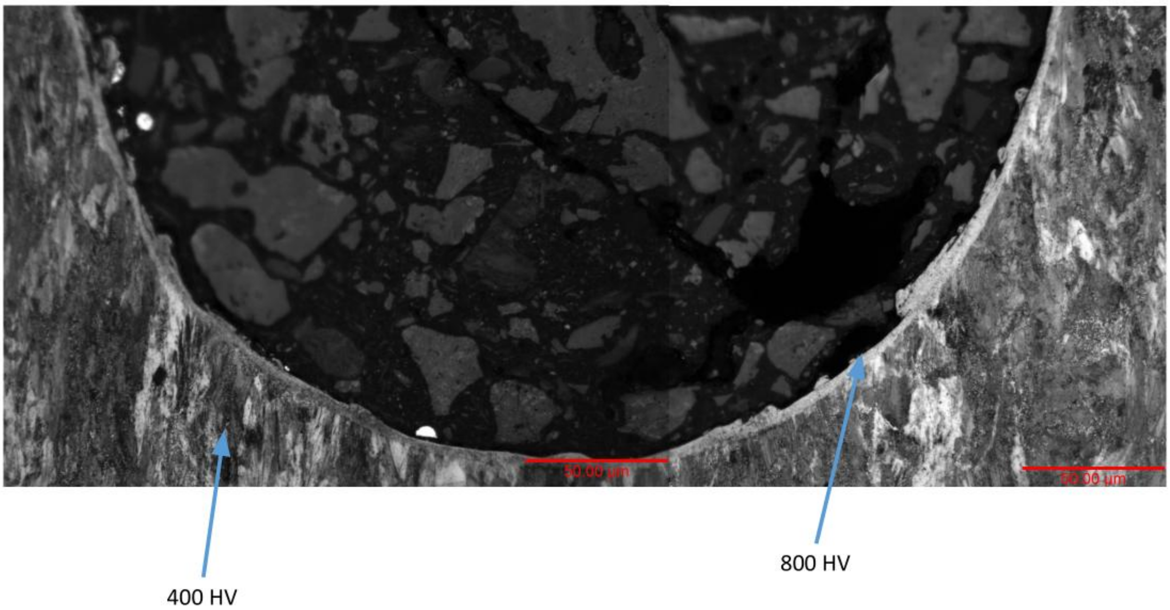

Figure 122: Hardness profile of Notch area on FCG sample

Hardness analysis of a FCG sample is shown in Figure 122. The high hardness recorded is an indication of martensite formation and can be put down to the electric discharge machining technique used to make the notch. This explains the difficulties in carrying out the test as planned. It is worth noting the shape of the crack path which is similar in shape to the fracture toughness along the length of the FCG sample. This is different to sample A-T in figure 123 which has a flat crack path. The flat crack path display is thereby indicating a crack propagation through a region that has not been severely deformed.

The difficulty associated with performing the FCG testing from modifying a shaker, flexing of the components during the test, to FCG sample production can be addressed by using larger FCG samples. This can only be produced from a larger HPT sample.

This cannot be achieved on the current test rig being used for the compression and rotation. However, the hardness measurements of the processed HPT specimens did indicate that the rotation may not be adding much strain to the specimen. If the deformed layer could be achieved in a satisfactory way using compression only this would open up the possibility of using a higher load capacity machine and therefore the processing of a larger initial specimen.

If the FCG test had been successful, it is expected to have behaved like the of A-T sample in Figure 123 due to the crack growing in the direction of lower fracture toughness from a region of higher fracture toughness.

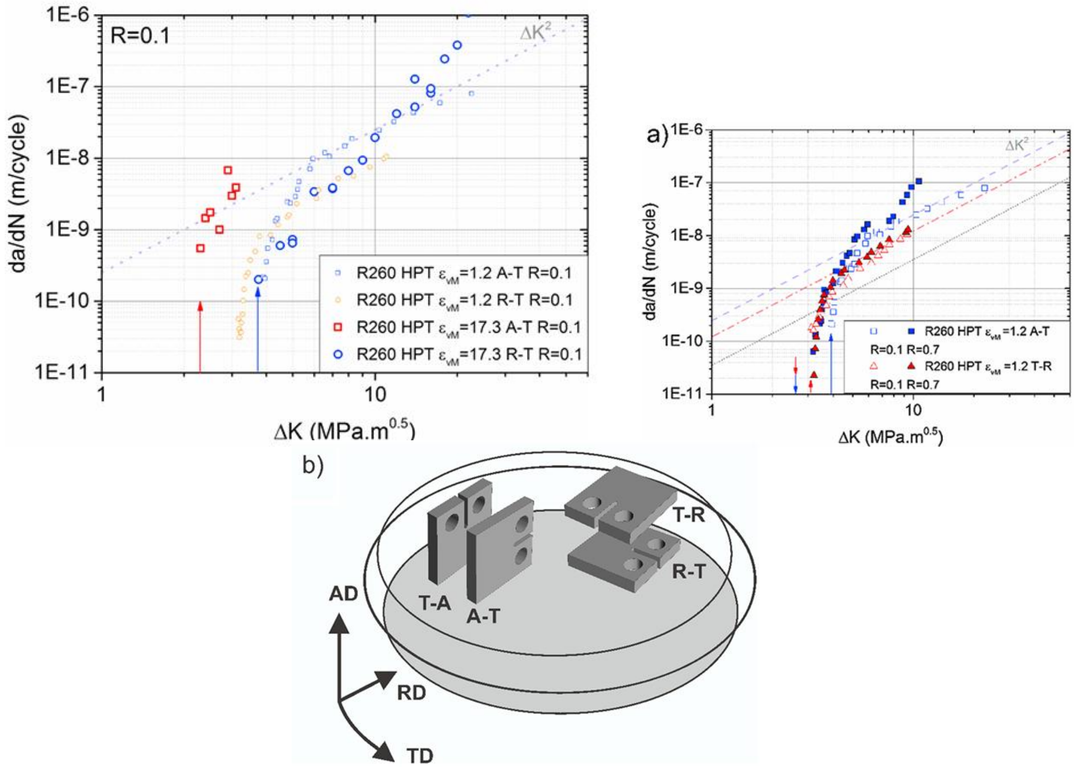

Figure 123: FCG results from previous research (Leitner, Hohenwarter and Pippan, 2019)

From the way the FCG samples were taken as shown in Figure 123, it could be seen as exploratory to try and find where the deformed layer is in the specimen created. The issue of anisotropy comes in when A-T and T-R clearly have two different rates even though they are in the same direction but different planes.

8 CONCLUSIONS

8.1 HPT/FCG Testing

Prior to embarking on the project, a thorough literature review was conducted. This helped to define the test approach and target microstructure of the deformed layer as well as the strain level to aim for.

As a result, an approach has been developed using a high pressure torsion test that enables the creation of an appropriate volume of deformed layer in rail (or wheel) material for subsequent FCG testing that is representative of that seen on the surface of rails and wheels in the field. Having a more controlled method for creating the layer is important and has been accomplished here through careful design of the anvil geometry and evidenced by the torque data uniquely collected in these tests. This has been achieved with a smaller specimen and lower load application than used in previous work.

The approach has been shown to work for a range of rail grades and the outcomes have been compared with full-scale tests using actual wheels and rails made from the same materials as well as representative contact loads/slips. The comparison revealed that the deformed layers were similar in both microstructure and hardness.

A method for extracting very small fatigue crack growth specimens has been created. Various test set-ups were trialled to test these, but it proved challenging to find an approach that allowed the small specimens to be tested at the conditions required and take measurements of the crack growth.

A new approach has been suggested that uses a larger specimen processed at a higher load. See the following section for more details.

8.2 Further Work

In order to enable FCG tests to be carried out at the conditions required, larger specimens are required whilst maintain a thickness that is as small as possible. This means that the initial specimens must be increased in size to give a larger deformed layer. This can only happen if a larger load capacity machine is identified. Such machines exist, but only for normal load application. A new machine has been identified for the cyclic loading of lager FCG specimens, but it has been out of use for seven years and is currently undergoing refurbishment. Once done though this would provide a solution to the issues with using the shaker test-rig.

Once the set-up for FCG testing is resolved there are many more variables that can be investigated.

REFERENCES

Agarwal, V. *et al.* (2014) ‘Fatigue crack propagation in a gear tooth in the presence of an inclusion’, *International Journal of Computational Methods in Engineering Science and Mechanics*, 15(3), pp. 247–252. doi: 10.1080/15502287.2014.882434.

Archard, J. F. (1986) ‘Friction between metal surfaces’, *Wear*, 113(1), pp. 3–16. doi: 10.1016/0043-1648(86)90052-9.

Arun Kumar, Pillai, U. T. S. and Srinivasan, A. (2019) ‘Processing Techniques to Develop Metallic Materials with Superior Mechanical Properties’, *Transactions of the Indian Institute of Metals*. Springer India, 72(10), pp. 2877–2891. doi: 10.1007/s12666-019-01764-3.

Asih, A. M. S., Ding, K. and Kapoor, A. (2012) ‘Modelling rail wear transition and mechanism due to frictional heating’, *Wear*. Elsevier B.V., 284–285, pp. 82–90. doi: 10.1016/j.wear.2012.02.017.

Asm committee (1996) ‘Fracture mechanics properties of carbon and alloy steel’, in Asm committee (ed.) *Asm handbook*. VOLUME 19, pp. 614–654. Available at: www.asminternational.org.

ASTM (1999) ‘E647-00’, 03, pp. 1–43. doi: 10.1520/E0647-15.2.

ASTM committee E08 (2019) *Standard test method for Linear-elastic plane-strain fracture toughness K_{Ic} of Metallic materials-E399*. E399-19th edn. Astm international.

Barbangelo, A. (1985) ‘Influence of non-metallic inclusions on fatigue crack growth in a structural steel’, *Journal of Materials Science*, 20(6), pp. 2087–2092. doi: 10.1007/BF01112291.

Barsom, J. and Rolfe, S. (1999) *Fracture and Fatigue Control in Structures: Applications of Fracture Mechanics, Third Edition*, *Fracture and Fatigue Control in Structures: Applications of Fracture Mechanics, Third Edition*. doi: 10.1520/mnl41-3rd-eb.

Beaty, P. *et al.* (2016) ‘Experimental modelling of lipping in insulated rail joints and investigation of rail head material improvements’, *Proceedings of the Institution of Mechanical Engineers, Part F: Journal of Rail and Rapid Transit*, 230(4), pp. 1375–1387. doi: 10.1177/0954409715600740.

Becker, W. T. (2018) ‘Fracture Appearance and Mechanisms of Deformation and Fracture’, *Failure Analysis and Prevention*, 11(Ref 3), pp. 559–586. doi: 10.31399/asm.hb.v11.a0003537.

Becker, W. T. *et al.* (2018) ‘Mechanisms and Appearances of Ductile and Brittle Fracture in Metals’, *Failure Analysis and Prevention*, 11, pp. 587–626. doi: 10.31399/asm.hb.v11.a0003538.

Bernsteiner, C. *et al.* (2016) ‘Development of white etching layers on rails: simulations and experiments’, *Wear*. Elsevier, 366–367, pp. 116–122. doi: 10.1016/j.wear.2016.03.028.

Bevan, A. *et al.* (2020) 'Judicious selection of available rail steels to reduce life-cycle costs', *Proceedings of the Institution of Mechanical Engineers, Part F: Journal of Rail and Rapid Transit*, 234(3), pp. 257–275. doi: 10.1177/0954409718802639.

BSI Group (2011) 'BSI Standards Publication Railway applications — Track — Rail'.

Carrel.J (2019) 'MEC446 Fundamentals and Applications of Tribology', *Friction*.

Chatterjee, S., Gadad, S. S. and Kundu, T. K. (2010) 'Atomic force microscopy', *Resonance*, 15(7), pp. 622–642. doi: 10.1007/s12045-010-0047-z.

Christoforou, P. *et al.* (2018) 'Benchmarking of premium rail material wear', *Proceedings of the 11th International Conference on Contact Mechanics and Wear of Rail/wheel Systems, CM 2018*. Elsevier B.V., 436–437(January), pp. 172–180. doi: 10.1016/j.wear.2019.202990.

Cyril, N. S. and Fatemi, A. (2009) 'Experimental evaluation and modelling of sulfur content and anisotropy of sulfide inclusions on fatigue behaviour of steels', *International Journal of Fatigue*. Elsevier Ltd, 31(3), pp. 526–537. doi: 10.1016/j.ijfatigue.2008.04.001.

Daves, W., Kráčalík, M. and Scheriau, S. (2019) 'Analysis of crack growth under rolling-sliding contact', *International Journal of Fatigue*, 121(December 2018), pp. 63–72. doi: 10.1016/j.ijfatigue.2018.12.006.

Dowling, Norman E, Siva Prasad, Katakam Narayanasamy, R. (2013) *Mechanical Behaviour of Materials.Engineering methods for deformation, fracture and fatigue.* Fourth Edi. Pearson Eduction limited.

Dwyer-Joyce, R. S. *et al.* (2009) 'Feasibility study for real time measurement of wheel-rail contact using an ultrasonic array', *Journal of Tribology*, 131(4), pp. 1–9. doi: 10.1115/1.3176992.

Edalati, K. and Horita, Z. (2016) 'A review on high-pressure torsion (HPT) from 1935 to 1988', *Materials Science and Engineering A*. Elsevier, 652, pp. 325–352. doi: 10.1016/j.msea.2015.11.074.

Edalati, K., Horita, Z. and Langdon, T. G. (2009) 'The significance of slippage in processing by high-pressure torsion', *Scripta Materialia*. Acta Materialia Inc., 60(1), pp. 9–12. doi: 10.1016/j.scriptamat.2008.08.042.

Ekberg, A. and Sotkovszki, P. (2001) 'Anisotropy and rolling contact fatigue of railway wheels', *International Journal of Fatigue*, 23(1), pp. 29–43. doi: 10.1016/S0142-1123(00)00070-0.

Fegredo, D. M. *et al.* (1988) 'The effect of sulphide and oxide inclusions on the wear rates of a standard C-Mn and a Cr-Mo alloy rail steel', *Wear*, 126(3), pp. 285–306. doi: 10.1016/0043-1648(88)90171-8.

Figueiredo, R. B. *et al.* (2012) 'Analysis of plastic flow during high-pressure torsion', *Journal of Materials Science*, 47(22), pp. 7807–7814. doi: 10.1007/s10853-012-6506-z.

Fletcher, D. (2019a) 'MEC448 - Railway engineering and sustainable transport Lecture 4 Wheel-rail contact mechanics Wheel-rail contact', pp. 1–17.

Fletcher, D. (2019b) 'MEC448 - Railway engineering and sustainable transport Lecture 6 Wear of wheels and rails', pp. 1–17.

Fletcher, D. I. and Lewis, S. (2013) 'Creep curve measurement to support wear and adhesion modelling, using a continuously variable creep twin disc machine', *Wear*. Elsevier, 298–299(1), pp. 57–65. doi: 10.1016/j.wear.2012.11.065.

Freisinger, M. *et al.* (2023) 'In-situ micro-cantilever bending studies of a white etching layer thermally induced on rail wheels', *Materials Science and Engineering: A*. Elsevier B.V., 869(February), p. 144805. doi: 10.1016/j.msea.2023.144805.

Furukawa, M. *et al.* (1998) 'The shearing characteristics associated with equal-channel angular pressing', *Materials Science and Engineering A*, 257(2), pp. 328–332. doi: 10.1016/S0921-5093(98)00750-3.

Gallardo-Hernandez, E.A., Lewis, R. (2008) 'Twin Disc Assessment of Wheel/Rail Adhesion', *Wear*, 265, pp. 1309-1316.

Garnham, J. E. and Davis, C. L. (2008) 'The role of deformed rail microstructure on rolling contact fatigue initiation', *Wear*, 265(9–10), pp. 1363–1372. doi: 10.1016/j.wear.2008.02.042.

Garnham, J. E. and Davis, C. L. (2011) 'Very early stage rolling contact fatigue crack growth in pearlitic rail steels', *Wear*. Elsevier B.V., 271(1–2), pp. 100–112. doi: 10.1016/j.wear.2010.10.004.

Hardwick, C., Lewis, R. and Stock, R. (2017) 'The effects of friction management materials on rail with pre-existing RCF surface damage', *Wear*. Elsevier B.V., 384–385(November 2016), pp. 50–60. doi: 10.1016/j.wear.2017.04.016.

Harmon, M. and Lewis, R. (2016) 'Review of top of rail friction modifier tribology', *Tribology - Materials, Surfaces and Interfaces*. Taylor & Francis, 10(3), pp. 150–162. doi: 10.1080/17515831.2016.1216265.

Hashimoto, K. *et al.* (2012) 'Effect of sulphide inclusions on rolling contact fatigue life of bearing steels', *Materials Science and Technology*, 28(1), pp. 39–43. doi: 10.1179/1743284711Y.0000000062.

He, C. G. *et al.* (2016) 'Experimental investigation on the effect of operating speeds on wear and rolling contact fatigue damage of wheel materials', *Wear*, 364–365, pp. 257–269. doi: 10.1016/j.wear.2016.08.006.

Hohenwarter, A. *et al.* (2011) 'Effect of large shear deformations on the fracture behaviour of a fully pearlitic steel', *Metallurgical and Materials Transactions A: Physical Metallurgy and Materials Science*, 42(6), pp. 1609–1618. doi: 10.1007/s11661-010-0541-7.

Hohenwarter, A. and Pippan, R. (2019) 'Sample Size and Strain-Rate-Sensitivity Effects on the Homogeneity of High-Pressure Torsion Deformed Disks', *Metallurgical and Materials Transactions A: Physical Metallurgy and*

Materials Science. Springer US, 50(2), pp. 601–608. doi: 10.1007/s11661-018-4989-1.

Jenkins, M. (2018) 'Fracture Resistance Testing of Brittle Solids', *Mechanical Testing and Evaluation*, 8(Eq 2), pp. 665–678. doi: 10.31399/asm.hb.v08.a0003312.

Johnson, K. L. (1989) 'The strength of surfaces in rolling contact', *Proceedings of the Institution of Mechanical Engineers, Part C: Journal of Mechanical Engineering Science*, 203(3), pp. 151–163. doi: 10.1243/PIME_PROC_1989_203_100_02.

Kammerhofer, C. *et al.* (2013) 'Influence of morphology and structural size on the fracture behaviour of a nanostructured pearlitic steel', *Materials Science and Engineering A*. Elsevier, 585, pp. 190–196. doi: 10.1016/j.msea.2013.07.032.

Kapoor, A;Fletcher, D.I; Franklin, F. . (2003) 'The role of wear in enhancing rail life', in *Proceeding of the 29th Leeds-Lyon Symposium on Tribology*, p. Pg 331-340.

Kapp, M. W. *et al.* (2016) 'Anisotropic deformation characteristics of an ultrafine- and nanolamellar pearlitic steel', *Acta Materialia*. Elsevier Ltd, 106, pp. 239–248. doi: 10.1016/j.actamat.2015.12.037.

Kim, J. G. *et al.* (2017) 'Effect of initial grain size on the microstructure and mechanical properties of high-pressure torsion processed twinning-induced plasticity steels', *Materials Science and Engineering A*. Elsevier, 682(October 2016), pp. 164–167. doi: 10.1016/j.msea.2016.11.050.

Kuhn, H. and Medlin, D. (2018) 'Fracture Toughness and Fracture Mechanics', *Mechanical Testing and Evaluation*, 8, pp. 563–575. doi: 10.31399/asm.hb.v08.a0003305.

Larijani, N. *et al.* (2014) 'The effect of anisotropy on crack propagation in pearlitic rail steel', *Wear*. Elsevier, 314(1–2), pp. 57–68. doi: 10.1016/j.wear.2013.11.034.

Larijani, N., Kammerhofer, C. and Ekh, M. (2015) 'Simulation of high pressure torsion tests of pearlitic steel', *Journal of Materials Processing Technology*. Elsevier B.V., 223, pp. 337–343. doi: 10.1016/j.jmatprotec.2015.04.018.

Lee, D. J. and Kim, H. S. (2014) 'Finite element analysis for the geometry effect on strain inhomogeneity during high-pressure torsion', *Journal of Materials Science*, 49(19), pp. 6620–6628. doi: 10.1007/s10853-014-8283-3.

Lee, K. M. and Polycarpou, A. A. (2005) 'Wear of conventional pearlitic and improved bainitic rail steels', *Wear*, 259(1–6), pp. 391–399. doi: 10.1016/j.wear.2005.02.058.

Leitner, T. (2017) *Fatigue crack growth of nanocrystalline and ultrafine grained metal processed by severe plastic deformation*. University of Leoben.

Leitner, T. *et al.* (2018) 'Influence of severe plastic deformation and specimen orientation on the fatigue crack propagation behaviour of a pearlitic steel', *Materials Science and Engineering A*. Elsevier B.V., 710(October 2017), pp. 260–270. doi: 10.1016/j.msea.2017.10.040.

Leitner, T., Hohenwarter, A. and Pippan, R. (2019) 'Anisotropy in fracture and fatigue resistance of pearlitic steels and its effect on the crack path', *International Journal of Fatigue*. Elsevier, 124(December 2018), pp. 528–536. doi: 10.1016/j.ijfatigue.2019.02.048.

Lewis, R; Dwyer-Joyce, R. S. (2004) 'Wear mechanisms and transition in railway wheel steel', 218, pp. 467–468. doi: 10.1258/itt.2010.100803.

Lewis, R. (2006) 'Wear at the wheel / rail interface when sanding is used to increase adhesion', 220, pp. 29–41. doi: 10.1243/095440905X33260.

Lewis, R. *et al.* (2010) 'Mapping railway wheel material wear mechanisms and transitions', *Proceedings of the Institution of Mechanical Engineers, Part F: Journal of Rail and Rapid Transit*, 224(3), pp. 125–137. doi: 10.1243/09544097JRRT328.

Lewis, R. and Olofsson, U. (2009) *Wheel-rail interface handbook*. woodhead publishing limited.

Lewis, S. R. *et al.* (2016) 'Improving rail wear and RCF performance using laser cladding', *Wear*. Elsevier, 366–367, pp. 268–278. doi: 10.1016/j.wear.2016.05.011.

Liu, J. *et al.* (2016) 'Effects of rail materials and axle loads on the wear behaviour of wheel/rail steels', *Advances in Mechanical Engineering*, 8(7), pp. 1–12. doi: 10.1177/1687814016657254.

Lowe, T. C. and Valiev, R. Z. (2004) 'The use of severe plastic deformation techniques in grain refinement', *Jom*, 56(10), pp. 64–68. doi: 10.1007/s11837-004-0295-z.

Lu, P. *et al.* (2019) 'Laser cladding of rail ; the effects of depositing material on lower rail grades', 439(January). doi: 10.1016/j.wear.2019.203045.

Masoumi, M. *et al.* (2018) 'Role of crystallographic orientation and grain boundaries in fatigue crack propagation in used pearlitic rail steel', *Materials Science and Engineering A*. Elsevier B.V., 722(January), pp. 147–155. doi: 10.1016/j.msea.2018.03.028.

Matsumoto, A. *et al.* (2002) 'Creep force characteristics between rail and wheel on scaled model', *Wear*, 253(1–2), pp. 199–203. doi: 10.1016/S0043-1648(02)00100-X.

Maya-Johnson, S., Felipe Santa, J. and Toro, A. (2017) 'Dry and lubricated wear of rail steel under rolling contact fatigue - Wear mechanisms and crack growth', *Wear*. Elsevier B.V., 380–381, pp. 240–250. doi: 10.1016/j.wear.2017.03.025.

Maya-Johnson, S., Ramirez, A. J. and Toro, A. (2015) 'Fatigue crack growth rate of two pearlitic rail steels', *Engineering Fracture Mechanics*. Elsevier Ltd, 138, pp. 63–72. doi: 10.1016/j.engfracmech.2015.03.023.

Messaadi, M., Oomen, M. and Kumar, A. (2019) 'Friction modifiers effects on tribological behaviour of bainitic rail steels', *Tribology International*, 140(March). doi: 10.1016/j.triboint.2019.105857.

Meyer, K. A., Nikas, D. and Ahlström, J. (2018) 'Microstructure and mechanical properties of the running band in a pearlitic rail steel: Comparison between biaxially deformed steel and field samples', *Wear*. Elsevier B.V., 396–397(August 2017), pp. 12–21. doi: 10.1016/j.wear.2017.11.003.

Mitchell, M. R. (2018) 'Fundamentals of Modern Fatigue Analysis for Design', *Fatigue and Fracture*, 19, pp. 227–249. doi: 10.31399/asm.hb.v19.a0002364.

Nikas, D., Zhang, X. and Ahlström, J. (2018) 'Evaluation of local strength via microstructural quantification in a pearlitic rail steel deformed by simultaneous compression and torsion', *Materials Science and Engineering A*. Elsevier B.V., 737(August), pp. 341–347. doi: 10.1016/j.msea.2018.09.067.

Olofsson, U. *et al.* (2013) 'Tribology of the wheel-rail contact-aspects of wear, particle emission and adhesion', *Vehicle System Dynamics*, 51(7), pp. 1091–1120. doi: 10.1080/00423114.2013.800215.

Peixoto, D. and Ferreira, L. A. (2013) 'Fatigue crack propagation behaviour in railway steels', *International Journal of Structural Integrity*, 4(4), pp. 487–500. doi: 10.1108/IJSI-10-2012-0029.

Petersen, D. *et al.* (1994) 'The Use of Fatigue Specimens Pre-cracked in Compression for Measuring Threshold Values and Crack Growth', *Journal of Testing and Evaluation*, 22(2), p. 98. doi: 10.1520/jte12641j.

Petersen, D. *et al.* (2000) 'Development of a Machine for Closely Controlled Rolling Contact Fatigue and Wear Testing', *Journal of Testing and Evaluation*, 28(4), p. 267. doi: 10.1520/jte12104j.

Pippan, R. *et al.* (2010) 'Saturation of Fragmentation During Severe Plastic Deformation', *Annual Review of Materials Research*, 40(1), pp. 319–343. doi: 10.1146/annurev-matsci-070909-104445.

Pletincx, S. (2014) 'Study of the encapsulation of healing agents for autonomous self-healing coatings .', (October).

Pointner, P. (2008) 'High strength rail steels-The importance of material properties in contact mechanics problems', in *Wear*, pp. 1373–1379. doi: 10.1016/j.wear.2008.03.015.

Ponter, A. R. S., Hearle, A. D. and Johnson, K. L. (1985) 'Application of the kinematical shakedown theorem to rolling and sliding point contacts', *Journal of the Mechanics and Physics of Solids*, 33(4), pp. 339–362. doi: 10.1016/0022-5096(85)90033-X.

Roodposhti, P. S. *et al.* (2015) 'Microstructural approach to equal channel angular processing of commercially pure titanium - A review', *Transactions of Nonferrous Metals Society of China (English Edition)*. The Nonferrous Metals Society of China, 25(5), pp. 1353–1366. doi: 10.1016/S1003-6326(15)63734-7.

Sakai, G. *et al.* (2005) 'Developing high-pressure torsion for use with bulk samples', *Materials Science and Engineering A*, 406(1–2), pp. 268–273. doi: 10.1016/j.msea.2005.06.049.

Scheriau, S. and Pippan, R. (2008) 'Severe Plastic Deformation of Steels', *BHM Berg- und Hüttenmännische Monatshefte*, 153, pp. 242–246.

Schilke, M., Larijani, N. and Persson, C. (2014) 'Interaction between cracks and microstructure in three dimensions for rolling contact fatigue in railway rails', *Fatigue and Fracture of Engineering Materials and Structures*, 37(3), pp. 280–289. doi: 10.1111/ffe.12112.

Six, K. *et al.* (2020) 'Rolling contact fatigue behaviour of rails: Wedge model predictions in T-Gamma world', *Proceedings of the Institution of Mechanical Engineers, Part F: Journal of Rail and Rapid Transit*, 234(10), pp. 1335–1345. doi: 10.1177/0954409719896941.

Stock, R. *et al.* (2011) 'Influencing rolling contact fatigue through top of rail friction modifier application - A full scale wheel-rail test rig study', *Wear*. Elsevier B.V., 271(1–2), pp. 134–142. doi: 10.1016/j.wear.2010.10.006.

Stock, R. and Pippan, R. (2014) 'Rail grade dependent damage behaviour - Characteristics and damage formation hypothesis', *Wear*. Elsevier, 314(1–2), pp. 44–50. doi: 10.1016/j.wear.2013.11.029.

Tournay.H. (2001) *'Supporting technologies vehicle track interaction',in guidelines to best practise for heavy haul railway operations:Wheel and rail interface Issues,international heavy haul association*. Virginia.

Trummer, G., Marte, C., Dietmaier, P., *et al.* (2016) 'Modelling surface rolling contact fatigue crack initiation taking severe plastic shear deformation into account', *Wear*. Elsevier, 352–353, pp. 136–145. doi: 10.1016/j.wear.2016.02.008.

Trummer, G., Marte, C., Scheriau, S., *et al.* (2016) 'Modelling wear and rolling contact fatigue: Parametric study and experimental results', *Wear*. Elsevier, 366–367, pp. 71–77. doi: 10.1016/j.wear.2016.04.024.

Ueda, M., Uchino, K. and Senuma, T. (2003) 'Effects of carbon content on wear property in pearlitic steels', *Materials Science Forum*, 426–432(2), pp. 1175–1180. doi: 10.1016/S0043-1648(02)00089-3.

Varfolomeev, I., Luke, M. and Burdack, M. (2011) 'Effect of specimen geometry on fatigue crack growth rates for the railway axle material EA4T', *Engineering Fracture Mechanics*. Elsevier Ltd, 78(5), pp. 742–753. doi: 10.1016/j.engfracmech.2010.11.011.

Vargolici, O. *et al.* (2016) 'Influence of the initial surface state of bodies in contact on the formation of white etching layers under dry sliding conditions', *Wear*. Elsevier, 366–367, pp. 209–216. doi: 10.1016/j.wear.2016.06.023.

Wang, W. J. *et al.* (2017) 'The role of slip ratio in rolling contact fatigue of rail materials under wet conditions', *Wear*, 376–377, pp. 1892–1900. doi: 10.1016/j.wear.2016.12.049.

Wetscher, F., Stock, R. and Pippan, R. (2007) ‘Changes in the mechanical properties of a pearlitic steel due to large shear deformation’, *Materials Science and Engineering A*, 445–446, pp. 237–243. doi: 10.1016/j.msea.2006.09.026.

Widiyarta, I. M., Franklin, F. J. and Kapoor, A. (2008) ‘Modelling thermal effects in ratcheting-led wear and rolling contact fatigue’, *Wear*, 265(9–10), pp. 1325–1331. doi: 10.1016/j.wear.2008.02.026.

Wilson, A. D. (1976) ‘Fatigue Crack Propagation in a533B Steels.’, *American Society of Mechanical Engineers (Paper)*, (76-WA/PVP-6).

Xiong, Y. *et al.* (2015) ‘Microstructure and Mechanical Properties of Granular Pearlite Steel After Equal Channel Angular Pressing’, *Journal of Materials Engineering and Performance*. Springer US, 24(7), pp. 2665–2669. doi: 10.1007/s11665-015-1553-7.

Zeng, D. *et al.* (2020) ‘Investigation of the crack initiation of subsurface rolling contact fatigue in railway wheels’, *International Journal of Fatigue*. Elsevier, 130(June 2019), p. 105281. doi: 10.1016/j.ijfatigue.2019.105281.

Zhilyaev, A. P. and Langdon, T. G. (2008) ‘Using high-pressure torsion for metal processing: Fundamentals and applications’, *Progress in Materials Science*, 53(6), pp. 893–979. doi: 10.1016/j.pmatsci.2008.03.002.